Investigating Advanced Cathode Materials for Li/Na-S Batteries

Experimentally and Theoretically

Chao Ye

A thesis submitted for the degree of Doctor of Philosophy

School of Chemical Engineering and Advanced Materials

The University of Adelaide

November 2019

Table of contents

Abstracts

Lithium/sodium-sulfur (Li/Na-S) batteries hold practical promise for next-generation batteries because of high energy density and low cost. Development is impeded at present however because of unsatisfied discharge capacity and stability in long cycling. Advanced materials can serve as sulfur host materials to improve the capacities and stability of the lithium/sodium-sulfur batteries. More importantly, they provide suitable models with which to connect and test experimental results with theoretical predictions. This is crucial to develop insight into the relationship between electrochemical behavior of sulfur and the structural properties of sulfur host materials. This thesis explores sulfur and its intermediates adsorption/redox conversion mechanisms and investigate crucial structural-property relationships of the advanced nanomaterials as sulfur host materials in high-performance lithium/sodium-sulfur batteries.

First, A unique three-dimensional hybrid of nickel sulfide and carbon hollow spheres was synthesized as a sulfur host. The uniformly distributed nickel sulfide can greatly promote adsorption capability towards polysulfides. Meanwhile, the hollow carbon spheres increase sulfur loading as well as the overall conductivity of the sulfur host. Utilized in an electrode, this 3D hybrid sulfur host achieved a capacity of 695 mA h g^{-1} after 300 cycles at 0.5 C and a low capacity decay of 0.013% per cycle.

Second, a two-dimensional (2D) MoN-VN heterostructure is investigated as a model sulfur host. The 2D heterostructure can regulate polysulfides and improve sulfur utilization efficiency. This resulted in superior rating and cycling performance. More importantly, incorporation of V in the heterostructure can effectively tailor the electronic structure of MoN. This leads to enhanced polysulfides adsorption.

Last, a two-dimensional (2D) metal-framework (MOF) is investigated as a model sulfur host for Na-S batteries. The MOF can enhance polysulfides adsorption and conversion kinetics. This resulted in superior rating and cycling performance. Through a combination of advanced experimental characterization techniques and theoretical computations based on the 2D nanomaterials, an in-depth understanding of sulfur redox and the structure-properties relationships in metal-sulfur batteries have been obtained.

Thesis Declaration

I certify that this work contains no material which has been accepted for the award of any other degree or diploma in my name in any university or other tertiary institution and, to the best of my knowledge and belief, contains no material previously published or written by another person, except where due reference has been made in the text. In addition, I certify that no part of this work will, in the future, be used in a submission in my name for any other degree or diploma in any university or other tertiary institution without the prior approval of the University of Adelaide and where applicable, any partner institution responsible for the joint award of this degree.

The author acknowledges that copyright of published works contained within this thesis resides with the copyright holder(s) of those works.

I give permission for the digital version of my thesis to be made available on the web, via the University's digital research repository, the Library Search and also through web search engines, unless permission has been granted by the University to restrict access for a period of time.

Chao Ye

Signature:

Date: 05/11/2019

Acknowledgments

This dissertation could only be completed thanks to the careful guidance and great devotion from my principle supervisor **Prof. Haihui Wang** and co-supervisor **Prof. Shi-Zhang Qiao**. During my four-year candidature, they devoted much of their time and patience to my selection of research topic, proposal of the concept, development of the experiment methodology, summary of the results and preparation of manuscripts. I would like to express my deepest gratitude to Prof. Wang for his lead and support throughout my Ph.D. study and for his patience, enthusiasm, and immense knowledge. He has inspired me to become an independent researcher and helped me realize the power of critical reasoning. In particular, I sincerely appreciated guidance and support in my study and daily living from Prof. Qiao. I am greatly inspired by his high-level research taste, accurate judgement and rigorous academic attitude. His solid fundamental knowledge, persistent pursuit of science and his day-to-day hard work will always motivate me to keep learning and working. He demonstrated what a brilliant and hard-working scientist can accomplish. Without his continuous guidance and valuable suggestions, this dissertation would hardly have been completed.

I would like to thank **Prof. Sheng Dai** (Brunel University London) for his academic guidance and support. I acknowledge the contribution of **Prof. Lei Zhang** (South China University of Technology) for his inspiring ideas and step-by-step teaching of experiment techniques. I would like to express my gratitude to **Prof. Tao Ling** (Tianjin University) for sharing her immense knowledge of experimental techniques without reservation. Her wise advice and encouragement are priceless for my work and life. Appreciation is also due to **Prof. Chunxian Guo** (Suzhou University of Science and Technology) for teaching me

valuable skills for writing and experiments design. I am indebted to **Dr. Yan Jiao** for leading me through theoretical calculations. I would not have a chance to look into such a wonderful microscopic world without her help and support. I am indebted to **Prof. Bo You** (Huazhong University of Science and Technology) and **Prof. Jingtao Wang** (Zhengzhou University) for their companionship and valuable comments on my work. In the last one year, I am lucky to have been guided by **Dr. Dongliang Chao**, who greatly helped me to gain widened and deepened knowledge about energy storage.

I am deeply indebted to all colleagues in Prof. Qiao's group viz. : **Dr. Yao Zheng**, **Dr. Sheng Chen**, **Dr. Jingjing Duan**, **Prof. Jingxue Sun**, **Dr. Jingrun Ran**, **Dr. Lin Xiong**, **Dr. Bita Bayasarmadi**, **Prof. Ping Chen**, **Mr. Tian Wen**, **Dr. Jinlong Liu**, **Dr. Lei Liu**, **Dr. Dongdong Zhu**, **Dr. Ke Zhang**, **Dr. Cheng Tang**, **Dr. Mohammad Ziaur Rahman**, **Dr. Fangxi Xie**, **Dr. Xuesi Wang**, **Dr. Yongqiang Zhao**, **Mr. Huanyu Jin**, **Mr. Anthony Vasileff**, **Mr. Yang Shi**, **Mr. Chaochen Xu**, **Ms. Jieqiong Shan**, **Mr. Xin Liu**, **Ms. Xing Zhi**, **Mr. Laiquan Li**, **Mr. Bingquan Xia**, **Mr. Xianlong Zhou**, **Mr. Huan Li**, **Mr. Dazhi Yao**, **Ms. Xin Xu**, **Mr. Yanzhao Zhang**. Thank **Dr. Xiaoguang Duan**, **Dr. Dongdong Li**, **Dr. Yanjie Wang**, **Dr. Heng Wang**, **Ms. Qi Bi**, **Mr. Fei Pei** (Xiamen University) and **Dr. Xiaofei Yang** (The University of Western Ontario) for the technological assistance and enlightening discussions. I would like to thank **Dr. Kenneth Davey** for his valuable comments and suggestions for the manuscripts of this work.

Special thanks go to the Analytical Services Coordinator **Dr. Qiuhong Hu** from School of Chemical Engineering and Advanced Materials for her kind technological support, care and encouragement. I would also express my gratitude to officers **Ms. Sue Earle**, **Ms. Michelle Fitton** and **Mr. Jason Peak** for their administrative help. I am indebted to **Dr. Lisa**

Chapter 1 Introduction

1.1. Background

Development of lithium-ion battery technology has dominated portable electronics devices over recent decades owing to their high voltage, low self-discharge rate, and stable cycling performance. Nevertheless, state-of-art lithium-ion batteries cannot meet the requirement of applications such as electric vehicles and grid-level energy storage, due to their low energy density (100-220 W h kg^{-1}) and high cost.[1-3]

Rechargeable metal-sulfur batteries are considered among the most promising candidates to achieve a low-cost and high-energy-density system owing to high theoretical specific capacities of elemental sulfur (1673 mA h g^{-1}) and metal, such as Li (3860 mA h g^{-1}), Na (1166 mA h g^{-1}), Mg (2205 mA h g^{-1}) and Al (2979 mA h g^{-1}). For example, lithium-sulfur (Li-S) batteries coupled sulfur and Li metal as cathode and anode exhibit an average voltage of 2.15 V. They can therefore deliver a theoretical energy density of ~ 2500 Wh kg^{-1}, which is significantly higher than that of the lithium-ion batteries. In addition, elemental sulfur is highly abundant, low-cost and low in toxicity. More importantly, redox conversion between the elemental sulfur and metal sulfide enable sulfur a universal cathode material to theoretically couple with a wide range of metal as anode. However, a series of intermediate metal polysulfides (MPoSs, M = Li, Na, K .etc, Li$_2$S$_n$, 2 < n ≤ 8) produced in the redox conversion are soluble in ethers-based solvent. The soluble MPoSs can diffuse to anode side and be chemically reduced by the metal, and then diffuse back to the cathode side. This "shuttle effect" results in loss of the sulfur and low Coulombic efficiency of the metal-sulfur batteries. In addition, low electrical conductivity of sulfur and metal sulfides as well as the pulverization of the cathode arising from large volume expansion during discharge largely

reduce utilization of the sulfur. Especially, high sulfur loading electrodes are essential for Li/Na–S technology in the marketplace. These problems become more severe with high sulfur loading in the sulfur cathode.

1.2. Aim and Objectives

The aim of this thesis is to design and synthesize effective and stable nanostructured cathode materials and illuminate the underlying structure-performance relations for Li/Na-S batteries. The specific objectives are as follows.

(1) To develop advanced cathode materials for high-performance Li/Na-S batteries through the investigation of surface atomic arrangement, surface areas and bulk compositions;

(2) To explore and understand the structure-performance relations and design principles of the cathode materials in Li/Na-S batteries;

(3) To fabricate high-performance Li/Na-S batteries with high capacities and stabilities.

1.3. Thesis Layout

This thesis contains six chapters. Chapter 1 introduces the significance and objectives of the thesis. Chapter 2 presents a critical review of the advanced materials in Li/Na-S batteries through experimental and theoretical approach. The mechanisms during the discharging and charging processes and their implications are discussed in detail. Additionally, it outlines the research objectives and key contributions. In Chapter 3, NiS@C-HS with high surface areas and high conductivity are first developed as an effective cathode material, which paves way for the development of highly efficient cathode material. In Chapter 4, 2D MoN-VN heterostructure was fabricated for the effective confinement of the polysulfides. Chapter 5 explores the effect of Ni-based MOF on the polysulfides adsorption and conversion kinetics Chapter 6 summarizes the key achievement of this thesis and provides perspectives for future

work.

References

(1) Clean Energy Council. Clean Energy Australia Report 2018 https://www.cleanenergycouncil.org.au/resources/resources-hub/clean-energy-australia-report.

(2) Hendriks, M. South Australia Leads the Way in Energy Storage Integration. *Energy News* **2018**, *36* (1), 15.

(3) Bruce, P. G.; Freunberger, S. A.; Hardwick, L. J.; Tarascon, J.-M. Li-O$_2$ and Li-S Batteries with High Energy Storage. *Nat. Mater.* **2012**, *11* (1), 19–29.

Chapter 2 Literature Review

2.1. Introduction

It is widely acknowledged that metal-sulfur batteries hold practical promise for next-generation batteries because of high energy density and low cost. However, a drawback with existing reviews is that they focus only on features and functions of electrode materials. What is missing is a critical evaluation of atomic/molecular-level structure-property relationships in sulfur cathodes and metal anodes. Significant progress has been made in understanding mechanisms for sulfur redox and metal stripping-plating to boost electrochemical performance of metal-sulfur batteries. This has rested on a judicious combination of experimental and theoretical approaches. Advanced nanomaterials (0D, 1D, 2D and 3D) have been widely studied in sulfur cathodes to boost the performances. For example, 3D hollow nanospheres can not only effectively confine the polysulfides within the hollow structures, also they can be utilized to build networks to enhance the electron/lithium ion conductivity. Two-dimensional (2D) nanomaterials offer a suitable model to correlate experimental results with theoretical predictions and, importantly, with which to explore structure-property relationships in metal-sulfur batteries. In this Review, we critically assess advances in 2D nanomaterials for metal-sulfur batteries and explore the atomic/molecular-level understanding of the structure-property relationships. In particular, we assess the prevailing sulfur redox and Li/Na stripping-plating reaction mechanisms from both an experimental and theoretical computational view and relationship between 2D nanomaterials design, physicochemical/electronic properties, reaction mechanisms and electrochemical performance.

2.2 Unveiling the Advances of 2D Materials for Li/Na-S Batteries Experimentally and Theoretically

This chapter is included as a submitted manuscript by Chao Ye, Dongliang Chao, Jieqiong Shan, Huan Li, Kenneth Davey, Shi-Zhang Qiao, Unveiling the Advances of 2D Materials for Li/Na-S Batteries Experimentally and Theoretically.

Statement of Authorship

Title of Paper	Unveiling the Advances of 2D Materials for Li/Na-S Batteries Experimentally and Theoretically
Publication Status	☐ Published ☐ Accepted for Publication ☑ Submitted for Publication ☐ Unpublished and Unsubmitted work written in manuscript style
Publication Details	Metal-sulfur batteries hold practical promise for next-generation batteries because of high energy density and low cost. Development is impeded at present however because of unsatisfied discharge capacity and stability in long cycling. Combination of experimental and theoretical approaches can be used to develop insight into the relationship between electrochemical behaviour of sulfur redox and metal stripping-plating and the structural properties of electrode materials. With metal-sulfur batteries, two-dimensional (2D) nanomaterials are a suitable model with which to connect and test experimental results with theoretical predictions and to explore structural-property relationships. Here through the view of combining experimental and theoretical approaches, we explore sulfur redox conversion on 2D nanomaterials in various reaction stages and critically review crucial factors impacting 2D nanomaterials as artificial solid electrolyte interfaces (SEIs) and host materials in protecting Li and Na metal anodes. We conclude with a focused discussion on promising research orientations for developing high-performance metal-sulfur batteries.

Principal Author

Name of Principal Author (Candidate)	Chao Ye
Contribution to the Paper	Chao Ye collected the data and wrote the manuscript.
Overall percentage (%)	70%
Certification:	This paper reports on original research I conducted during the period of my Higher Degree by Research candidature and is not subject to any obligations or contractual agreements with a third party that would constrain its inclusion in this thesis. I am the primary author of this paper.
Signature	Date 2019. 10. 31

Co-Author Contributions

By signing the Statement of Authorship, each author certifies that:

    i.   the candidate's stated contribution to the publication is accurate (as detailed above);

    ii.   permission is granted for the candidate in include the publication in the thesis; and

    iii.   the sum of all co-author contributions is equal to 100% less the candidate's stated contribution.

Name of Co-Author	Shi-Zhang Qiao
Contribution to the Paper	Prof. Shi-Zhang Qiao conceived the project, proposed the concept and prepared the manuscript.
Signature	Date 31/10/2019

Name of Co-Author	Dongliang Chao		
Contribution to the Paper	Dr. Dongliang Chao proposed the concept and prepared the manuscript.		
Signature		Date	31. Oct 2019

Name of Co-Author	Jieqiong Shan		
Contribution to the Paper	Jieqiong Shan prepared the manuscript.		
Signature		Date	2019.10.31

Name of Co-Author	Huan Li		
Contribution to the Paper	Huan Li prepared the manuscript.		
Signature		Date	2019./0.31

Name of Co-Author	Kenneth Davey		
Contribution to the Paper	Dr. Kenneth Davey prepared the manuscript.		
Signature		Date	31/10/2019

13

Unveiling the Advances of 2D Materials for Li/Na-S Batteries Experimentally and Theoretically

Chao Ye, [1, 2, 3] Dongliang Chao, [1, 2, 3] Jieqiong Shan, [1, 2] Huan Li, [1, 2] Kenneth Davey[1, 2] and Shi-Zhang Qiao[1, 2, *]

[1] School of Chemical Engineering & Advanced Materials, The University of Adelaide, Adelaide, SA 5005, Australia

[2] Centre for Materials in Energy and Catalysis (CMEC), The University of Adelaide, Adelaide, SA 5005, Australia

[3] These authors contributed equally

*Correspondence: s.qiao@adelaide.edu.au (S-Z. Q)

Abstract: Metal-sulfur batteries hold practical promise for next-generation batteries because of high energy density and low cost. Development is impeded at present however because of unsatisfied discharge capacity and stability in long cycling. Combination of experimental and theoretical approaches can be used to develop insight into the relationship between electrochemical behavior of sulfur redox and metal stripping-plating and the structural properties of electrode materials. With metal-sulfur batteries, two-dimensional (2D) nanomaterials are a suitable model with which to connect and test experimental results with theoretical predictions and to explore structural-property relationships. Here through the view of combining experimental and theoretical approaches, we explore sulfur redox conversion on 2D nanomaterials in various reaction stages and critically review crucial factors impacting 2D nanomaterials as artificial solid electrolyte interfaces (SEIs) and host materials in protecting Li and Na metal anodes. We conclude with a focused discussion on promising research orientations for developing high-performance metal-sulfur batteries.

14

Introduction

Rechargeable metal-sulfur batteries hold practical promise for next-generation batteries because of high energy density (> 300 W h kg^{-1}) and low cost of sulfur (~ \$150 ton^{-1}) when compared with state-of-the-art lithium-ion batteries with significantly lower energy density (100 – 220 W h kg^{-1}) and greater cost of active materials (e.g. $LiCoO_2$: ~ \$10000 ton^{-1}).[1] The high energy density is attributed to the high theoretical specific capacities of elemental sulfur (1673 mA h g^{-1}) and metals such as Li (3860 mA h g^{-1}) and Na (1166 mA h g^{-1}).[1-3] For example, lithium-sulfur (Li-S) batteries exhibit an average voltage of 2.15 V and can therefore deliver a theoretical energy density of ~ 2500 Wh kg^{-1}. This is significantly greater than for lithium-ion batteries.[4-8] Nevertheless, major obstacles for metal-sulfur batteries development are their unsatisfactory discharge capacities and stability.[9-11]

For high-performance metal-sulfur batteries, highly reversible and efficient interfacial reactions on sulfur cathodes/electrolyte and electrolyte/metal anodes interfaces are crucial (i.e. on the cathode side, elemental sulfur ↔ soluble metal polysulfides ↔ insoluble metal sulfides, and; on the anode side, metal stripping ↔ plating).[12-14] The reversibility and kinetics of these complex heterogeneous reactions significantly depend on physicochemical properties and electronic structure of the interfaces. Recent advances have resulted in an improved understanding of the electrochemistry of the interfacial reactions at the atomic/molecular level based on a judicious combining of experimental nanotechnology and computational quantum chemistry.[15,16] For example, remarkable advanced *in-situ* spectroscopy characterization techniques with high time-resolution have allowed identification of specific sulfur intermediates and the tracking of dynamic conversion processes. A result is that a comprehensive view of sulfur conversion kinetics in various

stages is obtained.[17,18] With theoretical investigations, researchers are capable now of obtaining growing fundamental insight into the adsorption/reaction origin on cathode/anode interfaces between sulfur species/solvation Li^+ and the electrode material. For example, it is practically possible to obtain a series of adsorption energies and decomposition energies of sulfur intermediates for a particular stage, based on thermochemical models and transition-states theory via density functional theory (DFT) computations. A comprehensive review of critical factors impacting reversibility and kinetics of the interfacial reactions on cathodes and anodes is therefore timely.

Two-dimensional (2D) nanomaterials, as sulfur/metal host materials, have been demonstrated as a particularly promising material to facilitate reversible and accelerated cathode/anode interfacial reactions.[19-21] So far, fine tuning of compositions and physicochemical/electronic properties of 2D nanomaterials can be achieved through defect engineering, heteroatom doping, heterostructure construction and hybridization.[22-31] One can synthesize 2D nanomaterials with a high density of active sites that facilitate rapid sulfur redox or homogeneous metal stripping-plating. More importantly, 2D nanomaterials with a uniformly exposed lattice plane provide ideal and programmable computational models to connect experimental results with theoretical studies. Additionally, free-standing flexible films of uniform thickness fabricated by 2D nanomaterials can significantly boost the energy storage efficiency of metal-sulfur batteries for practical application.[32]

Combining experimental and computational methodologies based on 2D nanomaterials has led to significant developments in lithium/sodium-sulfur (Li/Na-S) batteries over the years 2006 to 2019 as is seen in Figure 1. Importantly, this development has resulted in an increase in understanding of sulfur redox/metal stripping-plating at the atomic/molecular

level. Here, we review recent advances to boost electrochemical performance of Li/Na-S batteries from combining advanced experimental technologies and fundamental sciences. We show how a judicious combination of experimental and computational approaches can be used to understand crucial factors in Li/Na-S batteries and to direct a proof-of-concept design of 2D nanomaterials. We offer comprehensive insight into the structure-performance relationship of these nanomaterials in metal-sulfur batteries. We conclude with a focused discussion on promising research orientations for future development of high-performance metal-sulfur batteries.

Sulfur cathodes

Sulfur cathodes have been conjugated with a range of metal anodes to develop various metal-sulfur batteries. Amongst them, Li/Na-S batteries are the most widely studied in recent years owing to their outstanding high energy density and low cost (Figure 2).[33-36] Nevertheless, a major practical challenge is the polysulfide 'shuttle effect' on the sulfur cathode side.[37-39] This is a main cause of battery degradation as it leads to irreversible interfacial reaction on the sulfur cathodes. Soluble polysulfides generated in discharge can diffuse to the anode side and be reduced by metal anodes, and reduction products diffuse back to the cathode side.[40] More importantly, this results in loss of the active material of sulfur and consequently a low Coulombic efficiency (CE) with Li/Na-S batteries.[41] Additionally, the utilization of sulfur is largely reduced by its low electrical conductivity and resultant lithium/sodium sulfides, together with pulverization of the cathode resulted from a significant volume expansion during discharge. These problems are severe in cathodes with high sulfur loading and lean electrolyte.[42] The adsorption energies to polysulfides and kinetics of particular steps are widely considered as crucial factors impacting reversibility and kinetics of sulfur

electrochemical redox on sulfur cathodes. For example, in Li-S batteries, crucial steps such as reduction of soluble lithium polysulfides to insoluble Li_2S_2/Li_2S, Li_2S decomposition and Li_2S_2 reduction to Li_2S. These have been widely studied based on 2D nanomaterial models through combining experimental and theoretical approaches.

Metal-free 2D nanomaterials

Amongst the more widely studied metal-free materials in sulfur cathodes, graphene and hybrids possess several unique properties. These include : 1) large theoretical surface area, 2) large modulus of elasticity, and 3) attractive thermal/electrical conductivities. These properties make graphene an ideal sulfur host material.[43] Early research on graphene oxide (GO) in sulfur cathodes focused mainly on modification of the pore structure to provide physical confinement of the polysulfides. Dai and co-workers first developed a graphene/S composite electrode (S-PEG/G) with surfactant-directed sulfur particles and graphene nanosheets. This resulted in sulfur particles with improved electrical conductivity and provided enhanced physical confinement of the polysulfides within the graphene. The resultant sulfur cathodes showed specific capacity of nearly 800 mA h g^{-1} with life-span of 100 cylces.[44] Zhang and co-workers demonstrated that graphene oxide and sulfur composite cathode (GO-S) exhibit strong sulfur chemical adsorption and, therefore a prolonged span life of Li-S batteries. Soft X-ray absorption spectroscopy (XAS) measurements highlighted strong chemical interaction between S and these groups together with surface C atoms in GO.[45] One of the limitations of GO in sulfur cathodes however is that its electrical conductivity depends on its oxidation degree.[46] To address this, significant research has focused on synthesis of GO with various functional groups and tailored porosity, or hybridization of graphene with other conductive nanomaterials.[47-51] Despite this,

accomplishing enhanced polysulfides adsorption capability is a significant challenge on pristine GO.

To improve polysulfide adsorption on GO, heteroatom dopants can be introduced to boost interaction between GO and polysulfides. Zhang and co-workers highlighted that sulfur cathodes with N-doped graphene (NG) were effective for boosting polysulfides adsorption. *Ab initio* molecular dynamics (AIMD) computations implied that the polysulfides adsorption energies of the NG are greater than those for pristine graphene. Importantly, dominant pyridinic N and pyrrolic N in NG can form S_xLi-N interactions with lithium polysulfides via N lone-pair electrons.[52] Li and co-workers reported a fundamental study on polysulfides adsorption origin on NG. Through systematic DFT computations on behavior of lithium polysulfides adsorption on NG with various N dopants, they showed that only NG with pyridinic N-dopants interacts with the polysulfides.[53] Recently, Hou et al. employed systematic DFT computations to investigate the chemical origin of the polysulfides adsorption behavior on heteroatoms-doped nanocarbon materials to establish design principles. These authors proposed that the formation of a 'Li-bond' significantly enhances polysulfide adsorption and thereby effectively prevents the shuttle of polysulfides.[54] Further, Zhang and co-workers identified this Li-bond in sulfur cathodes via a combination of theoretical calculations and ^{7}Li nuclear magnetic resonance (NMR) measurements based on NG. They for the first time proposed a quantitative descriptor of chemical shift in ^{7}Li NMR to describe the Li-bond strength. The variations of chemical shift in NMR spectrum were in good agreement with DFT results. Therefore, the theoretically predicted Li-bond strength was verified through experimental ^{7}Li NMR results (Figures 3A and 3B).[55] Later, Zhou et al. reported that a N/S co-doped graphene (N,S-G) sponge electrode

provided strong polysulfides adsorption owing to a synergistic effect of nitrogen and sulfur dopants. A combination of lithium polysulfides physical confinement in the porous graphene and the polysulfides chemical adsorption to N and S sites in graphene, significantly prevented S loss. This resulted in a specific capacity of 1200 mA h g^{-1} at 0.2 C and good life-span of 500 cycles with nearly 100 % CE (Figure 3C).[56]

Recently, metal-free 2D nanomaterials have been utilized as a substrate to support low concentration metal single atoms that exhibit boosted performance in sulfur cathodes. For example, Ni@NG was reported to have a lower barrier for Li$_2$S decomposition than that for NG. The Ni-N-C moieties therefore facilitated formation and decomposition of Li$_2$S in discharge/charge process. Moreover, the low decomposition energy of Li$_2$S on Ni@NG contributes to enhanced conversion kinetics of polysulfides through $S_x^{2-}\cdots$Ni-N bonding. These properties resulted in significantly boosted rate performance and cycling stability in the Li-S batteries (Figures 3D, 3E and 3F).[57] Another example can be found with Co single atom decorated NG at a high S mass loading(6.0 mg cm^{-2}), in which Co@NG sulfur cathodes delivered a significant aerial capacity of 5.1 mA h cm^{-2} at 0.2 C together with a low capacity decay of 0.029 % per cycle.[58]

Other metal-free 2D nanomaterials have been widely studied in sulfur cathodes. For example, graphitic carbon nitride (g-C$_3$N$_4$) is a 2D crystal with a layered structure with van der Waals interaction between the layers. Importantly, plentiful pyridinic nitrogen species in g-C$_3$N$_4$ is considered crucial to improved polysulfides chemical adsorption. A seminal report was the synthesis of oxygenated carbon nitride (OCN) for Li-S batteries: enriched nitrogen and micro/mesopores in the material resulted in high S utilization and stable long-term cycle-life.[59] Quan et al. demonstrated electron transfer from electron-rich pyridinic N$^{\delta-}$ groups to

Li$^+$ in the polysulfides using Li 1s X-ray photoelectron spectroscopy (XPS) (Figure 3G). DFT computations implied that the Li$_2$S$_2$ is adsorbed via Li-N bonding illustrated by a shortened bond length of 2.06 Å, in comparison with the average length of 2.14 Å. They pointed out that 53.5 atom % N concentration is sufficient to absorb all polysulfides of a sulfur cathode containing 75 wt % sulfur, and resultant sulfur cathodes of 0.04 % capacity fade per cycle under 0.5 C in 1500 cycles (Figures 3H and 3I).[60] Additionally, g-C$_3$N$_4$ hybrids such as hybrid of graphene and g-C$_3$N$_4$ was also investigated as host materials to promote electrochemical properties of sulfur cathodes.[61,62]

For other analogues to graphene, including graphdiyne and hexagonal boron nitride (h-BN), there is little reported research for electrochemical applications. This might be due to its low stability together with poor electrical conductivity.[63] Black phosphorus (BP) is semiconductor with a layered structure and a bandgap of ∼ 2 eV that can be tuned through controlling thickness. Cui and co-workers reported a BP coated commercial separator in which the BP, with descent electron conductivity and ultra-high Li diffusion, trapped and activated polysulfides. The *ex-situ* XPS results indicated that BP adsorbed polysulfides through both P-S and P-Li bonds. Significantly, DFT computations confirmed these experimental results.[64]

Metal oxides

Inorganic materials represent an attractive class of host materials for sulfur cathodes. This is because they possess potential stronger adsorption energies to the polysulfides and more complex adsorption mechanisms to the polysulfides.[65-67] This presents an opportunity to boost adsorption and conversion kinetics of the polysulfides via a new mechanism. Early studies on the use of metal oxides as additives in sulfur cathodes were generally with

nonconductive oxides that included $Mg_{0.6}Ni_{0.4}O$ and SiO_2.[68,69] For example, Nazar and co-workers reported that semi-conducting Ti_4O_7 possessed strong polysulfides adsorption. A combination of *operando* XAS and electrochemical tests revealed that Ti_4O_7 enabled a significantly more rapid Li_2S deposition during discharge. This was attributed to an enhanced redox electron transfer on the Ti_4O_7 that resulted in significantly reduced interfacial impedance. They concluded that adjusting sulfiphilic and metallic properties of inorganic additives was crucial to facilitate sulfur redox reaction.[70] Further, these authors proposed a distinctive mechanism based on MnO_2 nanosheets as a redox mediator in the sulfur cathode (Figure 4A). Based on *ex-situ* XPS results, thiosulfate surface species formed on the MnO_2 surface that reacted with the polysulfides to produce a polythionate complex and shorter polysulfides. MnO_2 therefore can act as a redox mediator to bind soluble polysulfides and facilitate conversion to Li_2S via disproportionation. The resultant Li-S batteries exhibited a limited capacity decay of approximately 0.036 % per cycle over 2000 cycles (Figures 4B and 4C).[71] Cui and co-workers investigated systematically Li^+ diffusion properties on a series of nonconductive metal oxides decorated carbon flakes (Figure 4D). Significantly, a combination of electrochemical tests and DFT computations revealed fast polysulfides diffusion, that induced controlled growth of Li_2S and was essential for sulfur redox conversion. As a result, composite materials of MgO/C, La_2O_3/C and CeO_2/C nanoflakes showed greater capacity and better cycling performance in comparison with other studied metal oxides (Figures 4E and 4F).[72]

More recently extensive research attention has been given to the impact of geometric properties of metal oxides surface on polysulfides conversion. For example, oxygen vacancies have been considered to be beneficial in promoting polysulfides conversion

kinetics in sulfur cathodes.[73] However, it was demonstrated that on ultra-thin niobic acid, adsorption and conversion of polysulfides is hindered by the oxygen vacancies (Figure 4G). Results from a judicious combination of electrochemical tests and DFT computations attributed inferior performance of niobic acid to decreased electrical conductivity and weakened polysulfides adsorption, which is induced by oxygen vacancies (Figures 4H and 4I).[74]

Metal sulfides

With development of syntheses for 2D metal dichalcogenides, metal sulfides have been explored for sulfur cathodes in recent times.[75-77] Metal sulfides have a number of major benefits that include: 1) low lithiation voltages *vs*. Li/Li$^+$ that is less likely to overlap with working voltage windows of sulfur cathodes, and 2) a largely metallic or half-metallic property that contrasts with that for metal oxides. For example, Pentlandite Co_9S_8 exhibits a significantly good room-temperature conductivity of 290 S cm^{-1}. With dual-interaction based on S (from polysulfides)-Co and Li-S (from Co_9S_8) between the polysulfides and Co_9S_8, a low capacity fading of 0.045 % per cycle in 1500 cycles can be achieved.[78] Cui and co-workers demonstrated a 2D titanium sulfide (TiS_2) as an effective host material for Li_2S. TiS_2 possesses high conductivity and polar Ti atoms that can potentially form Ti-S bonds. These result in strong interactions with Li_2S/Li_2S_n species.[79]

Transition metal dichalcogenides (TMDs), a large group of 2D nanomaterials, have attracted significant research attention for sulfur cathodes, especially MoS_2, owing to unique physicochemical/electronic properties and large surface area. A major development was understanding polysulfide adsorption on different sites of the 2D nanomaterials for controlled Li_2S deposition via a combination of theoretical and experimental investigations

(Figure 5A). The selectivity of Li$_2$S deposition on MoS$_2$ edge sites, compared with that of the MoS$_2$ terrace sites, was demonstrated through DFT computations, electrochemical tests and microscopic characterizations (Figures 5B and 5C). The vertically aligned MoS$_2$ (V-MoS$_2$) significantly promoted electrochemical performance compared with that of the horizontal MoS$_2$ (H- MoS$_2$). This work proffered guidance for design of 2D MoS$_2$ with improved metal-sulfur batteries.[80] Lee and co-workers studied the effect of S deficiencies on MoS$_2$ basal plane on sulfur redox conversion. They found that S deficiencies boosted conversion of soluble lithium polysulfides. This decreased losses from the shuttle effect. As a result, a meaningfully small amount of MoS$_{2-x}$/rGO (i.e. 4 wt% in the cathode) promoted simultaneously rating capacity and cycling stability. These findings provided strong evidence for the catalytic impact of MoS$_{2-x}$/rGO in the sulfur cathode (Figures 5D, 5E and 5F).[81] Most recently, MoS$_3$ was studied as cathode materials in Li/Na-S batteries to enable relative high capacity and long life-span (Figure 5G). A combination of *operando* XAS experiments and DFT computations provided convincing evidence that repetitive discharge/charge processes did not lead to decomposition of MoS$_3$ (Figures 5H and 5I). Significantly, shuttle effect can be avoided because there was no Li$_2$S or polysulfide detected during the discharge/charge processes.[82]

A range of metal sulfides can be used in investigation of polysulfides adsorption behavior and conversion and offer insight into the energy barriers in these processes. Zhou et al. selected a series of metal sulfides as models to explore crucial parameters in determining the energy barrier for Li$_2$S decomposition (Figure 6A). They demonstrated that the Li$_2$S decomposition energy barrier was associated with the binding between Li$^+$ and the S atoms in metal sulfides. The resultant sulfur cathodes with VS$_2$, TiS$_2$ and CoS$_2$ exhibited

greater capacity, lower overpotential and better cycling stability when compared with the other metal sulfides-based electrodes (Figures 6B and 6C).[83] Similarly, Chen et al. selected a series of transitional-metal sulfides as modes to obtain an in-depth understanding of adsorption origin to the polysulfides (Figure 6D). It was concluded that strong S bonds are induced mainly by electron transfer between metal atoms in metal sulfides and S atoms in lithium polysulfides, whilst Li bonds are induced by electrostatic interactions between them. The adsorption energies and Li diffusion energy barriers are crucial factors for high-performance sulfur cathodes. VS_2 has the strongest adsorption ability on the polysulfides together with a low diffusion barrier among all the transitional-metal sulfides (Figures 6E and 6F).[84]

Research has focused on soluble polysulfides conversion and Li_2S deposition/oxidation. However, the importance of conversion from Li_2S_2 to Li_2S has been overlooked. Recently, Yang et al. reported a 2D nanomaterial of CoS_3@NG (CoS_3-S) as an effective electrocatalyst for electrochemical conversion from Li_2S_2 to Li_2S (Figure 6G). Significantly, a combination of *in-situ* XAS characterizations and DFT computations revealed that CoS_3 had strong interaction with sulfur species, and significantly low Li_2S_2 dissociation energy, facilitating conversion of Li_2S_2 to Li_2S (Figures 6H and 6I). The sulfur cathode with high sulfur loaded electrodes (3 - 10 mg cm^{-2}) with CoS_3 exhibited > 80 % sulfur utilization. This is a > 20 % increase compared with counterparts without CoS_3.[85]

Other inorganics

In addition to 2D metal oxides and sulfides, inorganics such as 2D metal carbides/nitrides, phosphides and metal organic frameworks (MOFs) with porous structure and strong chemical interaction with polysulfides have been used as metal-sulfur batteries.[86-91] Amongst

these materials MXene appears as a practical option. Derived from a selective etching out the A constituent to exfoliate MAX phases, where M, A, X refer to early transition metal, group 13 or 14 element, C and/or N, respectively, MXene exhibits high conductivity, large specific surface area and strong interaction with polysulfides.[92,93] Nazar and co-workers explored the surface chemistry of the polysulfides on titanium based MXene phases (Figure 7A). Using a combination of XPS analyses and DFT computations, these authors demonstrated for the first time, that prior to a Lewis acid-base interaction of Ti-S bond, hydroxyl groups on the MXene surface facilitate conversion from the polysulfides to thiosulfate (Figures 7B and 7C). This finding of dual-mode behavior provided a new mechanism to confine polysulfides and to enable promoted cycling performance of the Li-S batteries.[94] Qiao and co-workers fabricated a 2D heterostructured MoN-VN as a new model sulfur host (Figures 7D and 7E). Spectroscopic studies highlighted that Mo in MoN-VN heterostructures possess greater chemical interaction with the polysulfides than does Mo in MoN. Theoretical investigations underscored that the electronic structure modification of 2D MoN achieved by incorporation of V resulted in enhanced adsorption capability to the polysulfides on the 2D MoN-VN. Compared with the 2D MoN, the 2D MoN-VN heterostructure showed improved sulfur utilization efficiency and capacity retention.[95] Li and co-workers, similarly through a judicious combination of experimental and theoretical approaches, demonstrated VN with strong polysulfides chemical adsorption. These authors synthesized a 3D free-standing electrode with porous VN and graphene to achieve a significant rate performance of 956 mA h g^{-1} at 2 C (Figure 7F).[96]

To study the effect of anions on polysulfides adsorption/conversion of various inorganics, Qian and co-workers systematically studied the kinetic behavior of Li-S

chemistry on Co-based inorganics and deciphered the descriptor of the electrochemical results. DFT computations revealed that a shift of p band centers highly significantly impacted kinetics of interfacial electron transfer on Co-based inorganics (Figure 7G). Moreover, a scaling relationship was established between the energy gap of d and p band centers and the redox potentials. This revealed that the anion p band position and electronic structural engineering is crucial for sulfur redox conversion (Figures 7H and 7I).[97] As a result, CoP exhibits the lowest overpotential for polysulfide redox conversion, and CoP-based sulfur cathodes deliver a capacity of 417 mA h g^{-1} at 40 C together with an unmatched power density of 137 kW kg^{-1}.[98]

In order to boost both electron conduction and polysulfide adsorption properties, Nazar and co-workers reported lightweight MgB_2 as a sulfur host. They showed that borides are unique in that both B- and Mg- terminated surfaces bond with S_x^{2-} anions through DFT computations. The surface-mediated polysulfide redox behavior resulted in a significantly greater exchange current in comparison with MgO. By fabricating a high-surface-area composite structure via hybridizing MgB_2 with graphene, these researchers synthesized sulfur cathodes with stable cycling properties at a high sulfur loading of 9.3 mg cm^{-2}.[99]

Metal anodes

The acknowledged instability of the Li/Na stripping-plating interfacial reaction is considered originating from the high reactivity with polysulfides/additives in organic electrolyte and significant volume change during the stripping-plating process.[100] These act together to form unstable SEI and uncontrollable growth of Li/Na dendrites that can lead to problems such as: 1) low CE, 2) Li/Na powdering, and 3) internal short-circuits in Li/Na metal batteries. A significantly reduced life-span and important overriding safety concerns with Li/Na metal

anodes can act to limit practical application of Li/Na-S batteries.[2] The judicious combining

of experimental studies and theoretical computational investigations can be used to reveal

the chemical origin of reaction between the metal and solvents or additives in the electrolyte.

This approach can be successfully used to predict stability of the SEI and thereby assist the

search for and screening of appropriate compositions in the electrolyte. Additionally, 2D

nanomaterials such as graphene and h-BN have been used to fabricate artificial SEIs.

Advantages include: 1) a light weight, large specific surface area, 2) high chemical stability,

and 3) good mechanical strength. The SEI formed during the anode reaction can be stabilized

on top of the artificial SEIs and the metal ions can be plated underneath the artificial SEIs.[101]

Both these strategies improve CE. 2D nanomaterials as Li/Na hosts with high porosity and

lithiophilic/sodiophilic properties, have been demonstrated to enable homogeneous Li/Na

nucleation and to block dendrite growth.[102]

2D nanomaterials in Li metal anodes

The structure and components of SEIs formed on Li anodes in Li-S batteries are distinctive

from those in routine Li metal batteries because of the reactivity of lithium polysulfides with

Li metal. This results in additional requirements of high resistance to lithium polysulfides

and high Li loading to match sulfur cathodes for Li metal anodes in Li-S batteries.[103] In

addition to strategies such as introduction of electrolyte additives and optimization of

electrolyte components, artificial SEIs have been widely studied via combining experimental

and theoretical approaches to protect Li metal anode. For example, an artificial SEI

fabricated via electroplating in electrolyte (based on LiTFSI, LiNO$_3$ and Li$_2$S$_5$) was used to

prevent side reactions (Figure 8A). Theoretical calculations showed that the highest

occupied molecular orbitals (HOMOs) of SEI components were lower than the lowest

unoccupied molecular orbitals (LUMOs) of the solvents, including 1,3-dioxolane/1,2-dimethoxyethane (DOL/DME) and ethylene carbonate/diethyl carbonate (EC/DEC) solvents (Figure 8B). This indicates the artificial SEI is stable against DOL/DME and EC/DEC solvents. The resultant Li-S pouch cells showed significantly boosted capacity from 156 to 917 mA h g^{-1} and enhanced CE from 12 % to 85 % at 0.1 C compared with Li-S pouch cells without protection of the artificial SEI.[104] In addition, fabrication of artificial SEI and lithiophilic matrix with 2D nanomaterials has also been extensively studied.[105-109] For example, Reza and co-workers demonstrated a facile application of defective GO on Li anodes. DFT computations and AIMD simulations indicated that lithiophilic GO enhances Li$^+$ adsorption and diffusion to the Li anode surface through defect sites on the GO (Figure 8C). Phase-field modeling (PFM) showed that defective GO with good mechanical property can physically block the Li dendrites growth (Figure 8D). A dense and uniform plating of Li and significant improvement in cyclability and stability was achieved. Overall findings suggest that the lithiophilic and defective nature of the GO coating have a synergic effect for protecting Li anode as artificial SEIs.[110] Kim used phosphate functional graphenes to design artificial SEIs that improve Li anode stability. This artificial SEI stabilized Li migration through a favored interaction of the Li with pyro-/metaphosphates and phosphorus species.[111]

The concept of lithiophilicity has been a dominant indicator in estimating the Li host properties since Cui and co-workers pioneered in fabricating layered Li-GO composite films through thermal infusion.[112] Recently NG has been reported as the Li plating matrix in Li anodes that assists to regulate the nucleation of Li metal and therefore suppresses the growth of Li dendrites. Amongst the different configurations in NG, the lithiophilic pyridinic and

pyrrolic nitrogen were demonstrated to facilitate uniform nucleation and distribution of Li on the anode surface. With this modification a dendrite-free morphology is achieved on the Li metal anode, and consequently a high CE of 98 % in 200 cycles.[113] Zhang and co-workers proposed a descriptor of log (0.5 × electronegativity + local dipole) for Li binding energy on doped graphene via combining NMR spectra and DFT computations. They showed that a dopant with a large electronegative and a strong local dipole directly delivered a large binding energy (Figures 8E and 8F). Li nucleation overpotential tests confirmed the O doping carbon frameworks possessed excellent lithiophilicity. This was also evidenced by TEM images.[114]

In addition to graphene, other 2D nanomaterials with homogeneous Li nucleation sites have been explored to protect the Li metal anode. For example, Yang and co-workers have reported uniform nucleation of Li a g-C_3N_4 coating on 3D collector. They emphasized that the inherent negative electric fields on the g-C_3N_4 possess a strong ability to adsorb Li^+ as was confirmed through DFT computation. The uniform electric field induced by the high N content results in homogeneous Li nucleation sites, promoting homogeneous Li nucleation. The resultant Li anode had a high CE of 98 % and an ultra-long life-span with a high capacity of 9 mA h cm^{-2}.[115]

2D nanomaterials in Na metal anodes

Because of different intrinsic atomic and physicochemical properties of metal Na from metal Li, Na dendritic nucleation/growth mechanism and SEI components/structure on Na metal anode in RT Na-S batteries are not analogues to those for Li-S batteries and have been poorly elucidated.[116] Importantly, because of the high reactivity of Na with solvent/additives in the electrolyte, the formation of a stable SEI could actually play a more important role in

protecting Na metal anodes than that in Li metal anodes.[117,118] This would also mean that computations, such as adsorption energy and diffusion barriers in Li metal anode, are oversimplified for Na plating. It is significant to note that the protection of Na metal anodes is discussed rarely in the general field of RT Na-S battery research. Therefore, here we have focused on more generally on Na metal anodes.

Despite that strategies applied in Li anodes are not aligned to Na anodes, several researchers have demonstrated that alloying is effective in avoiding Na dendrites due to a low melting point of Na.[119,120] In addition, the thermal infusion approach was used successfully in fabricating controllable Na-GO composite anodes. Compared with the pristine Na metal, the mechanical strength and electrochemical stability of Na-GO anodes were boosted.[121]

In the search for 2D nanomaterials as artificial SEIs, Zhang and co-workers concluded that to make a compromise between metal ion diffusion and acceptable mechanical property is important. In general, the diffusion barrier strongly depends on the size of the hollow atomic ring in 2D nanomaterials. In addition, electronic structure can significantly impact barriers for ion diffusion. For example, although structures and atomic bond lengths of defective h-BN and graphene are similar, the former one enables significantly better ion diffusion compared with the latter one (~ 24 orders of magnitude greater). Additionally, improving ion diffusion through introducing defects or pores decreases mechanical property of the 2D materials to suppress Li/Na dendrite growth (Figures 8G and 8H).[122]

Notably, in following research it was shown that defective graphene catalyzes SEI formation on the Na anode. The authors compared the defective graphene with nanopores and pristine graphene. They found that the former led to a thicker SEI than the later. This

resulted in a significant overpotential and low CE during subsequent Na plating/stripping. This promoted growth of metal dendrites and electrical shorting.[123] More recently, a facile and versatile strategy was demonstrated by synthesizing a sodiophilic interphase. Through DFT computations this facilitated a homogenous Na nucleation and lateral Na plating to form dendrite-free Na metal anode (Figure 8I). The resultant Na anode exhibited an ultra-high specific capacity that approached the theoretical capacity and ultra-long life up to 3000 cycles[124]

Summary and outlook

Crucial factors such as adsorption energy, diffusion barrier and electronic structure have been widely investigated from a theoretical view using DFT computations to assess performance of various materials, especially sulfur cathodes (Figure 9). In addition, other computational methods such as AIMD have been used to reveal microscopic sulfur redox kinetics.[125-127] At the same time, a broad spectrum of spectroscopic characterization, electron microscopy techniques and electrochemical methods have been used on a range of 2D nanomaterials to investigate relationships between surface physicochemical properties and dynamic conversion of intermediates species on cathodes and anodes.

Author contributions

S.-Z. Q. proposed the topic. C. Y., D. C., J. S., H. L., K. D. and S.-Z. Q. wrote and revised the manuscript.

Declaration of interests

The authors declare no competing interests.
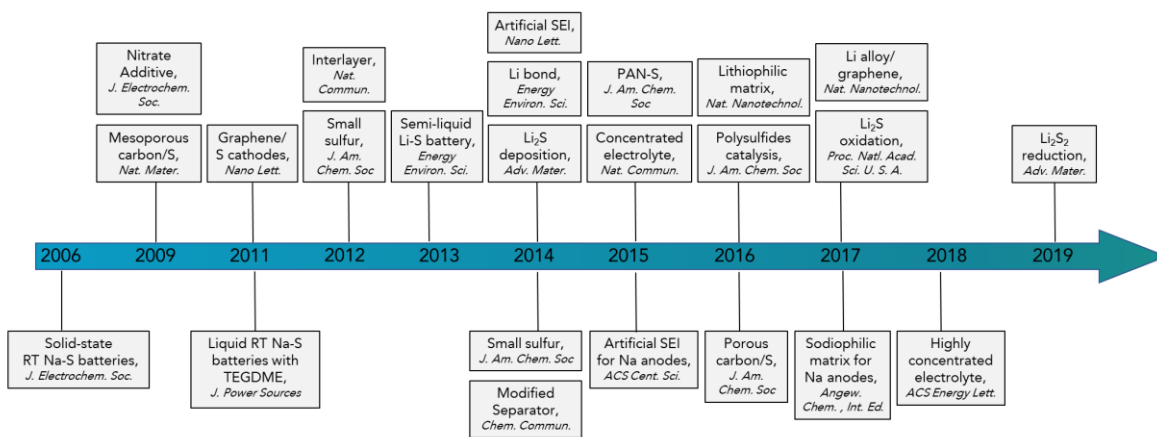
Li-S batteries

Figure 1. Timeline (2006 to 2019) for Li-S and Na-S battery development.
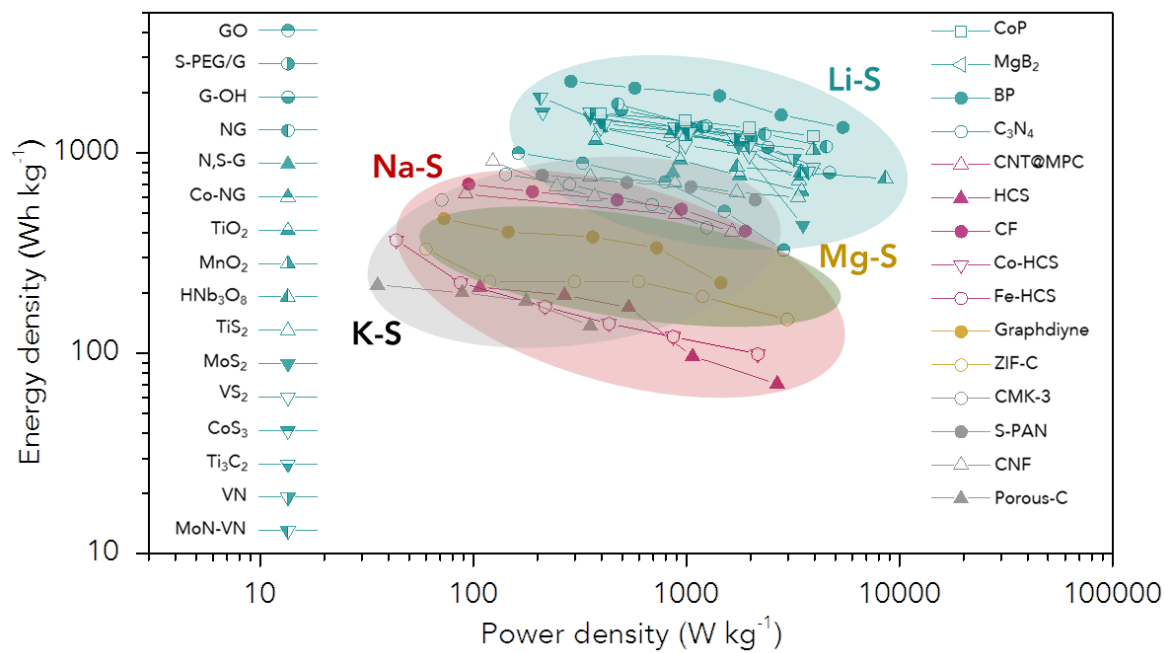
Figure 2. Summary comparison of power and energy density of metal-sulfur batteries with regard to mass of sulfur cathode.
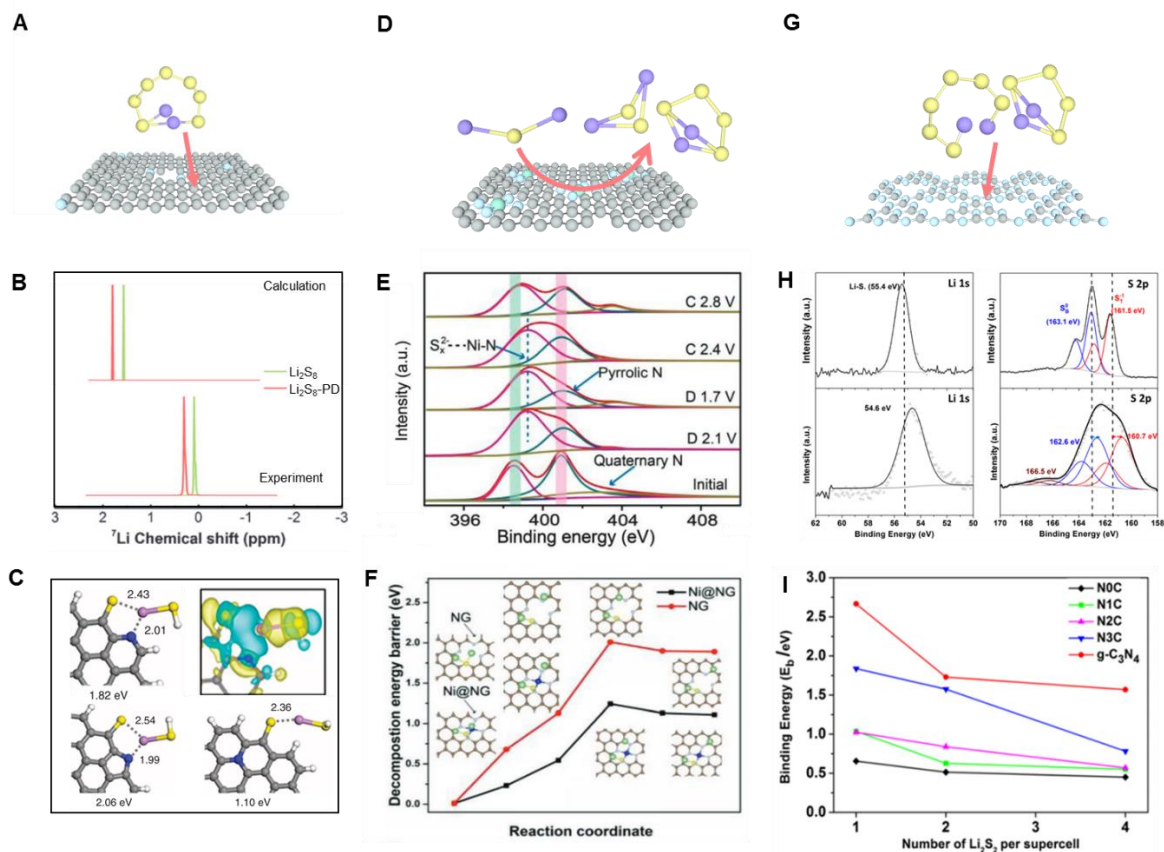
Figure 3. 2D carbonaceous nanomaterials as sulfur hosts in sulfur cathodes. (A) Schematic diagram of polysulfides adsorption on N-doped graphene (Grey, light blue, yellow and purple balls represent C, N, S and Li atoms, respectively). (B) Theoretically computed and experimentally obtained ^{7}Li NMR spectra for Li_2S_8 before and after interacting with pyridine. Reproduced with permission from Hou et al.[55] Copyright 2017 John Wiley Sons, Inc. (C) Optimized configurations for binding of the polysulfides to N,S-G. Reproduced with permission from Zhou et al.[56] Copyright 2015 Nature Publishing Group. (D) Schematic of Li_2S oxidation on Ni single atom on N-doped graphene (Grey, light blue, green, yellow and purple balls represent C, N, Ni, S and Li atoms, respectively). (E) XPS spectra of N 1s on the Ni@NG at various charge/discharge states. (F) The decomposition energy barriers of Li_2S on the Ni@NG and NG (Blue, cyan, green, yellow, and brown balls represent Ni, N, Li, S, and C atoms, respectively). Reproduced with permission from Zhang et al.[57] Copyright 2019 John Wiley Sons, Inc. (G) Schematic of polysulfides adsorption on g-C_3N_4 (Grey, light blue, yellow and purple balls represent C, N, S and Li atoms, respectively). (H) Li 1s and S 2p XPS spectra of Li_2S_4 and g-C_3N_4/Li_2S_4 mixture. (I) Variation of binding energy of Li_2S_2 molecules versus the number of Li_2S_2 on respective substrates. Reproduced with permission from Pang et al.[60] Copyright 2016 American Chemical Society.
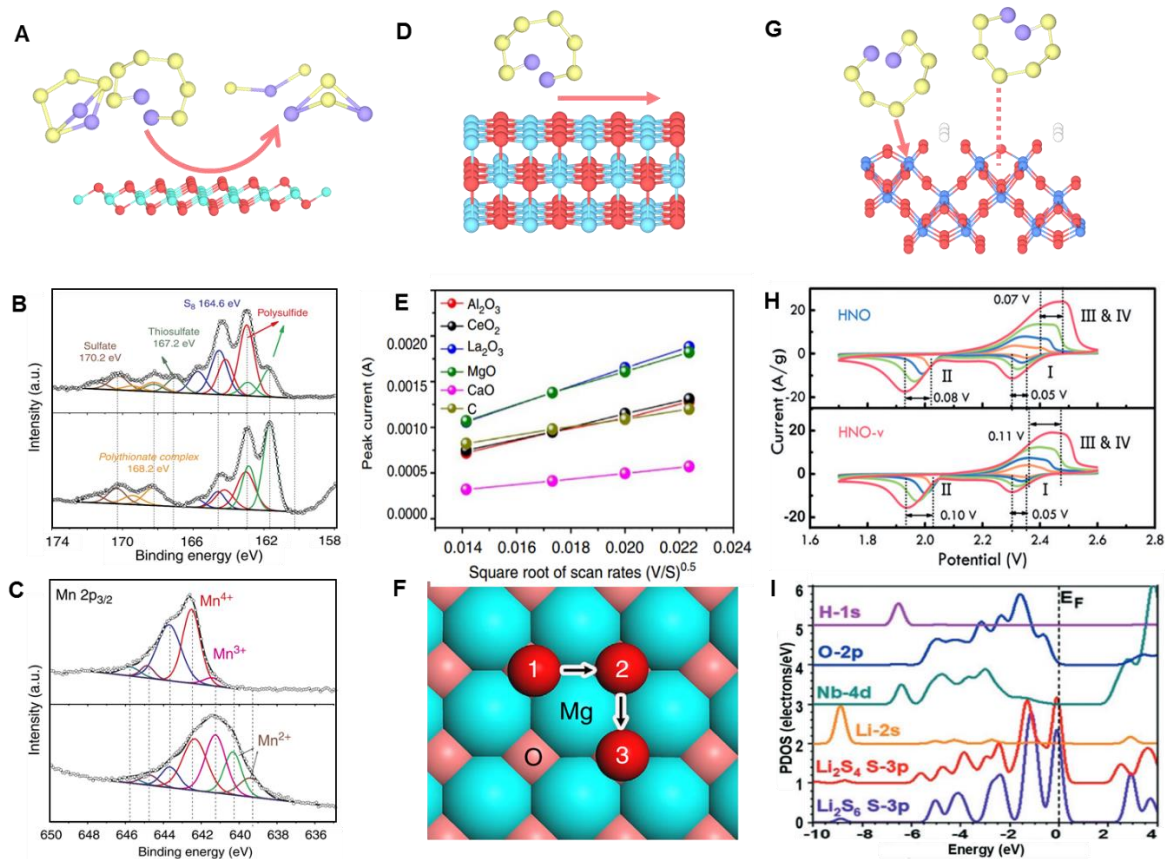
Figure 4. Metal oxide nanomaterials promoting sulfur redox in sulfur cathodes. (A) Schematic diagram of reduction of polysulfides on MnO_2 nanosheets (Red, cyan, yellow and purple balls represent O, Mn, S and Li atoms, respectively). (B) *Ex-situ* XPS of S/MnO_2 electrodes after discharge to 2.15 V (top) and aged for 20 h afterwards (bottom). (C) Mn $2p_{3/2}$ spectra of MnO_2 nanosheet (top) and MnO_2-Li_2S_4 (bottom). Reproduced with permission from Liang et al.[71] Copyright 2015 Nature Publishing Group. (D) Schematic of polysulfides diffusion on MgO (Red, sky blue, yellow and purple balls represent O, Mg, S and Li atoms, respectively). (E) Plot of CV peak current of the cathodic reaction S_8-Li_2S_4. (F) Minimum energy path for Li ion diffusion on MgO (100). Reproduced with permission from Tao et al.[72] Copyright 2015 Nature Publishing Group. (G) Schematic of polysulfides adsorption on HNb_3O_8 nanobelts (Red, white, blue, yellow and purple balls represent O, H, Nb, S and Li atoms, respectively). (H) CV curves of HNb_3O_8 (HNO) and HNb_3O_8 with high oxygen vacancy concentration (HNO-v) cathodes. Orange, blue, green and red lines represent scan rates of 0.2, 0.5, 1.0 and 2.0 mV s^{-1}, respectively. (I) The PDOSs of HNb_3O_8. Reproduced with permission from Xu et al.[74] Copyright 2019 John Wiley Sons, Inc.
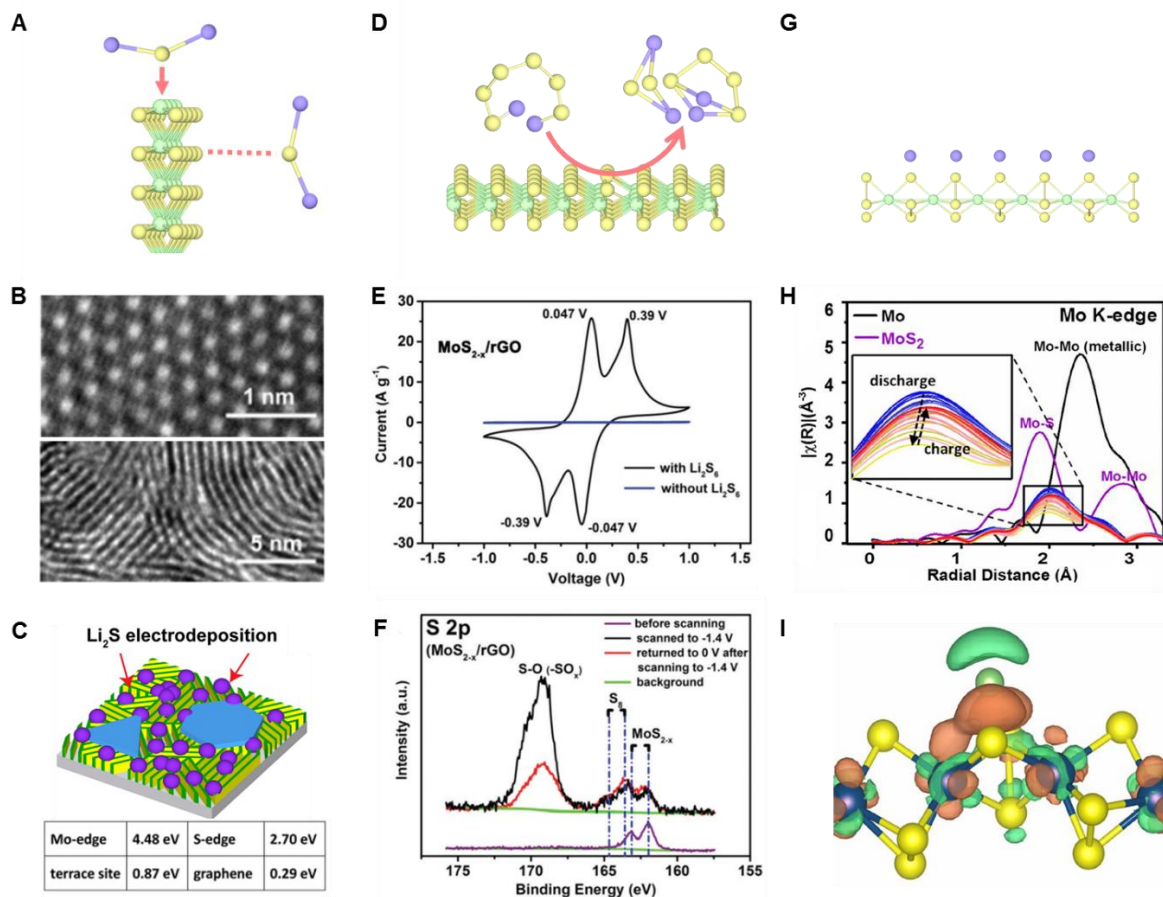
Figure 5. Molybdenum sulfides in sulfur cathodes. (A) Schematic of Li_2S adsorption on MoS_2 (Bright green, yellow and purple balls represent Mo, S and Li atoms, respectively). (B) TEM images of Horizontally aligned MoS_2 (H-MoS_2, top) and vertically aligned MoS_2 nanofilm (V-MoS_2, bottom). (C) Schematic of H-MoS_2 nanosheet on V-MoS_2 with binding energies. Reproduced with permission from Wang et al.[80] Copyright 2016 American Chemical Society. (D) Schematic of polysulfides conversion on MoS_{2-x} (Bright green, yellow and purple balls represent V, S and Li atoms, respectively). (E) CV tests of symmetric cells with MoS_{2-x}/rGO. (F) S 2p XPS spectra of MoS_{2-x}/rGO electrodes after CV tests. Reproduced with permission from Lin et al.[81] Copyright 2017 Royal Society of Chemistry. (G) Schematic of Li storage on MoS_3 (Bright green, yellow and purple balls represent Mo, S and Li atoms, respectively). (H) Fourier-transformed XAS spectrum of Mo K-edge in MoS_3 during charge and discharge comparing with those for MoS_2 and Mo. Inset image indicates slight change of Mo-S bond length during battery cycle. (I) Calculation of charge-density distribution in Li on MoS_3, where cyan, blue, and yellow balls represent Li, Mo, and S atoms, respectively, and green and brick red regions indicate depletion and accumulation of electrons. Reproduced with permission from Ye et al.[82] Copyright 2017 National Academy of Sciences.
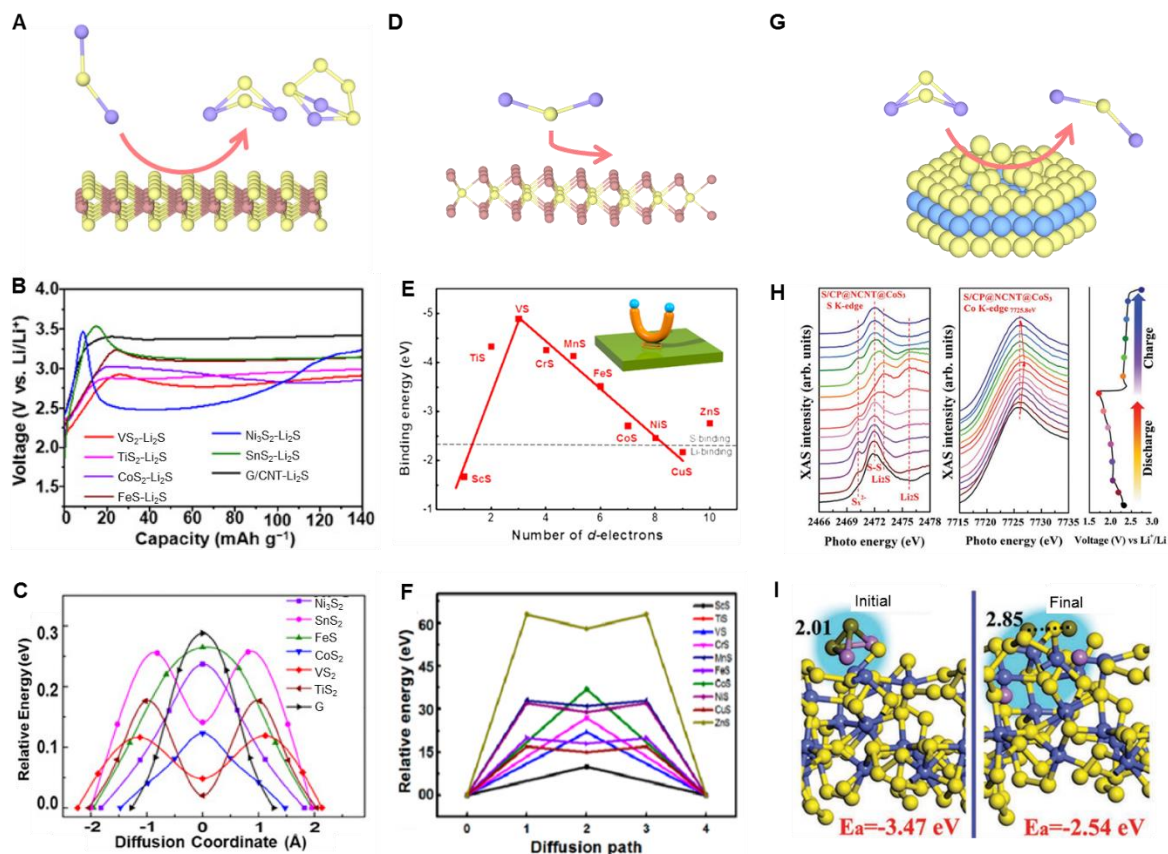
Figure 6. Other metal sulfides promoting sulfur redox in sulfur cathodes. (A) Schematic of conversion from Li₂S to the polysulfides on VS₂ (Deep pink, yellow and purple balls represent V, S and Li atoms, respectively). (B) Voltage profiles of various metal sulfides-Li₂S electrodes in the first charge process. (C) Energy for Li⁺ diffusion of on various metal sulfides and graphene. Reproduced with permission from Zhou et al.[83] Copyright 2017 National Academy of Sciences. (D) Schematic of Li₂S diffusion on VS₂ (Deep pink, yellow and purple balls represent V, S and Li atoms, respectively). (E) Periodic law of binding energy on transition metal sulfides. (F) Energy barriers of Li⁺ diffusion on transition metal sulfide surfaces. Reproduced with permission from Chen et al.[84] Copyright 2017 American Chemical Society. (G) Schematic of conversion from Li₂S₂ to Li₂S on CoS₃ (Blue, yellow and purple balls represent Co, S and Li atoms, respectively). (H) S K-edge and Co K-edge XAS of sulfur electrode with CoS₃ at different states of discharge/charge. (I) Adsorption energy (Ea) of Li₂S₂ on the surface of CoS₃. Reproduced with permission from Yang et al.[85] Copyright 2019 John Wiley Sons, Inc.
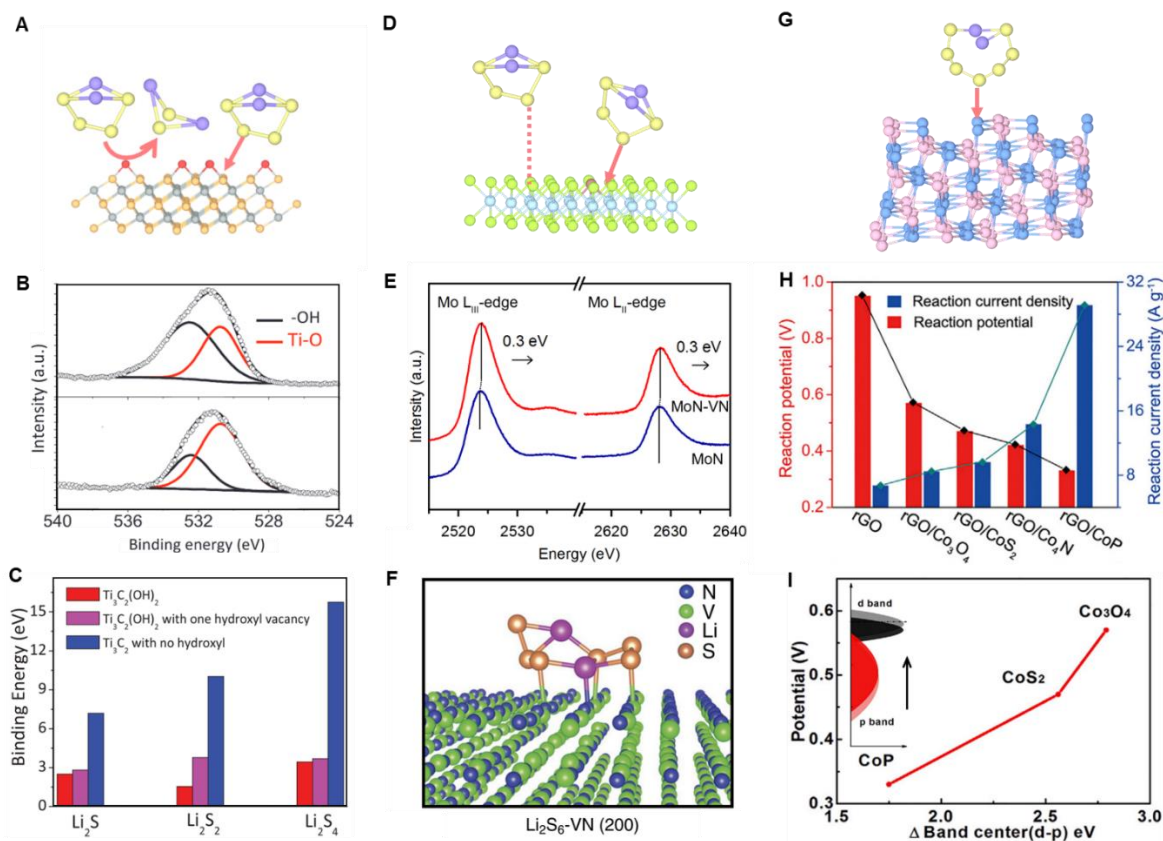
Figure 7. Other inorganics as promoters in sulfur cathodes. (A) Schematic of polysulfides adsorption and conversion on Ti_3C_2 (Grey, orange, red, yellow and purple balls represent C, Ti, O, S and Li atoms, respectively). (B) O 1s XPS spectra of Ti_3C_2 (top) and Ti_3C_2-polysulfides (bottom). (C) Variation of binding energy of lithium polysulfides bonding to respective substrates. Reproduced with permission from Liang et al.[94] Copyright 2017 John Wiley Sons, Inc. (D) Schematic of polysulfides adsorption on V-MoN (Light blue, bright green, deep pink, yellow and purple balls represent N, Mo, V, S and Li atoms, respectively). (E) Mo L-edge NEXAFS spectra of MoN-VN and MoN. Reproduced with permission from Ye et al.[95] Copyright 2018 John Wiley Sons, Inc. (F) View of Li_2S_6 on VN. Reproduced with permission from Sun et al.[96] Copyright 2017 Nature Publishing Group. (G) Schematic of polysulfides adsorption on CoP (Light pink, blue, yellow and purple balls represent P, Co, S and Li atoms, respectively). (H) Summary potential and current density for CV peak corresponding to reduction of Li_2S_6 to Li_2S for Co-based samples with various anions. (I) Relation between the Δ band (d-p) center and polysulfides redox potentials for CoP, CoS_2, and Co_3O_4, respectively. Reproduced with permission from Zhou et al.[98] Copyright 2018 Elsevier.
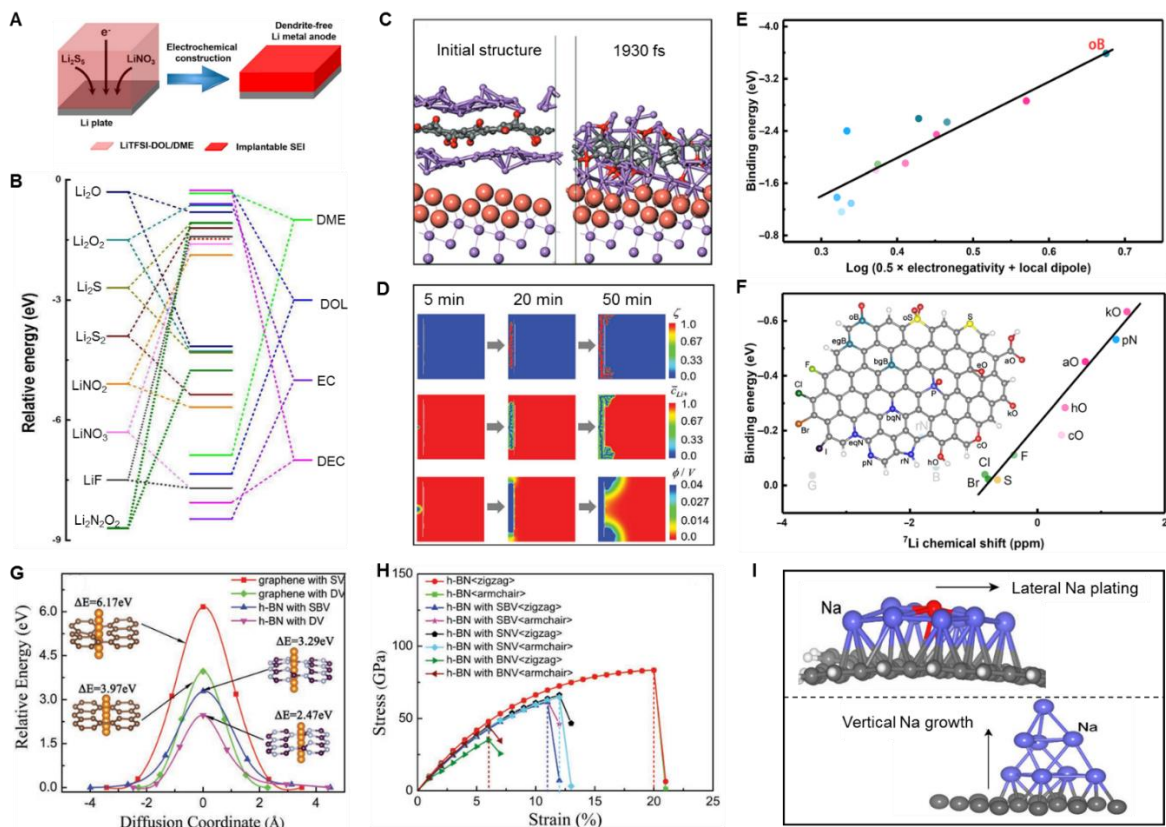
Figure 8. Combining experimental and theoretical investigations to develop Li/Na anodes. (A) Schematic of *ex-situ* SEI fabrication on the Li through electroplating. (B) HOMO and LUMO levels of SEI components and solvents. Reproduced with permission from Cheng et al.[104] Copyright 2018 Elsevier. (C) Simulation of lithiated GO on Cu surface from initial state to 1930 fs (Purple, orange, gray and red spheres represent Li, Cu, C and O atoms, respectively). (D) Simulations of Li dendrites growth with protective layer. Reproduced with permission from Foroozan et al.[110] Copyright 2018 John Wiley Sons, Inc. The relationship between Li atom binding energy and (E) log (0.5 × electronegativity + local dipole), and (F) theoretical ⁷Li chemical shift. Inset is the modeling of heteroatom-doped graphene. Reproduced with permission from Chen et al.[114] Copyright 2019 American Association for the Advancement of Science. (G) Energy curves of Na⁺ ion diffusion through defective graphene and h-BN. (H) The strain–stress relations for h-BN and defective h-BN. Reproduced with permission from Tian et al.[122] Copyright 2017 John Wiley Sons, Inc. (I) The Na growth on oxygen functionalized carbon nanotubes (top) and Cu foil surfaces (bottom) by DFT computations. Reproduced with permission from Ye et al.[124] Copyright 2019 John Wiley Sons, Inc.
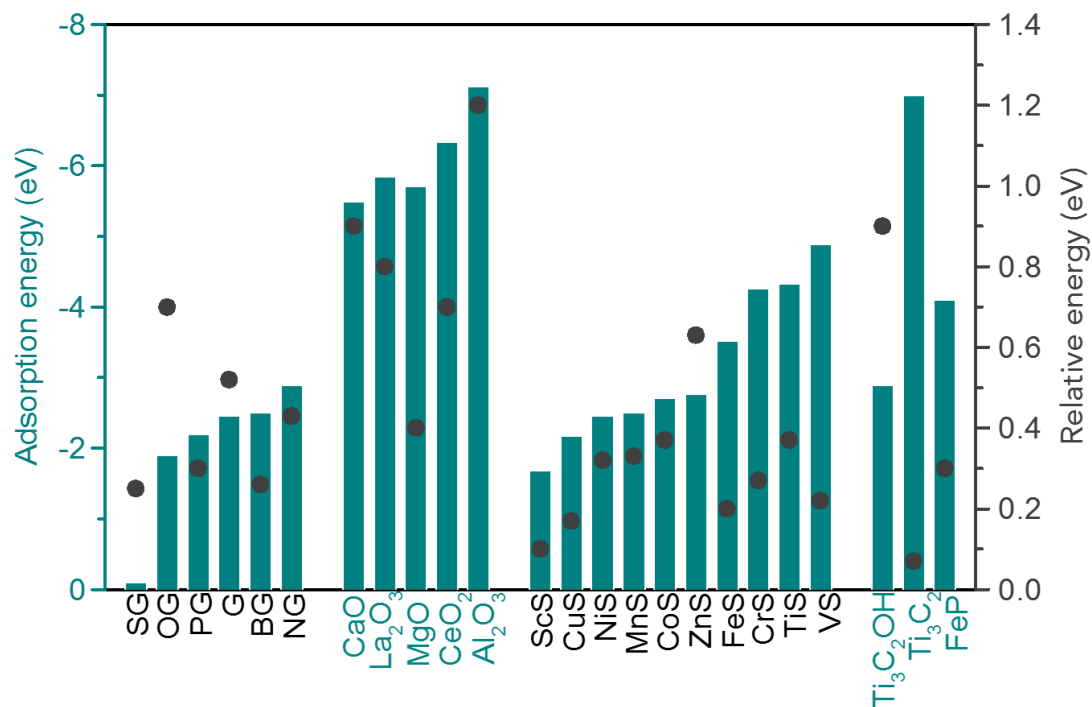
Figure 9. Summary theoretical investigation of sulfur intermediates adsorption energy, and Li ion diffusion relative energy, on various nanomaterials (represented by bars and points, respectively).
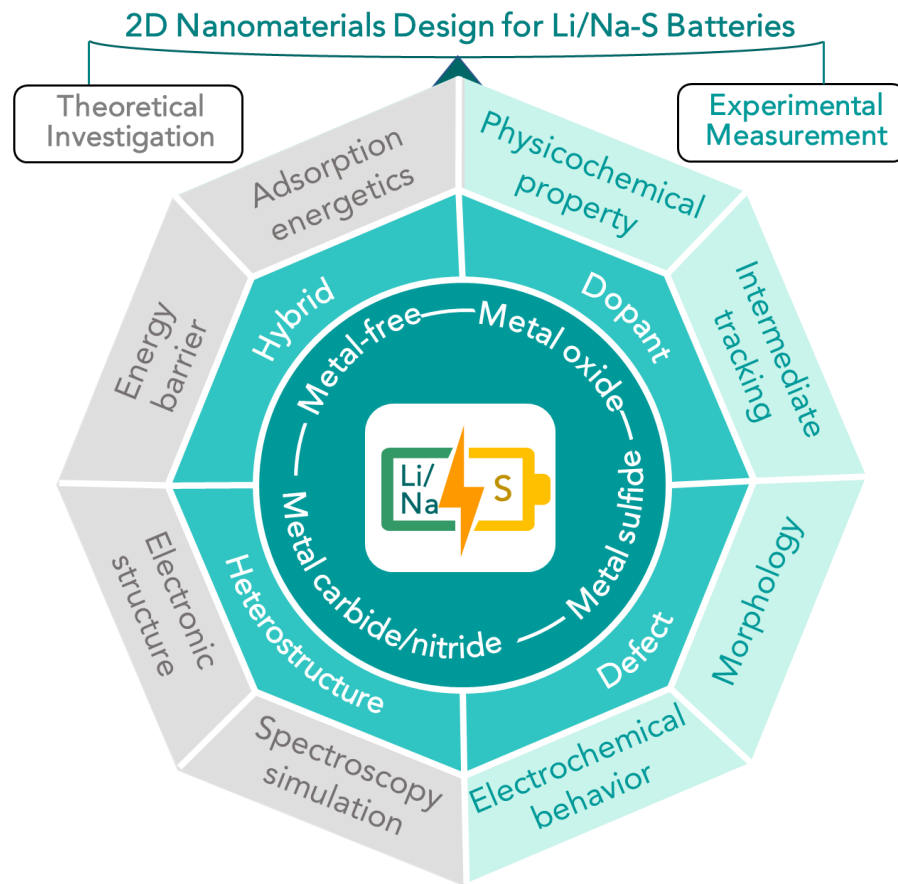
Figure 10. 2D nanomaterials design for Li/Na-S batteries through combining experimental and computational approaches.

References

1. Chung, S.-H., and Manthiram, A. (2019). Current status and future prospects of metal–sulfur batteries. Adv. Mater. *31*, 1901125.

2. Salama, M., Rosy, Attias, R., Yemini, R., Gofer, Y., Aurbach, D., and Noked, M. (2019). Metal-sulfur batteries: Overview and research methods. ACS Energy Lett. *4*, 436-446.

3. Zhou, G., Wang, D.-W., Li, F., Hou, P.-X., Yin, L., Liu, C., Lu, G.Q.M., Gentle, I.R., and Cheng, H.-M. (2012). A flexible nanostructured sulphur–carbon nanotube cathode with high rate performance for Li-S batteries. Energy Environ. Sci. *5*, 8901-8906.

4. Ji, X., Lee, K.T., and Nazar, L.F. (2009). A highly ordered nanostructured carbon–sulphur cathode for lithium–sulphur batteries. Nat. Mater. *8*, 500-506.

5. Jiang, Z., Xie, H., Wang, S., Song, X., Yao, X., and Wang, H. (2018). Perovskite membranes with vertically aligned microchannels for all-solid-state lithium batteries. Adv. Energy Mater. *8*, 1801433.

6. Chen, X., He, W., Ding, L.-X., Wang, S., and Wang, H. (2019). Enhancing interfacial contact in all solid state batteries with a cathode-supported solid electrolyte membrane framework. Energy Environ. Sci. *12*, 938-944.

7. Wang, D.-W., Zeng, Q., Zhou, G., Yin, L., Li, F., Cheng, H.-M., Gentle, I.R., and Lu, G.Q.M. (2013). Carbon–sulfur composites for Li–S batteries: Status and prospects. J. Mater. Chem. A *1*, 9382-9394.

8. Xiang, H., Chen, J., Li, Z., and Wang, H. (2011). An inorganic membrane as a separator for lithium-ion battery. J. Power Sources *196*, 8651-8655.

9. Hong, X., Mei, J., Wen, L., Tong, Y., Vasileff, A.J., Wang, L., Liang, J., Sun, Z., and Dou, S.X. (2019). Nonlithium metal-sulfur batteries: Steps toward a leap. Adv. Mater. *31*, 1802822.

10. Zhou, G., Li, F., and Cheng, H.-M. (2014). Progress in flexible lithium batteries and future prospects. Energy Environ. Sci. *7*, 1307-1338.

11. Zhou, G., Pei, S., Li, L., Wang, D.W., Wang, S., Huang, K., Yin, L.C., Li, F., and Cheng, H.M. (2014). A graphene-pure-sulfur sandwich structure for ultrafast, long-life lithium–sulfur batteries. Adv. Mater. *26*, 664-664.

12. Xu, R., Cheng, X.-B., Yan, C., Zhang, X.-Q., Xiao, Y., Zhao, C.-Z., Huang, J.-Q., and Zhang, Q. (2019). Artificial interphases for highly stable lithium metal anode. Matter *1*, 317-344.

13. Ye, C., Zhang, L., Guo, C., Li, D., Vasileff, A., Wang, H., and Qiao, S.-Z. (2017). A 3D hybrid of chemically coupled nickel sulfide and hollow carbon spheres for high performance lithium–sulfur

batteries. Adv. Funct. Mater. *27*, 1702524.

14. Zhou, G., Li, L., Wang, D.W., Shan, X.Y., Pei, S., Li, F., and Cheng, H.M. (2015). A flexible sulfur-graphene-polypropylene separator integrated electrode for advanced Li–S batteries. Adv. Mater. *27*, 641-647.

15. Chen, X., Hou, T., Persson, K.A., and Zhang, Q. (2019). Combining theory and experiment in lithium-sulfur batteries: Current progress and future perspectives. Mater. Today *22*, 142-158.

16. Chao, D., Zhou, W., Ye, C., Zhang, Q., Chen, Y., Gu, L., Davey, K., and Qiao, S.-Z. (2019). An electrolytic Zn–MnO2 battery for high-voltage and scalable energy storage. Angew. Chem. Int. Ed. *58*, 7823-7828.

17. Gu, Q., Kimpton, J.A., Brand, H.E., Wang, Z., and Chou, S. (2017). Solving key challenges in battery research using in situ synchrotron and neutron techniques. Adv. Energy Mater. *7*, 1602831.

18. Yan, Y., Cheng, C., Zhang, L., Li, Y., and Lu, J. (2019). Deciphering the reaction mechanism of lithium-sulfur batteries by in situ/operando synchrotron-based characterization techniques. Adv. Energy Mater. *9*, 1900148.

19. Shan, J., Liu, Y., Liu, P., Huang, Y., Su, Y., Wu, D., and Feng, X. (2015). Nitrogen-doped carbon-encapsulated SnO2–SnS/graphene sheets with improved anodic performance in lithium ion batteries. J. Mater. Chem. A *3*, 24148-24154.

20. Zhang, L., Liang, P., Shu, H.-b., Man, X.-l., Li, F., Huang, J., Dong, Q.-m., and Chao, D.-l. (2017). Borophene as efficient sulfur hosts for lithium–sulfur batteries: Suppressing shuttle effect and improving conductivity. J. Phys. Chem. C *121*, 15549-15555.

21. Shan, J., Liu, Y., Su, Y., Liu, P., Zhuang, X., Wu, D., Zhang, F., and Feng, X. (2016). Graphene-directed two-dimensional porous carbon frameworks for high-performance lithium–sulfur battery cathodes. J. Mater. Chem. A *4*, 314-320.

22. Li, B., Xu, H., Ma, Y., and Yang, S. (2019). Harnessing the unique properties of 2D materials for advanced lithium–sulfur batteries. Nanoscale Horiz. *4*, 77-98.

23. Chen, B., Liu, E., He, F., Shi, C., He, C., Li, J., and Zhao, N. (2016). 2D sandwich-like carbon-coated ultrathin TiO2@defect-rich MoS2 hybrid nanosheets: Synergistic-effect-promoted electrochemical performance for lithium ion batteries. Nano Energy *26*, 541-549.

24. Zhang, L., Liang, P., Shu, H.B., Man, X.L., Du, X.Q., Chao, D.L., Liu, Z.G., Sun, Y.P., Wan, H.Z., and Wang, H. (2018). Design rules of heteroatom-doped graphene to achieve high performance

lithium–sulfur batteries: Both strong anchoring and catalysing based on first principles calculation. J. Colloid Interface Sci. *529*, 426-431.

25. Jin, H., Guo, C., Liu, X., Liu, J., Vasileff, A., Jiao, Y., Zheng, Y., and Qiao, S.-Z. (2018). Emerging two-dimensional nanomaterials for electrocatalysis. Chem. Rev. *118*, 6337-6408.

26. Liu, J., Zhang, Y., Zhang, L., Xie, F., Vasileff, A., and Qiao, S.-Z. (2019). Graphitic carbon nitride (g-C3N4)-derived n-rich graphene with tuneable interlayer distance as a high-rate anode for sodium-ion batteries. Adv. Mater. *31*, 1901261.

27. Chao, D., Ouyang, B., Liang, P., Huong, T.T.T., Jia, G., Huang, H., Xia, X., Rawat, R.S., and Fan, H.J. (2018). C-plasma of hierarchical graphene survives sns bundles for ultrastable and high volumetric na-ion storage. Adv. Mater. *30*, 1804833.

28. Zhu, D., Wang, Y., Yuan, G., and Xia, H. (2014). High-performance supercapacitor electrodes based on hierarchical Ti@MnO2 nanowire arrays. Chem. Commun. *50*, 2876-2878.

29. Guo, C.X., and Li, C.M. (2017). Molecule-confined FeOx nanocrystals mounted on carbon as stable anode material for high energy density nickel-iron batteries. Nano Energy *42*, 166-172.

30. Wu, Y., and Yu, Y. (2019). 2D material as anode for sodium ion batteries: Recent progress and perspectives. Energy Storage Materials *16*, 323-343.

31. Xie, F., Zhang, L., Su, D., Jaroniec, M., and Qiao, S.Z. (2017). Na2Ti3O7@ N-doped carbon hollow spheres for sodium-ion batteries with excellent rate performance. Adv. Mater. *29*, 1700989.

32. Pei, F., Lin, L., Ou, D., Zheng, Z., Mo, S., Fang, X., and Zheng, N. (2017). Self-supporting sulfur cathodes enabled by two-dimensional carbon yolk-shell nanosheets for high-energy-density lithium-sulfur batteries. Nat. Commun. *8*, 482.

33. Xu, X., Zhou, D., Qin, X., Lin, K., Kang, F., Li, B., Shanmukaraj, D., Rojo, T., Armand, M., and Wang, G. (2018). A room-temperature sodium-sulfur battery with high capacity and stable cycling performance. Nat. Commun. *9*, 3870.

34. Zhang, B.-W., Sheng, T., Liu, Y.-D., Wang, Y.-X., Zhang, L., Lai, W.-H., Wang, L., Yang, J., Gu, Q.-F., and Chou, S.-L. (2018). Atomic cobalt as an efficient electrocatalyst in sulfur cathodes for superior room-temperature sodium-sulfur batteries. Nat. Commun. *9*, 4082.

35. Zhang, B.-W., Sheng, T., Wang, Y.-X., Chou, S., Davey, K., Dou, S.-X., and Qiao, S.-Z. (2019). Long-life room-temperature sodium–sulfur batteries by virtue of transition-metal-nanocluster–sulfur interactions. Angew. Chem. Int. Ed. *58*, 1484-1488.

36. Su, D., Cortie, M., and Wang, G. (2017). Fabrication of N-doped graphene–carbon nanotube hybrids from prussian blue for lithium–sulfur batteries. Adv. Energy Mater. *7*, 1602014.

37. Fang, R., Zhao, S., Hou, P., Cheng, M., Wang, S., Cheng, H.M., Liu, C., and Li, F. (2016). 3D interconnected electrode materials with ultrahigh areal sulfur loading for Li–S batteries. Adv. Mater. *28*, 3374-3382.

38. Wu, F., Chen, S., Srot, V., Huang, Y., Sinha, S.K., van Aken, P.A., Maier, J., and Yu, Y. (2018). A sulfur–limonene-based electrode for lithium–sulfur batteries: High-performance by self-protection. Adv. Mater. *30*, 1706643.

39. Wang, Y.-X., Yang, J., Lai, W., Chou, S.-L., Gu, Q.-F., Liu, H.K., Zhao, D., and Dou, S.X. (2016). Achieving high-performance room-temperature sodium-sulfur batteries with S@interconnected mesoporous carbon hollow nanospheres. J. Am. Chem. Soc. *138*, 16576-16579.

40. Fang, R., Zhao, S., Pei, S., Qian, X., Hou, P.-X., Cheng, H.-M., Liu, C., and Li, F. (2016). Toward more reliable lithium–sulfur batteries: An all-graphene cathode structure. ACS nano *10*, 8676-8682.

41. Hu, G., Sun, Z., Shi, C., Fang, R., Chen, J., Hou, P., Liu, C., Cheng, H.M., and Li, F. (2017). A sulfur-rich copolymer@CNT hybrid cathode with dual-confinement of polysulfides for high-performance lithium–sulfur batteries. Adv. Mater. *29*, 1603835.

42. Pang, Q., Liang, X., Kwok, C.Y., and Nazar, L.F. (2016). Advances in lithium-sulfur batteries based on multifunctional cathodes and electrolytes. Nat. Energy *1*, 16132.

43. Wang, Z., Dong, Y., Li, H., Zhao, Z., Bin Wu, H., Hao, C., Liu, S., Qiu, J., and Lou, X.W. (2014). Enhancing lithium–sulphur battery performance by strongly binding the discharge products on amino-functionalized reduced graphene oxide. Nat. Commun. *5*, 5002.

44. Wang, H., Yang, Y., Liang, Y., Robinson, J.T., Li, Y., Jackson, A., Cui, Y., and Dai, H. (2011). Graphene-wrapped sulfur particles as a rechargeable lithium–sulfur battery cathode material with high capacity and cycling stability. Nano Lett. *11*, 2644-2647.

45. Ji, L., Rao, M., Zheng, H., Zhang, L., Li, Y., Duan, W., Guo, J., Cairns, E.J., and Zhang, Y. (2011). Graphene oxide as a sulfur immobilizer in high performance lithium/sulfur cells. J. Am. Chem. Soc. *133*, 18522-18525.

46. Li, N., Zheng, M., Lu, H., Hu, Z., Shen, C., Chang, X., Ji, G., Cao, J., and Shi, Y. (2012). High-rate lithium–sulfur batteries promoted by reduced graphene oxide coating. Chem. Commun. *48*, 4106-4108.

47. Zhou, G., Yin, L.-C., Wang, D.-W., Li, L., Pei, S., Gentle, I.R., Li, F., and Cheng, H.-M. (2013). Fibrous hybrid of graphene and sulfur nanocrystals for high-performance lithium–sulfur batteries. ACS Nano *7*, 5367-5375.

48. Zu, C., and Manthiram, A. (2013). Hydroxylated graphene–sulfur nanocomposites for high-rate lithium–sulfur batteries. Adv. Energy Mater. *3*, 1008-1012.

49. Li, H., Tao, Y., Zhang, C., Liu, D., Luo, J., Fan, W., Xu, Y., Li, Y., You, C., Pan, Z.-Z.*, et al.* (2018). Dense graphene monolith for high volumetric energy density Li-S batteries. Adv. Energy Mater. *8*, 1703438.

50. Tang, C., Zhang, Q., Zhao, M.-Q., Huang, J.-Q., Cheng, X.-B., Tian, G.-L., Peng, H.-J., and Wei, F. (2014). Nitrogen-doped aligned carbon nanotube/graphene sandwiches: Facile catalytic growth on bifunctional natural catalysts and their applications as scaffolds for high-rate lithium-sulfur batteries. Adv. Mater. *26*, 6100-6105.

51. Tang, C., Li, B.-Q., Zhang, Q., Zhu, L., Wang, H.-F., Shi, J.-L., and Wei, F. (2016). CaO-templated growth of hierarchical porous graphene for high-power lithium–sulfur battery applications. Adv. Funct. Mater. *26*, 577-585.

52. Qiu, Y., Li, W., Zhao, W., Li, G., Hou, Y., Liu, M., Zhou, L., Ye, F., Li, H., and Wei, Z. (2014). High-rate, ultralong cycle-life lithium/sulfur batteries enabled by nitrogen-doped graphene. Nano Lett. *14*, 4821-4827.

53. Yin, L.-C., Liang, J., Zhou, G.-M., Li, F., Saito, R., and Cheng, H.-M. (2016). Understanding the interactions between lithium polysulfides and N-doped graphene using density functional theory calculations. Nano Energy *25*, 203-210.

54. Hou, T.Z., Chen, X., Peng, H.J., Huang, J.Q., Li, B.Q., Zhang, Q., and Li, B. (2016). Design principles for heteroatom-doped nanocarbon to achieve strong anchoring of polysulfides for lithium-sulfur batteries. Small *12*, 3283-3291.

55. Hou, T.-Z., Xu, W.-T., Chen, X., Peng, H.-J., Huang, J.-Q., and Zhang, Q. (2017). Lithium bond chemistry in lithium-sulfur batteries. Angew. Chem. Int. Ed. *56*, 8178-8182.

56. Zhou, G., Paek, E., Hwang, G.S., and Manthiram, A. (2015). Long-life Li/polysulphide batteries with high sulphur loading enabled by lightweight three-dimensional nitrogen/sulphur-codoped graphene sponge. Nat. Commun. *6*, 8760.

57. Zhang, L., Liu, D., Muhammad, Z., Wan, F., Xie, W., Wang, Y., Song, L., Niu, Z., and Chen, J.

(2019). Single nickel atoms on nitrogen-doped graphene enabling enhanced kinetics of lithium–sulfur batteries. Adv. Mater. *31*, 1903955.

58. Du, Z., Chen, X., Hu, W., Chuang, C., Xie, S., Hu, A., Yan, W., Kong, X., Wu, X., and Ji, H. (2019). Cobalt in nitrogen-doped graphene as single-atom catalyst for high-sulphur content lithium-sulphur batteries. J. Am. Chem. Soc. *141*, 3977-3985.

59. Liu, J., Li, W., Duan, L., Li, X., Ji, L., Geng, Z., Huang, K., Lu, L., Zhou, L., and Liu, Z. (2015). A graphene-like oxygenated carbon nitride material for improved cycle-life lithium/sulfur batteries. Nano Lett. *15*, 5137-5142.

60. Pang, Q., and Nazar, L.F. (2016). Long-life and high-areal-capacity Li–S batteries enabled by a light-weight polar host with intrinsic polysulfide adsorption. ACS nano *10*, 4111-4118.

61. Liang, J., Yin, L., Tang, X., Yang, H., Yan, W., Song, L., Cheng, H.-M., and Li, F. (2016). Kinetically enhanced electrochemical redox of polysulfides on polymeric carbon nitrides for improved lithium-sulfur batteries. ACS Appl. Mater. Interfaces *8*, 25193-25201.

62. Pang, Q., Liang, X., Kwok, C.Y., Kulisch, J., and Nazar, L.F. (2016). A comprehensive approach toward stable lithium–sulfur batteries with high volumetric energy density. Adv. Energy Mater. *7*, 1601630.

63. Du, H., Zhang, Z., He, J., Cui, Z., Chai, J., Ma, J., Yang, Z., Huang, C., and Cui, G. (2017). A delicately designed sulfide graphdiyne compatible cathode for high-performance lithium/magnesium–sulfur batteries. Small *13*, 1702277.

64. Sun, J., Sun, Y., Pasta, M., Zhou, G., Li, Y., Liu, W., Xiong, F., and Cui, Y. (2016). Entrapment of polysulfides by a black-phosphorus-modified separator for lithium–sulfur batteries. Adv. Mater. *28*, 9797–9803.

65. Ma, D., Li, Y., Yang, J., Mi, H., Luo, S., Deng, L., Yan, C., Rauf, M., Zhang, P., Sun, X., *et al.* (2018). New strategy for polysulfide protection based on atomic layer deposition of TiO2 onto ferroelectric-encapsulated cathode: Toward ultrastable free-standing room temperature sodium–sulfur batteries. Adv. Funct. Mater. *28*, 1705537.

66. Li, Z., Zhang, J., and Lou, X.W.D. (2015). Hollow carbon nanofibers filled with MnO2 nanosheets as efficient sulfur hosts for lithium–sulfur batteries. Angew. Chem. Int. Ed. *54*, 12886-12890.

67. Zhang, J., Hu, H., Li, Z., and Lou, X.W.D. (2016). Double‐shelled nanocages with cobalt hydroxide inner shell and layered double hydroxides outer shell as high‐efficiency polysulfide

mediator for lithium–sulfur batteries. Angew. Chem. Int. Ed. *55*, 3982-3986.

68. Yu, M., Yuan, W., Li, C., Hong, J.-D., and Shi, G. (2014). Performance enhancement of a graphene–sulfur composite as a lithium–sulfur battery electrode by coating with an ultrathin Al2O3 film via atomic layer deposition. J. Mater. Chem. A *2*, 7360-7366.

69. Fan, Q., Liu, W., Weng, Z., Sun, Y., and Wang, H. (2015). Ternary hybrid material for high-performance lithium–sulfur battery. J. Am. Chem. Soc. *137*, 12946-12953.

70. Pang, Q., Kundu, D., Cuisinier, M., and Nazar, L. (2014). Surface-enhanced redox chemistry of polysulphides on a metallic and polar host for lithium-sulphur batteries. Nat. Commun. *5*, 4759.

71. Liang, X., Hart, C., Pang, Q., Garsuch, A., Weiss, T., and Nazar, L.F. (2015). A highly efficient polysulfide mediator for lithium–sulfur batteries. Nat. Commun. *6*, 6682.

72. Tao, X., Wang, J., Liu, C., Wang, H., Yao, H., Zheng, G., Seh, Z.W., Cai, Q., Li, W., and Zhou, G. (2016). Balancing surface adsorption and diffusion of lithium-polysulfides on nonconductive oxides for lithium-sulfur battery design. Nat. Commun. *7*, 11203.

73. Patil, S.B., Kim, H.J., Lim, H.-K., Oh, S.M., Kim, J., Shin, J., Kim, H., Choi, J.W., and Hwang, S.-J. (2018). Exfoliated 2D lepidocrocite titanium oxide nanosheets for high sulfur content cathodes with highly stable Li–S battery performance. ACS Energy Lett. *3*, 412-419.

74. Xu, L., Zhao, H., Sun, M., Huang, B., Wang, J., Xia, J., Li, N., Yin, D., Luo, M., Luo, F*., et al.* (2019). Oxygen vacancies on layered niobic acid that weaken the catalytic conversion of polysulfides in lithium-sulfur batteries. Angew. Chem. Int. Ed. *58*, 11491-11496.

75. Zhu, C., Gao, D., Ding, J., Chao, D., and Wang, J. (2018). Tmd-based highly efficient electrocatalysts developed by combined computational and experimental approaches. Chem. Soc. Rev. *47*, 4332-4356.

76. Xu, J., Zhang, W., Fan, H., Cheng, F., Su, D., and Wang, G. (2018). Promoting lithium polysulfide/sulfide redox kinetics by the catalyzing of zinc sulfide for high performance lithium-sulfur battery. Nano Energy *51*, 73-82.

77. Tian, Y., Huang, H., Liu, G., Bi, R., and Zhang, L. (2019). Metal–organic framework derived yolk–shell NiS2/carbon spheres for lithium–sulfur batteries with enhanced polysulfide redox kinetics. Chem. Commun. *55*, 3243-3246.

78. Pang, Q., Kundu, D., and Nazar, L.F. (2016). A graphene-like metallic cathode host for long-life and high-loading lithium–sulfur batteries. Mater. Horiz. *3*, 130.

79. Seh, Z.W., Yu, J.H., Li, W., Hsu, P.-C., Wang, H., Sun, Y., Yao, H., Zhang, Q., and Cui, Y. (2014).

Two-dimensional layered transition metal disulphides for effective encapsulation of high-capacity lithium sulphide cathodes. Nat. Commun. *5*, 5017.

80. Wang, H., Zhang, Q., Yao, H., Liang, Z., Lee, H.-W., Hsu, P.-C., Zheng, G., and Cui, Y. (2014). High electrochemical selectivity of edge versus terrace sites in two-dimensional layered MoS2 materials. Nano Lett. *14*, 7138-7144.

81. Lin, H., Yang, L., Jiang, X., Li, G., Zhang, T., Yao, Q., Zheng, G.W., and Lee, J.Y. (2017). Electrocatalysis of polysulfide conversion by sulfur-deficient MoS2 nanoflakes for lithium–sulfur batteries. Energy Environ. Sci. *10*, 1476-1486.

82. Ye, H., Ma, L., Zhou, Y., Wang, L., Han, N., Zhao, F., Deng, J., Wu, T., Li, Y., and Lu, J. (2017). Amorphous MoS3 as the sulfur-equivalent cathode material for room-temperature Li–S and Na–S batteries. Proc. Natl. Acad. Sci. U. S. A. *114*, 13091-13096.

83. Zhou, G., Tian, H., Jin, Y., Tao, X., Liu, B., Zhang, R., Seh, Z.W., Zhuo, D., Liu, Y., and Sun, J. (2017). Catalytic oxidation of Li2S on the surface of metal sulfides for Li−S batteries. Proc. Natl. Acad. Sci. U. S. A. *114*, 840-845.

84. Chen, X., Peng, H.-J., Zhang, R., Hou, T.-Z., Huang, J.-Q., Li, B., and Zhang, Q. (2017). An analogous periodic law for strong anchoring of polysulfides on polar hosts in lithium sulfur batteries: S- or Li-binding on first-row transition-metal sulfides? ACS Energy Lett. *2*, 795-801.

85. Yang, X., Gao, X., Sun, Q., Jand, S.P., Yu, Y., Zhao, Y., Li, X., Adair, K., Kuo, L.-Y., Rohrer, J.*, et al.* (2019). Promoting the transformation of Li2S2 to Li2S: Significantly increasing utilization of active materials for high-sulfur-loading Li–S batteries. Adv. Mater. *31*, 1901220.

86. Tian, M., Pei, F., Yao, M., Fu, Z., Lin, L., Wu, G., Xu, G., Kitagawa, H., and Fang, X. (2018). Ultrathin MOF nanosheet assembled highly oriented microporous membrane as an interlayer for lithium-sulfur batteries. Energy Storage Materials *21*, 14-21.

87. Chen, G., Song, X., Wang, S., Chen, X., and Wang, H. (2018). Two-dimensional molybdenum nitride nanosheets modified celgard separator with multifunction for lis batteries. J. Power Sources *408*, 58-64.

88. Xiao, X., Wang, H., Bao, W., Urbankowski, P., Yang, L., Yang, Y., Maleski, K., Cui, L., Billinge, S.J.L., Wang, G.*, et al.* (2019). Two-dimensional arrays of transition metal nitride nanocrystals. Adv. Mater. *31*, 1902393.

89. Bai, L., Chao, D., Xing, P., Tou, L.J., Chen, Z., Jana, A., Shen, Z.X., and Zhao, Y. (2016). Refined sulfur nanoparticles immobilized in metal–organic polyhedron as stable cathodes for Li–S battery.

ACS Appl. Mater. Interfaces *8*, 14328-14333.

90. Yao, Y., Feng, W., Chen, M., Zhong, X., Wu, X., Zhang, H., and Yu, Y. (2018). Boosting the electrochemical performance of Li–S batteries with a dual polysulfides confinement strategy. Small *14*, 1802516.

91. Xu, J., Lawson, T., Fan, H., Su, D., and Wang, G. (2018). Updated metal compounds (MOFs, S, OH, N, C) used as cathode materials for lithium–sulfur batteries. Adv. Energy Mater. *8*, 1702607-1702629.

92. Wang, J., Zhao, T., Yang, Z., Chen, Y., Liu, Y., Wang, J., Zhai, P., and Wu, W. (2019). MXene-based Co, N-codoped porous carbon nanosheets regulating polysulfides for high-performance lithium–sulfur batteries. ACS Appl. Mater. Interfaces. *11,* 38654-38662.

93. Zhao, T., Zhai, P., Yang, Z., Wang, J., Qu, L., Du, F., and Wang, J. (2018). Self-supporting Ti3C2Tx foam/s cathodes with high sulfur loading for high-energy-density lithium–sulfur batteries. Nanoscale *10*, 22954-22962.

94. Liang, X., Rangom, Y., Kwok, C.Y., Pang, Q., and Nazar, L.F. (2016). Interwoven MXene nanosheet/carbon-nanotube composites as Li–S cathode hosts. Adv. Mater. *29*, 1603040.

95. Ye, C., Jiao, Y., Jin, H., Slattery, A.D., Davey, K., Wang, H., and Qiao, S.-Z. (2018). 2D MoN-VN heterostructure to regulate polysulfides for highly efficient lithium-sulfur batteries. Angew. Chem. Int. Ed. *57*, 16703-16707.

96. Sun, Z., Zhang, J., Yin, L., Hu, G., Fang, R., Cheng, H.-M., and Li, F. (2017). Conductive porous vanadium nitride/graphene composite as chemical anchor of polysulfides for lithium-sulfur batteries. Nat. Commun. *8*, 14627.

97. You, B., Tang, M.T., Tsai, C., Abild-Pedersen, F., Zheng, X., and Li, H. (2019). Enhancing electrocatalytic water splitting by strain engineering. Adv. Mater. *31*, 1807001.

98. Zhou, J., Liu, X., Zhu, L., Zhou, J., Guan, Y., Chen, L., Niu, S., Cai, J., Sun, D., Zhu, Y*., et al.* (2018). Deciphering the modulation essence of p bands in Co-based compounds on Li-S chemistry. Joule *2*, 2681-2693.

99. Pang, Q., Kwok, C.Y., Kundu, D., Liang, X., and Nazar, L.F. (2019). Lightweight metallic MgB2 mediates polysulfide redox and promises high-energy-density lithium-sulfur batteries. Joule *3*, 136-148.

100. Cao, R., Xu, W., Lv, D., Xiao, J., and Zhang, J.G. (2015). Anodes for rechargeable lithium-sulfur

batteries. Adv. Energy Mater. *5*, 1402273.

101. Zhao, Y., Goncharova, L.V., Lushington, A., Sun, Q., Yadegari, H., Wang, B., Xiao, W., Li, R., and Sun, X. (2017). Superior stable and long life sodium metal anodes achieved by atomic layer deposition. Adv. Mater. *29*, 1606663.

102. Pei, F., Fu, A., Ye, W., Peng, J., Fang, X., Wang, M.-S., and Zheng, N. (2019). Robust lithium metal anodes realized by lithiophilic 3D porous current collectors for constructing high-energy lithium–sulfur batteries. ACS Nano *13*, 8337-8346.

103. Cheng, X.-B., Huang, J.-Q., and Zhang, Q. (2018). Li metal anode in working lithium-sulfur batteries. J. Electrochem. Soc. *165*, A6058-A6072.

104. Cheng, X.-B., Yan, C., Chen, X., Guan, C., Huang, J.-Q., Peng, H.-J., Zhang, R., Yang, S.-T., and Zhang, Q. (2017). Implantable solid electrolyte interphase in lithium-metal batteries. Chem *2*, 258-270.

105. Aurbach, D., Pollak, E., Elazari, R., Salitra, G., Kelley, C.S., and Affinito, J. (2009). On the surface chemical aspects of very high energy density, rechargeable Li–sulfur batteries. J. Electrochem. Soc. *156*, A694-A702.

106. Ma, G., Wen, Z., Wu, M., Shen, C., Wang, Q., Jin, J., and Wu, X. (2014). A lithium anode protection guided highly-stable lithium–sulfur battery. Chem. Commun. *50*, 14209-14212.

107. Zheng, G., Lee, S.W., Liang, Z., Lee, H.-W., Yan, K., Yao, H., Wang, H., Li, W., Chu, S., and Cui, Y. (2014). Interconnected hollow carbon nanospheres for stable lithium metal anodes. Nat. Nanotechnol. *9*, 618-623.

108. Qian, J., Henderson, W.A., Xu, W., Bhattacharya, P., Engelhard, M., Borodin, O., and Zhang, J.-G. (2015). High rate and stable cycling of lithium metal anode. Nat. Commun. *6*, 6362.

109. Liang, Z., Lin, D., Zhao, J., Lu, Z., Liu, Y., Liu, C., Lu, Y., Wang, H., Yan, K., and Tao, X. (2016). Composite lithium metal anode by melt infusion of lithium into a 3D conducting scaffold with lithiophilic coating. Proc. Natl. Acad. Sci. U. S. A. *113*, 2862-2867.

110. Foroozan, T., Soto, F.A., Yurkiv, V., Sharifi-Asl, S., Deivanayagam, R., Huang, Z., Rojaee, R., Mashayek, F., Balbuena, P.B., and Shahbazian-Yassar, R. (2018). Synergistic effect of graphene oxide for impeding the dendritic plating ofLli. Adv. Funct. Mater. *28*, 1705917.

111. Kim, M.S., Ryu, J.-H., Deepika, Lim, Y.R., Nah, I.W., Lee, K.-R., Archer, L.A., and Il Cho, W. (2018). Langmuir–blodgett artificial solid-electrolyte interphases for practical lithium metal batteries. Nat. Energy *3*, 889-898.

112. Lin, D., Liu, Y., Liang, Z., Lee, H.-W., Sun, J., Wang, H., Yan, K., Xie, J., and Cui, Y. (2016). Layered reduced graphene oxide with nanoscale interlayer gaps as a stable host for lithium metal anodes. Nat. Nanotechnol. *11*, 626.

113. Zhang, R., Chen, X.-R., Chen, X., Cheng, X.-B., Zhang, X.-Q., Yan, C., and Zhang, Q. (2017). Lithiophilic sites in doped graphene guide uniform lithium nucleation for dendrite-free lithium metal anodes. Angew. Chem. Int. Ed. *56*, 7764-7768.

114. Chen, X., Chen, X.-R., Hou, T.-Z., Li, B.-Q., Cheng, X.-B., Zhang, R., and Zhang, Q. (2019). Lithiophilicity chemistry of heteroatom-doped carbon to guide uniform lithium nucleation in lithium metal anodes. Sci. Adv. *5*, eaau7728.

115. Lu, Z., Liang, Q., Wang, B., Tao, Y., Zhao, Y., Lv, W., Liu, D., Zhang, C., Weng, Z., Liang, J.*, et al.* (2019). Graphitic carbon nitride induced micro-electric field for dendrite-free lithium metal anodes. Adv. Energy Mater. *9*, 1803186.

116. Lee, B., Paek, E., Mitlin, D., and Lee, S.W. (2019). Sodium metal anodes: Emerging solutions to dendrite growth. Chem. Rev. *119*, 5416-5460.

117. Zhao, Y., Adair, K.R., and Sun, X. (2018). Recent developments and insights into the understanding of Na metal anodes for Na-metal batteries. Energy Environ. Sci. *11*, 2673-2695.

118. Zhao, Y., Goncharova, L.V., Zhang, Q., Kaghazchi, P., Sun, Q., Lushington, A., Wang, B., Li, R., and Sun, X. (2017). Inorganic–organic coating via molecular layer deposition enables long life sodium metal anode. Nano Lett. *17*, 5653-5659.

119. Luo, J., Wang, C., Wang, H., Hu, X., Matios, E., Lu, X., Zhang, W., Tao, X., and Li, W. (2019). Pillared MXene with ultralarge interlayer spacing as a stable matrix for high performance sodium metal anodes. Adv. Funct. Mater. *29*, 1805946.

120. Tang, S., Zhang, Y.-Y., Zhang, X.-G., Li, J.-T., Wang, X.-Y., Yan, J.-W., Wu, D.-Y., Zheng, M.-S., Dong, Q.-F., and Mao, B.-W. (2019). Stable Na plating and stripping electrochemistry promoted by in situ construction of an alloy-based sodiophilic interphase. Adv. Mater. *31*, 1807495.

121. Wang, A., Hu, X., Tang, H., Zhang, C., Liu, S., Yang, Y.-W., Yang, Q.-H., and Luo, J. (2017). Processable and moldable sodium-metal anodes. Angew. Chem. Int. Ed. *56*, 11921-11926.

122. Tian, H., Seh, Z.W., Yan, K., Fu, Z., Tang, P., Lu, Y., Zhang, R., Legut, D., Cui, Y., and Zhang, Q. (2017). Theoretical investigation of 2D layered materials as protective films for lithium and sodium metal anodes. Adv. Energy Mater. *7*, 1602528.

123. Liu, W., Li, P., Wang, W., Zhu, D., Chen, Y., Pen, S., Paek, E., and Mitlin, D. (2018). Directional

flow-aided sonochemistry yields graphene with tunable defects to provide fundamental insight on sodium metal plating behavior. ACS Nano *12*, 12255-12268.

124. Ye, L., Liao, M., Zhao, T., Sun, H., Zhao, Y., Sun, X., Wang, B., and Peng, H. (2019). Sodiophilic interphase mediated, dendrite-free anode with ultrahigh specific capacity for sodium-metal batteries. Angew. Chem. Int. Ed. *131*, 2-9.

125. Liu, Z., Bertolini, S., Balbuena, P.B., and Mukherjee, P.P. (2016). Li2S film formation on lithium anode surface of Li–S batteries. ACS Appl. Mater. Interfaces *8*, 4700-4708.

126. Burgos, J.C., Balbuena, P.B., and Montoya, J.A. (2017). Structural dependence of the sulfur reduction mechanism in carbon-based cathodes for lithium–sulfur batteries. J. Phys. Chem. C *121*, 18369-18377.

127. Perez Beltran, S., and Balbuena, P.B. (2018). First-principles explorations of the electrochemical lithiation dynamics of a multilayer graphene nanosheet-based sulfur–carbon composite. J. Mater. Chem. A *6*, 18084-18094.

TOC
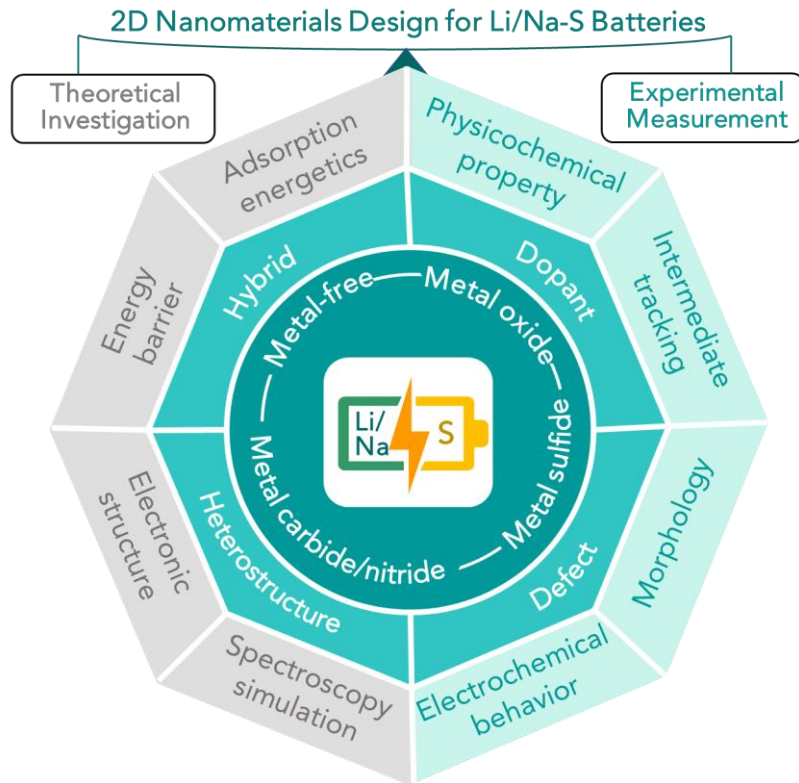
Chapter 3 A Three-Dimensional Hybrid of Chemically Coupled Nickel Sulfide and Hollow Carbon Spheres for High Performance Lithium-Sulfur Batteries

3.1. Introduction and Significance

Lithium-sulfur batteries are regarded as one of the most promising next generation batteries. However, their performance is limited by the loss of active material and the low conductivity of sulfur. Metal sulfide and its hybrids can potentially serve as sulfur hosts to effectively solve these issues. However, conventional methods produce metal sulfides with large size and poor distribution, limiting the performance of the lithium-sulfur batteries. Moreover, sluggish charge transfer at the interface of the metal sulfide and carbon results in limited redox efficiency of the polysulfides.

Our study presents a new method to produce a three-dimensional (3D) hybrid of nickel sulfide and carbon hollow spheres with strong chemical coupling, achieving a unique 3D nanostructure of nanosized nickel sulfide uniformly distributed on carbon hollow spheres. The hybrid electrode realized a sulfur loading of 2.3 mg cm-2, a high capacity of 695 mA h g-1 after 300 cycles at 0.5C, and a low capacity decay of 0.013% per cycle. This new hybrid system provides new routes to engineer sulfur hosts for lithium-sulfur systems. The highlights of this work include:

1. New method. An in situ thermal reduction and sulfidation method was applied to hybridize nickel sulfide and hollow nanocarbon which is different from conventional methods.

2. Unique structure. A unique 3D hybrid material of nickel sulfide and carbon hollow spheres was produced as a sulfur host with nanosized nickel sulfide uniformly distributed on hollow carbon spheres.

3. Chemical coupling. Strong C-S chemical coupling between nickel sulfide and nanocarbon derived from the new method further enhances the charge transfer and redox kinetics of the electrode.

4. High performance. The hybrid as a sulfur host promises high retention of sulfur and high conductivity, leading to high performance lithium-sulfur batteries (0.013% capacity decay per cycle at 0.5 C).

3.2. A Three-Dimensional Hybrid of Chemically Coupled Nickel Sulfide and Hollow Carbon Spheres for High Performance Lithium-Sulfur Batteries

This section is included as a submitted manuscript by Chao Ye, Lei Zhang, Chunxian Guo, Dongdong Li, Anthony Vasileff, Haihui Wang, and Shi-Zhang Qiao, A Three-dimensional Hybrid of Chemically Coupled Nickel Sulfide and Hollow Carbon Spheres for High Performance Lithium-sulfur Batteries, Advanced Functional Materials, 2017, 27(33), 1702524.

Statement of Authorship

Title of Paper	A Three-Dimensional Hybrid of Chemically Coupled Nickel Sulfide and Hollow Carbon Spheres for High Performance Lithium-Sulfur Batteries
Publication Status	☑ Published ☐ Accepted for Publication ☐ Submitted for Publication ☐ Unpublished and Unsubmitted work written in manuscript style
Publication Details	Lithium-sulfur batteries are a promising next-generation energy storage device owing to their high theoretical capacity and the low cost and abundance of sulfur. However, the low conductivity and loss of active sulfur material during operation greatly limits the rating capabilities and cycling stability of lithium-sulfur batteries. In this work, a unique sulfur host hybrid material comprising nanosized nickel sulfide (NiS) uniformly distributed on three-dimensional (3D) carbon hollow spheres (C-HS) is fabricated using an in situ thermal reduction and sulfidation method. In the hybrid material, the nanosized NiS provides a high adsorption capability for polysulfides and the C-HS serves as a physical confinement for polysulfides and also a 3D electron transfer pathway. Moreover, NiS has strong chemical coupling with the C-HS, favouring fast charge transfer and redox kinetics of the sulfur electrode. With a sulfur loading of up to 2.3 mg cm^{-2}, the hybrid material-based lithium-sulfur batteries offer a capacity decay as low as 0.013% per cycle and a capacity of 695 mA h g^{-1} at 0.5 C after 300 cycles. This unique 3D hybrid material with strong chemical coupling provides a promising sulfur host for high performance lithium-sulfur batteries.

Principal Author

Name of Principal Author (Candidate)	Chao Ye
Contribution to the Paper	Chao Ye performed the experiments and wrote the manuscript.
Overall percentage (%)	60%
Certification:	This paper reports on original research I conducted during the period of my Higher Degree by Research candidature and is not subject to any obligations or contractual agreements with a third party that would constrain its inclusion in this thesis. I am the primary author of this paper.
Signature	Date 2019. 10.31

Co-Author Contributions

By signing the Statement of Authorship, each author certifies that:

    i.   the candidate's stated contribution to the publication is accurate (as detailed above);

    ii.   permission is granted for the candidate in include the publication in the thesis; and

    iii.   the sum of all co-author contributions is equal to 100% less the candidate's stated contribution.

Name of Co-Author	Shi-Zhang Qiao
Contribution to the Paper	Prof. Shi-Zhang Qiao conceived the project, proposed the concept and prepared the manuscript.
Signature	Date 31/10/2019

Name of Co-Author	Haihui Wang
Contribution to the Paper	Prof. Haihui Wang conceived the project, proposed the concept and prepared the manuscript.
Signature		Date	2019.10.31

Name of Co-Author	Lei Zhang
Contribution to the Paper	Prof. Lei Zhang guided the material synthesis.
Signature		Date	2019.10.31

Name of Co-Author	Chunxian Guo
Contribution to the Paper	Prof. Chunxian Guo guided the experiments and prepared the manuscript.
Signature		Date	2019.10.31

Name of Co-Author	Dongdong Li
Contribution to the Paper	Dongdong Li prepared the manuscript.
Signature		Date	2019.10.31

Name of Co-Author	Anthony Vasileff
Contribution to the Paper	Anthony Vasileff prepared the manuscript.
Signature		Date	2019.10.31

60

A 3D Hybrid of Chemically Coupled Nickel Sulfide and Hollow Carbon Spheres for High Performance Lithium–Sulfur Batteries

Chao Ye, Lei Zhang, Chunxian Guo, Dongdong Li, Anthony Vasileff, Haihui Wang,* and Shi-Zhang Qiao*

Lithium–sulfur batteries are a promising next-generation energy storage device owing to their high theoretical capacity and the low cost and abundance of sulfur. However, the low conductivity and loss of active sulfur material during operation greatly limit the rating capabilities and cycling stability of lithium–sulfur batteries. In this work, a unique sulfur host hybrid material comprising nanosized nickel sulfide (NiS) uniformly distributed on 3D carbon hollow spheres (C-HS) is fabricated using an in situ thermal reduction and sulfidation method. In the hybrid material, the nanosized NiS provides a high adsorption capability for polysulfides and the C-HS serves as a physical confinement for polysulfides and also a 3D electron transfer pathway. Moreover, NiS has strong chemical coupling with the C-HS, favoring fast charge transfer and redox kinetics of the sulfur electrode. With a sulfur loading of up to 2.3 mg cm^{-2}, the hybrid material-based lithium–sulfur batteries offer a capacity decay as low as 0.013% per cycle and a capacity of 695 mA h g^{-1} at 0.5 C after 300 cycles. This unique 3D hybrid material with strong chemical coupling provides a promising sulfur host for high performance lithium–sulfur batteries.

1. Introduction

As a promising alternative to existing lithium–ion batteries, lithium–sulfur batteries have a high theoretical specific capacity of around 1675 mA h g^{-1}. In addition, the active sulfur material in lithium–sulfur batteries is highly abundant, low cost, and low in toxicity, making it a great potential candidate for practical applications.[1] However, performance of lithium–sulfur batteries is largely affected by the low conductivity of sulfur, the solubility of the intermediate lithium polysulfides (Li$_2$S$_x$, $2 < x \leq 8$), and the pulverization of the cathode arising from large volume expansion during discharge. Although enormous research efforts have been devoted to address these issues, including modulating the cathode structure,[2] decorating the separator,[3] and developing new electrolyte recipes/additives,[4] the cycle life and Coulombic efficiency (CE) of lithium–sulfur batteries are still not satisfactory.[5] Thus, a rational design of proper sulfur host materials to further promote high utilization and retention of active sulfur is required to achieve high performance lithium–sulfur batteries.

It has been realized that some inorganic materials including transition-metal oxides,[6] sulfides,[7] carbides,[8] and hydroxides can offer abundant adsorption sites to chemically adsorb polysulfides,[9] retaining their capability as effective sulfur hosts. In particular, metal sulfides represent a promising sulfur host owing to their strong sulfiphilicity. Moreover, metal sulfides can act as catalysts to promote redox kinetics of polysulfides during the discharge process, which derives from their multitude of possible stoichiometric compositions, crystal structures, and valence states.[10] For instance, micrometer size metal sulfides have been fabricated and used as a sulfur host in lithium–sulfur batteries. Specifically, amorphous NiS$_2$ with a continuous structure was used to adsorb soluble polysulfides and to accommodate insoluble active sulfur materials, achieving 77% retention of the initial capacity after 1200 cycles at 0.5 A g^{-1}.[11] Nevertheless, the large particle size limits the specific surface area and adsorption site density of the materials, making it difficult to load large amounts of sulfur for efficient utilization. Recently, 2D Co$_9$S$_8$ was reported to have high binding energy (6.93 eV) with Li$_2$S owing to a strong binding effect from both metal and sulfide ions.[7] Although exhibiting improved adsorption of sulfur to some extent and efficient charge transfer within the layer, 2D metal sulfides generally have poor charge transfer between the layers. In addition, the 2D materials easily aggregate when preparing the sulfur electrode. Therefore, the fabrication of metal sulfide-based materials with favorable nanostructure and charge transfer pathways should be useful

C. Ye, Dr. L. Zhang, Dr. C. X. Guo, A. Vasileff, Prof. S.-Z. Qiao
School of Chemical Engineering
The University of Adelaide
Adelaide, SA 5005, Australia
E-mail: s.qiao@adelaide.edu.au
D. D. Li, Prof. H. H. Wang
School of Chemistry and Chemical Engineering
South China University of Technology
Guangzhou 510640, China
E-mail: hhwang@scut.edu.cn

The ORCID identification number(s) for the author(s) of this article can be found under https://doi.org/10.1002/adfm.201702524.

in enabling both high adsorption capability for polysulfides and efficient charge transfer.

Hybrid materials of metal sulfides and carbons that can provide a conductive scaffold and a high adsorption capacity for polysulfides have been widely used as sulfur hosts in lithium–sulfur batteries. For instance, CoS_2 synthesized by a hydrothermal method was mechanically mixed with graphene as a sulfur host. This mitigated the polarization of the lithium–sulfur batteries and promoted a 10% increase in efficiency.[12] Recently, a hybrid material of WS_2 nanosheets and a carbon nanofiber (CNF) matrix was fabricated and used as a sulfur host.[13] This hybrid material demonstrated 90% specific capacity retention after 1500 cycles at 2 C, which was attributed to the conductivity of the CNF and the chemical adsorption of polysulfides on the WS_2 nanosheets. Although enhancing the redox reactions on the sulfur electrode, hybridization of metal sulfides and carbons (by mechanically mixing the two components or hydrothermal growth of metal sulfides on the carbons) may result in sluggish charge transfer at the interface, leading to limited redox efficiency of the polysulfides.[7,14] Thus, engineering hybrid sulfur hosts from metal sulfides and carbons with strong interaction should be favorable in enabling both high redox efficiency and sulfur utilization in lithium–sulfur batteries.

Very recently, strongly coupled hybrid materials have shown unique advantages as sulfur hosts, derived from the chemical bonding between the components, leading to its high adsorption capacity to the polysulfides as well as the good stability during battery operation.[8,15] As an example, a chemically coupled hybrid material of ferrocene (Fc) and graphene oxide (GO) was fabricated as a sulfur host, achieving capacity decay as low as 0.014% in 550 cycles.[16] The chemical bonding between the Fc and the GO not only provided an excellent distribution of Fc on the GO to enhance the adsorption capacity to the polysulfides, but also provided strong attachment of Fc particles on the GO during long cycles. However, the poor conductivity of Fc particles may hinder the redox efficiency of the polysulfides, resulting in poor rating performance. Therefore, the combination of metal sulfides and carbons with strong chemical coupling could offer favorable electron pathways as well as high adsorption capacity for the redox reaction of the polysulfides. However, such a hybrid material of metal sulfides and carbons as a sulfur host has not been reported.

In this work, we report the fabrication of a hybrid material of nanosized nickel sulfide (NiS) uniformly distributed on 3D carbon hollow spheres (NiS@C-HS) with strong chemical coupling by an in situ thermal reduction and sulfidation approach. The nanosized NiS with uniform distribution maximizes the chemical adsorption capability to polysulfides. Meanwhile, the C-HS can provide sufficient internal void space to accommodate high sulfur loading and large volume expansion, a 3D electron pathway, and a physical barrier to reduce the loss of active material. More importantly, the strong chemical coupling between the nanosized NiS and carbon shell further enhanced charge transfer and redox kinetics of the sulfur electrode. As a result, the hybrid material achieved excellent operation stability with a low capacity decay of 0.013% per cycle and a capacity of 695 mA h g^{-1} after 300 cycles.

2. Results and Discussion

The hybrid NiS@C-HS material was synthesized using a controllable template method (**Figure 1**a). First, highly dispersed and uniform SiO_2 nanospheres with an average diameter of ≈450 nm were synthesized as a hard template (Figure 1b and
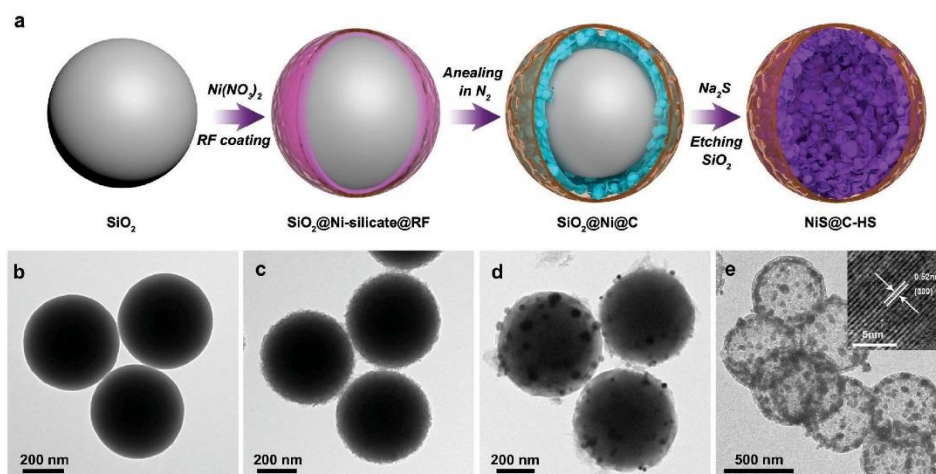

Figure 1. a) Schematic illustration of the fabrication process of NiS@C-HS. TEM images of b) SiO_2, c) SiO_2@Ni-silicate@RF, d) SiO_2@Ni@C, e) NiS@C-HS, and the inset is the HRTEM of NiS.

Figure S1 (Supporting Information)). After reacting with an aqueous solution of nickel nitrate (Figures S2 and S3, Supporting Information) and being coated by resorcinol formaldehyde (RF) resin, SiO_2@Ni-silicate@RF spheres were fabricated with an average diameter of about 530 nm (Figure 1c). Subsequently, Ni nanoparticles were incorporated into the carbon shell after carbonized in N_2 atmosphere, forming SiO_2@Ni@C (Figure 1d). NiS@C-HSs with well-maintained spherical morphology were fabricated by a sulfidation process using sodium sulfide (Na$_2$S; Figure 1e and Figure S4 (Supporting Information)), where Ni particles are in situ transformed to NiS. The clear lattice fringes had an interplanar spacing of 0.52 nm were assigned to the (300) planes of millerite NiS. EDX spectroscopy showed that the carbon content in NiS@C-HS hybrid is over 60 wt% and that the SiO_2 cores are etched by OH^- released from the hydrolysis of sulfide ions (Figure S5, Supporting Information). Herein, the Na$_2$S not only functions as a sulfurizing agent, transforming nickel particles to nanosized NiS, but also grants the as-formed hollow spheres structural integrity by providing a mild alkaline environment to gradually remove the SiO_2 template. To investigate the components and structural advantages of NiS@C-HS, three control samples were prepared. First, a conventional hybrid material of NiS and C-HS (C-HS@NiS) was prepared by coating NiS particles on the surface of C-HS using a solvothermal method. Consequently, the size of NiS is much larger than that of NiS in the NiS@C-HS and the distribution of the NiS is poor (Figure S6a,d, Supporting Information). This is because the formation of NiS on the surface of C-HS proceeds via an uncontrolled process of heterogeneous nucleation. Carbon hollow spheres (C-HS) and NiS hollow spheres (NiS-HS) were applied as another two control samples. The C-HS were fabricated by coating SiO_2 with RF resin, followed by annealing in N_2 and etching SiO_2 with Na$_2$S. The C-HS obtained exhibited a well-maintained hollow structure (Figure S6b,e, Supporting Information). The NiS-HS were fabricated by treating the SiO_2@Ni-silicate with Na$_2$S. Scanning electron microscope (SEM) and transmission electron microscope (TEM) images show that the NiS-HS assembled into nanosheets with hollow spherical structure (Figure S6c,f, Supporting Information).

X-ray diffraction (XRD) spectroscopy revealed that the crystal phase of NiS@C-HS changes during the in situ thermal reduction and sulfidation process. After sintering at 800 °C, Ni-silicate was reduced to nanosized Ni particles (JCPDS No. 650143) by the carbon species (Figure S7, Supporting Information). Then, the Ni metal was transformed into millerite-type NiS (JCPDS No.86-2280) after Na$_2$S treatment (Figure S8, Supporting Information).[17] The XRD patterns of the C-HS@NiS and NiS-HS also demonstrated that the millerite-type NiS is the primary crystalline phase of the products (Figure S8, Supporting Information). The N_2 adsorption isotherm recorded on NiS@C-HS resembles type I and IV isotherm and a H3 hysteresis loop, suggesting an adequate microporous texture compared with the other three samples (Figure S9, Supporting Information). The specific surface area (SSA) of NiS@C-HS were calculated to be 241 m^2 g^{-1}, using the Brunauer–Emmett–Teller method. In contrast, the SSA of C-HS@NiS, C-HS, and NiS-HS were calculated to be 59, 120, and 81 m^2 g^{-1}, respectively. The larger SSA and microporous texture of NiS@C-HS might derive from

the etching of silicate in the carbon shell during treatment with Na$_2$S, in which the silicate acted as molecular separator. The hybrid nature of NiS@C-HS was further confirmed by thermogravimetric analysis (TGA; Figure S10, Supporting Information). The weight loss of 62.8% in NiS@C-HS between 100 and 800 °C was ascribed to the combustion of carbon species, which is consistent with the result of EDX. To make a proper comparison, the carbon content in C-HS@NiS was controlled to be ≈60% by controlling the duration of the solvothermal process. TGA was also used to confirm the absence of SiO_2 in these three samples.

The strong chemical coupling of the hybrid material was studied by carbon K-edge near-edge X-ray absorption fine structure (NEXAFS), which offered local structural information of C in the NiS@C-HS, C-HS@NiS, and C-HS (**Figure 2a**). The peak at 285.3 eV is attributed to the C 1s unoccupied states of C–C π^* in C-HS and C-HS@NiS. Notably, the shift in the corresponding π^* of NiS@C-HS to a higher energy (285.4 eV) implies a different chemical environment of C in NiS@C-HS. This might derive from the chemical bond between C and NiS, resulting in a reduced electron density of C in NiS@C-HS.[18] Further, X-ray photoelectron spectra (XPS) of S 2p in NiS@C-HS and C-HS@NiS were obtained with the assumption of five species (Figure 2b), including a pair of spin–orbit doublets and their shakeup satellite.[19] In comparison to the signal detected at 163.8 eV assigned to C–S bonds in the C-HS@NiS, the increasing signal detected at 163.8 and 165.0 eV (–C=S– bond) in NiS@C-HS implies the C–S chemical bonding in the NiS@C-HS is much stronger that in the C-HS@NiS.[20] Moreover, electrochemical properties of the two materials were also investigated by cyclic voltammetry (CV) in 1 M KOH electrolyte at scan rate of 100 mV s^{-1}. CV curves in Figure 2c show that NiS@C-HS exhibits a peak voltage separation (ΔE_p) of 144 mV, which is smaller than that of the C-HS@NiS (185 mV), indicating greater reversible redox behavior for the NiS@C-HS. This improved reversible redox behavior for NiS@C-HS could be attributed to the strong coupling interaction.[21]

The impregnation of sulfur was carried out using a modified melting-diffusion method. The S/NiS@C-HS composite maintained its original spherical morphology with smooth surfaces after sulfur loading (**Figure 3a**). The EDX spectrum of S/NiS@C-HS shows the presence of sulfur and NiS in the composite, as shown in the inset of Figure 3a. TEM imaging shows that the contrast of the inner space of NiS@C-HS becomes much darker after sulfur loading (Figure 3b). Also, scanning transmission electron microscopy (STEM) and the linear scan analysis of S/NiS@C-HS verifies its hybrid nature and demonstrates that sulfur is homogeneously distributed in the NiS@C-HS host (Figure 3c–f). The S/C-HS@NiS, S/C-HS, and S/NiS-HS composites retained their original spherical morphology, again suggesting the excellent sulfur loading capacity of the hollow structures (Figure S11, Supporting Information). The sulfur content was determined by TGA characterization performed from 20 to 400 °C at a heating rate of 5 min^{-1} under nitrogen atmosphere. TGA suggests that the sulfur content of the four composite samples is ≈72% (Figure S12, Supporting Information).

The rate capabilities of the four composites were evaluated by cycling at various current densities. When cycled at 0.1,
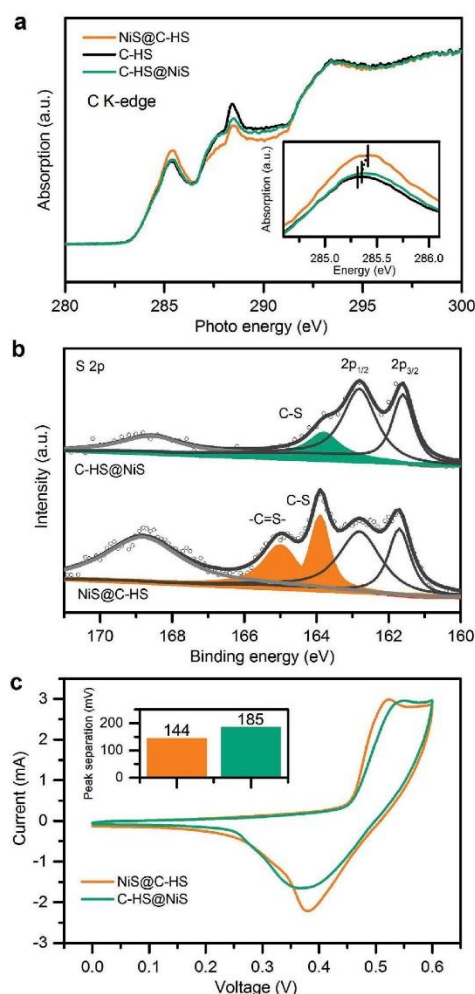
Figure 2. a) Carbon K-edge NEXAFS of NiS@C-HS, C-HS@NiS and C-HS, and the inset is the magnified absorption curve between 285.0 and 286.0 eV. b) XPS S 2p spectra of C-HS@NiS and NiS@C-HS. c) CV curve of redox reaction of NiS@C-HS and C-HS@NiS, and the inset is the peak separation of the CV curves.

0.2, 0.5, 1, and 2 C, the discharge capacities of S/NiS@C-HS were about 1196, 997, 880, 798, and 674 mA h g^{-1}, respectively (**Figure 4**a,b). When the current density was abruptly switched back to 0.2 C, a high discharge capacity of 1013 mA h g^{-1} was still maintained. S/NiS@C-HS exhibited the highest capacity among the four composites at the same discharge rate, indicating good conductivity, and stability of the S/NiS@C-HS

during various rates. The S/C-HS@NiS electrode showed an abrupt capacity drop (612–224 mA h g^{-1}) when the current density was switched from 1 to 2 C because of the relative poor conductivity and inadequate adsorption to polysulfide. Although the S/C-HS also shows good cycling stability, the relative low capacity is caused by a lack of chemical adsorption to polysulfides throughout the whole cycling. The S/NiS-HS electrode shows the worst rate capability among all of the four composites, suffering from its poor conductivity which derives from the lack of a conductive carbon shell. Also, the semicircular diameter in the electrochemical impedance spectroscopy (EIS) of S/NiS-HS and S/C-HS@NiS composites is much larger than that of S/NiS@C-HS and S/C-HS (Figure 4c). Specifically, the semicircular diameters of the S/C-HS and S/NiS@C-HS are almost the same, suggesting that the conductivities of the two electrodes are similar. This implies that the incorporation of NiS into the C-HS has no significant effect on the conductivity of C-HS. The cycling performance of the four cathodes at 0.2 C (1 C = 1675 mA g^{-1}) was evaluated (Figure 4d). The S/NiS@C-HS delivered an initial capacity of 1002 mA h g^{-1} and a capacity retention of 72% (718 mA h g^{-1} after 200 cycles), indicating good conductivity and a high adsorption capacity to polysulfides. In contrast, S/C-HS@NiS and S/C-HS showed initial capacities of 851 and 932 mA h g^{-1} with a capacity retention of 60% and 51%, respectively, indicating inadequate adsorption to polysulfides. Without the high conductivity offered by nanocarbon, the S/NiS-HS showed the lowest cycling performance with a final capacity of 509 mA h g^{-1} after 107 cycles.

The long-term cycling stability of the S/NiS@C-HS (with a high sulfur loading of 2.3 mg cm^{-2}) was further investigated at a higher rate of 0.5 C (Figure 4e). After two activation cycles at 0.1 C, the reversible capacity of S/NiS@C-HS was 723 mA h g^{-1}. After 300 cycles at 0.5 C, S/NiS@C-HS was able to retain a capacity of 695 mA h g^{-1}. The corresponding capacity retention was ≈96%, representing a minimal capacity decay of ≈0.013% per cycle. Additionally, the corresponding CE to S/NiS@C-HS stabilized around 97% after 400 cycles. This excellent cycling stability of S/NiS@C-HS is superior to most metal oxide, metal sulfide, or hybrid electrodes reported previously (Table S1, Supporting Information).

Adsorption capability plays an important role in battery performance for a sulfur host. For the purpose of comparing adsorption capabilities, the four hosts were treated with a 0.005 mol L^{-1} polysulfide solution (Li$_2$S$_x$, x ≈ 6) for 5 h. As illustrated in **Figure 5**a, adsorption capability of the hosts follows: NiS@C-HS ≥ NiS-HS > C-HS@NiS > C-HS, which agrees well with their electrochemical properties presented above. From their Raman spectra, four strong peaks at 252, 290, 355, and 376 cm^{-1} can be ascribed to the vibration modes of E(2), A$_1$(2), E(1), and A$_1$(1), respectively, of millerite NiS in the NiS@C-HS (Figure 5b).[22] A new broad peak at 230 cm^{-1} was observed in the Li$_2$S$_x$-treated NiS@C-HS (NiS@C-HS-Li$_2$S$_x$), likely the characteristic absorbance of an S—S bonds in the polysulfide species.[23] Noticeably, a slight redshift of the four main peaks provides strong evidence for the chemical bonding between NiS and the lithium polysulfides. Accordingly, XPS studies of the NiS@C-HS and NiS@C-HS-Li$_2$S$_x$ were performed to further probe the underlying adsorption principles. The Ni 2p in NiS@C-HS and NiS@C-HS-Li$_2$S$_x$ were recorded with the

64

**ADVANCED
SCIENCE NEWS**
www.advancedsciencenews.com

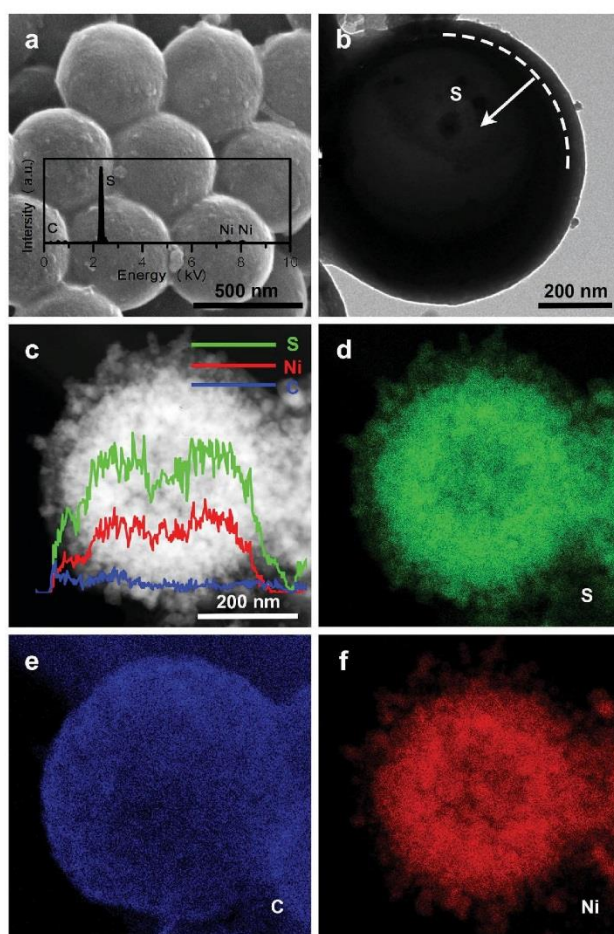**ADVANCED
FUNCTIONAL
MATERIALS**
www.afm-journal.de

Figure 3. a) SEM image, with inset of the EDX spectrum and b) TEM image of S/NiS@C-HS. c–f) STEM image, linear scan and corresponding EDX spectrum elemental map of the S/NiS@C-HS.

which is desired for high-performance lithium–sulfur batteries.

Strong chemical coupling in NiS@C-HS derived from the in situ sulfidation of Ni particles into nanosized NiS is supported by spectroscopic analyses (Figure 2), resulting in significantly improved conductivity and charge transfer capability. Accordingly, NiS@C-HS displays a longer second-discharge plateau at ≈2.1 V (the deep redox reaction from long-chain lithium polysulfides into insoluble products Li_2S_2/Li_2S) compared with the S/C-HS@NiS (Figure S13a,b, Supporting Information). This suggests that the redox reaction kinetics in the S/NiS@C-HS is more favorable than that in the S/C-HS@NiS, implying better charge transfer in the S/NiS@C-HS electrode compared with the S/C-HS@NiS electrode.[26] It was also confirmed that no obvious redox reaction of NiS in NiS@C-HS occurred and the NiS@C-HS contributed less than 20 mA h g^{-1} to the capacity (Figure S14, Supporting Information). Also, in comparison to that of S/NiS-HS, S/NiS@C-HS shows a narrow voltage gap between discharge and charge voltages during long-term cycling, indicating more sustained adsorption to the polysulfides. This may result from the strong C−S chemical coupling, enhancing the adhesion between the nanosized NiS and C-HS during cycling, promoting the structural stability of the host material for long cycling processes, and consequently reducing the loss of lithium polysulfides and undesirable interface in the electrode.[27] In addition, S/NiS@C-HS had a similar EIS semicircular diameter to S/C-HS, but significantly smaller than that of C-HS@NiS (Figure 4c). This implies a highly improved conductivity and charge transfer capability to the conventionally hybridized C-HS@NiS material. Accordingly, NiS@C-HS utilized as a sulfur host largely exceeds the capacities of the conventional C-HS@NiS material at high rate (Figure 4b).

Moreover, the C-HS in the NiS@C-HS serves as a 3D electron pathway as well as a physical confinement to the polysulfides, which is supported by the longer second-discharge plateau and the narrow voltage gap between discharge and charge voltages of the S/NiS@C-HS in comparison to that of the S/NiS-HS (Figure S13a,c,d, Supporting Information). This suggests better conductivity and more effective adsorption to the polysulfides in the electrode which might result from the physical confinement provided by the C-HS.[28] Schematic illustrations of Li–S batteries show the effects of the unique 3D hybrid sulfur hosts on electrochemical performance (**Figure 6**). NiS@C-HS is a superior sulfur host structure which affords advantages of both high conductivity and effective adsorption to polysulfides compared to conventional hybrid sulfur hosts.

assumption of six species (Figure 5c), including two pairs of spin–orbit doublets and their two shakeup satellites.[20,24] In comparison to the XPS peaks centered at 853.2 and 870.5 eV, assigned to Ni^{2+} 2p$_{3/2}$ and Ni^{2+} 2p$_{1/2}$ of NiS@C-HS, the shift in the corresponding peaks of NiS@C-HS-Li$_2$S$_x$ to 853.7 and 871.0 eV implies the transfer of coupled electrons from S$_x^{2-}$ to Ni^{2+}. The Raman spectra together with the XPS studies (Figure 5b,c) indicate strong chemical adsorption of Ni^{2+} in NiS to S$_x^{2-}$ in Li$_2$S$_x$, which is illustrated in Figure 5d.[25] Therefore, adsorption experiments, Raman, and XPS demonstrate the high adsorption capability of nanosized NiS in the NiS@C-HS,

**ADVANCED
SCIENCE NEWS**
www.advancedsciencenews.com

**ADVANCED
FUNCTIONAL
MATERIALS**
www.afm-journal.de

Figure 4. a) Discharge/charge curves of S/NiS@C-HS at different rates. b) Rate capabilities, c) Nyquist plots, and d) cycling performances and CE of the four sulfur cathodes at 0.2 C. e) Cycling performances and CE of the S/NiS@C-HS at 0.5 C.

3. Conclusion

In summary, we report the fabrication of a 3D hybrid material, NiS@C-HS, to promote the loading, utilization, and retention of sulfur. The resultant 3D hybrid sulfur host was employed as an electrode which achieved a capacity of 695 mA h g^{-1} after 300 cycles at 0.5 C, with a low capacity decay of 0.013% per cycle. The three main advantages of NiS@C-HS are high adsorption capability toward polysulfides, strong chemical coupling for charge transfer and operation stability, and a 3D hollow structure for favorable electron pathway, all of which likely contribute to its high performance. This new NiS@C-HS hybrid system can potentially be applied in other energy storage and conversion systems. In addition, the new in situ thermal reduction and sulfidation method is expected to stimulate the development of more 3D hybrid materials for applications in other energy storage devices, e.g., sodium-ion batteries.

4. Experimental Section

Preparation of NiS@C-HS and Other Control Samples: SiO$_2$ nanospheres were prepared by a previously reported method.[29] Ni-silicate was first coated on SiO$_2$ nanospheres via a method that has been reported.[17] Typically, 0.2 g of SiO$_2$ nanospheres were dispersed in 40 mL of deionized (DI) water in a capped bottle, followed by the addition of 1 g of urea and 0.12 g of Ni(NO$_3$)$_2$·6H$_2$O. The capped bottle was stored in an oven at 105 °C. After reaction for 12 h, SiO$_2$@ Ni-silicate nanospheres were collected by centrifugation and washed several times with ethanol and DI water. The carbon precursor layer was coated on SiO$_2$@Ni-silicate by a method reported.[30] Typically, 0.2 g of SiO$_2$@Ni-silicate nanospheres was dispersed into a solution containing 150 mL ethanol, 45 mL of DI water, and 7.5 g Hexadecyl trimethyl ammonium Bromide (CTAB), followed by the addition of 0.525 g of resorcinol and 0.6 mL of ammonium hydroxide (28 wt%), and stirring for 30 min. Then, 0.75 mL of formalin solution was added to the dispersion under stirring. After 6 h, the stirring was stopped, and the mixture was aged at room temperature. SiO$_2$@Ni-silicate@ RF was collected by centrifugation and washed several times with DI

66

ADVANCED
SCIENCE NEWS
www.advancedsciencenews.com

ADVANCED
FUNCTIONAL
MATERIALS
www.afm-journal.de
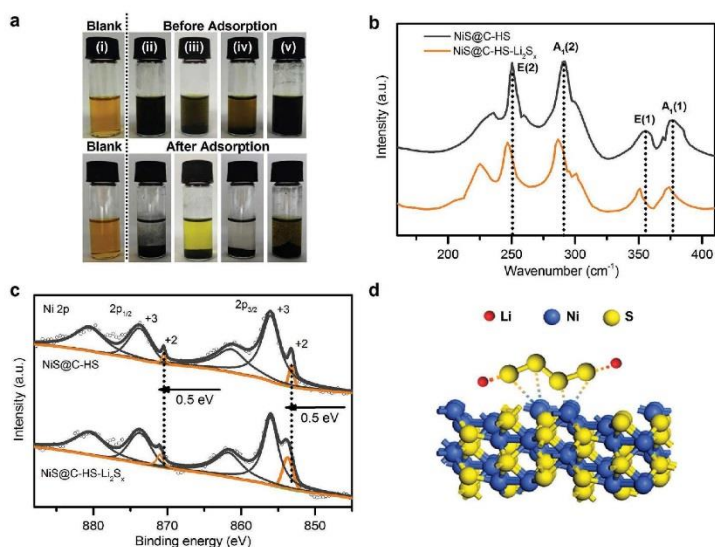
Figure 5. a) Optical images of (i) blank polysulfide solution, (ii) NiS@C-HS, (iii) C-HS@NiS, (iv) NiS-HS, and (v) C-HS before and after treatment of the polysulfide solution. b) Raman spectra and c) XPS spectra of Ni 2p regions for the NiS@C-HS and NiS@C-HS-Li$_2$S$_x$. d) Schematic illustration of the Li$_2$S$_4$ binding configuration with NiS.

water and ethanol, and then dried at 70 °C for 12 h. The as-prepared SiO$_2$@Ni-silicate@RF nanospheres were carbonized at 800 °C for 6 h under nitrogen atmosphere with a heating rate of 1 °C min^{-1}. Finally, 0.1 g of the synthesized SiO$_2$@Ni@C nanospheres was dispersed in 40 mL of DI water in a Teflon container, followed by addition of 0.1 g

of Na$_2$S. After thorough mixing, the mixture was heated at 160 °C for 24 h. After cooling down naturally, the black precipitate was collected by several rinse-centrifugation cycles before drying at 60 °C in vacuum for characterization. The NiS-HS control samples were synthesized using a hydrothermal reaction mentioned above. The resultant
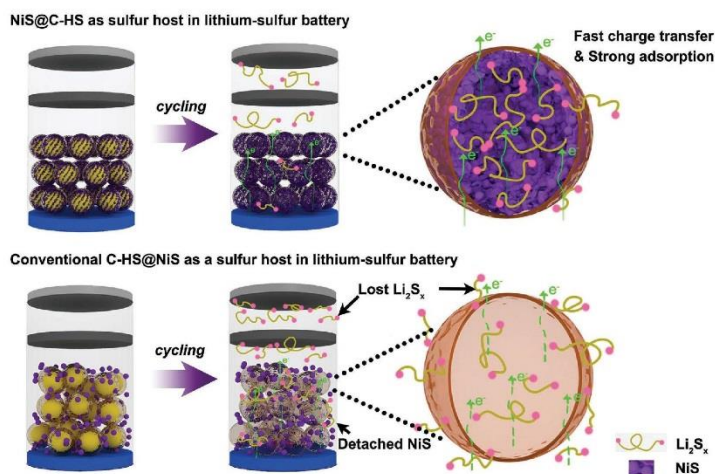
Figure 6. Schematic illustration of NiS@C-HS and conventional C-HS@NiS as sulfur hosts for improving the performance of lithium–sulfur batteries.

NiS-HS were washed several times with DI water and ethanol by centrifugation, and dried at 70 °C for 12 h. To prepare C-HS, 0.2 g SiO$_2$ nanospheres was dispersed into a solution containing 150 mL ethanol, 45 mL of DI water, and 7.5 g CTAB. This was followed by the addition of 0.525 g resorcinol and 0.6 mL of ammonium hydroxide (28 wt%), and stirring for 30 min. Then, 0.75 mL of formalin solution was added to the dispersion under stirring. After 6 h, the stirring was stopped, and the mixture was aged at room temperature. SiO$_2$@ RF were collected by centrifugation and washed several times with DI water and ethanol, and dried at 70 °C for 12 h. The HCS sample was obtained by annealing SiO$_2$@RF at 800 °C for 6 h under nitrogen atmosphere with a heating rate of 1 °C min^{-1} and then reacting with Na$_2$S using a hydrothermal method.

Preparation of S/NiS@C-HS and Other Control Composites: A mixture of NiS@C-HS and sulfur powder (1:3 by weight) was sealed in a glass vessel under argon protection, and heated at 155 °C for 30 h in a quartz tube furnace for compositing sulfur with NiS@C-HS. After cooling down, S/NiS@C-HS was obtained. The preparation process of S/C-HS@NiS, S/C-HS, and S/NiS-HS is the same to the method mentioned above.

Characterization: The morphologies and structures of the samples were characterized by SEM (FEI Quanta 450), TEM (FEI Tecnai G2 Spirit), high resolution TEM (HRTEM, Talos F200x), STEM (Talos F200x), and EDX (Talos F200x). XRD data were collected on a Rigaku MiniFlex 600 X-Ray Diffractometer. Sulfur or carbon contents of the samples were determined by TGA (METTLER TOLEDO TGA/DSC 2) under nitrogen or air flow with a temperature ramp of 20 or 10 °C min^{-1}, respectively. Raman spectrums were collected on HORIBA LabRAM HR Evolution with an excitation wavelength of 532 nm.

Electrochemical Measurements: CV studies of NiS@C-HS and C-HS@ NiS were carried out in a three-electrode system in 1 M KOH aqueous electrolyte at room temperature. The as-prepared host materials, a platinum wire electrode and a silver chloride electrode (Ag/AgCl) were used as working electrode, counter electrode, and reference electrode, respectively. The working electrode was prepared by mixing a sample of the active material with Nafion as the binder in water and ethanol to produce a homogeneous paste. The resultant mixture was then coated onto a Ni foam substrate. The foam was dried at 80 °C in air for 12 h to remove remaining solvent. The electrochemical performances of the as-prepared electrodes were tested using CV on an electrochemical workstation (CHI 660D, Shanghai CH Instrument Company, China). The measurements were carried out in 1 M KOH aqueous electrolyte at room temperature. CV tests were done between 0 and 0.6 V (vs Ag/AgCl) at a scan rate of 100 mV s^{-1}. For battery performance measurements, a slurry mixture containing 70 wt% of the active material, 20 wt% of conductive carbon, 5 wt% of carboxymethylcellulose sodium, and 5 wt% Styrene Butadiene Rubber was cast on aluminum foil and dried at 70 °C overnight to fabricate the electrode film. The 2032-type coin cells were assembled using Celgard 2400 membranes as the separator and Li metal as the anode. The area of the sulfur electrode was accurately defined as 1.13 cm^2. The electrolyte was prepared by dissolving 1.0 mol L^{-1} lithium bis(trifluoromethanesulfonyl) imide in a mixture of 1,3-dioxolane (DOL) and dimethoxymethane (1:1 v/v) with the addition of 0.2 mol L^{-1} LiNO$_3$. The volume of electrolyte injected in coin cells was controlled to about 20 μL per 1 mg of sulfur. The areal sulfur loading in cathode for rating performance is about 1.0 mg cm^{-2}. The galvanostatic charge/discharge measurements were performed using a NEWARE battery tester. The capacities were calculated based on the mass of sulfur. The electrochemical impedance measurements were carried out at 5 mV AC oscillation amplitude over the frequency range of 100 kHz to 100 MHz.

Polysulfide Adsorption Study: The 0.1 M polysulfide solution (Li$_2$S$_x$, $x \approx 6$) was prepared by dissolving and mixing stoichiometric amounts of Li$_2$S and sulfur in DOL at room temperature for 10 h. Test solutions were prepared by mixing 100 μL of the 0.1 M polysulfide solution, 1 mL of DOL and 1 mL of dimethyl ether (DME). 20 mg of NiS@C-HS, C-HS@NiS, NiS-HS, and C-HS were added separately to each solution. All procedures were completed in an Ar-filled glove box.

Supporting Information

Supporting Information is available from the Wiley Online Library or from the author.

Acknowledgements

Conflict of Interest

The authors declare no conflict of interest.

Keywords

[1] a) Z. W. Seh, Y. Sun, Q. Zhang, Y. Cui, *Chem. Soc. Rev.* **2016**, *45*, 5605; b) Y. Yang, G. Zheng, Y. Cui, *Chem. Soc. Rev.* **2013**, *42*, 3018.

[2] a) G. Zhou, Y. Zhao, A. Manthiram, *Adv. Energy Mater.* **2015**, *5*, 1402263; b) J. Zhang, H. Hu, Z. Li, X. W. D. Lou, *Angew. Chem. Int. Ed.* **2016**, *55*, 3982; c) X. Song, S. Wang, Y. Bao, G. Liu, W. Sun, L.-X. Ding, H. Liu, H. Wang, *J. Mater. Chem. A* **2017**, *5*, 6832; d) D. Su, M. Cortie, G. Wang, *Adv. Energy Mater.* **2016**, *7*, 1602014.

[3] H. Yao, K. Yan, W. Li, G. Zheng, D. Kong, Z. W. Seh, V. K. Narasimhan, Z. Liang, Y. Cui, *Energy Environ. Sci.* **2014**, *7*, 3381.

[4] M. Cuisinier, C. Hart, M. Balasubramanian, A. Garsuch, L. F. Nazar, *Adv. Energy Mater.* **2015**, *5*, 1401801.

[5] a) S. Xin, L. Gu, N.-H. Zhao, Y.-X. Yin, L.-J. Zhou, Y.-G. Guo, L.-J. Wan, *J. Am. Chem. Soc.* **2012**, *134*, 18510; b) H. J. Peng, Q. Zhang, *Angew. Chem. Int. Ed.* **2015**, *54*, 11018; c) C. J. Hart, M. Cuisinier, X. Liang, D. Kundu, A. Garsuch, L. F. Nazar, *Chem. Commun.* **2015**, *51*, 2308.

[6] W. Kong, L. Yan, Y. Luo, D. Wang, K. Jiang, Q. Li, S. Fan, J. Wang, *Adv. Funct. Mater.* **2017**, *27*, 1606663.

[7] Q. Pang, D. Kundu, L. F. Nazar, *Mater. Horiz.* **2016**, *3*, 130.

[8] W. Bao, D. Su, W. Zhang, X. Guo, G. Wang, *Adv. Funct. Mater.* **2016**, *26*, 8746.

[9] H. J. Peng, Z. W. Zhang, J. Q. Huang, G. Zhang, J. Xie, W. T. Xu, J. L. Shi, X. Chen, X. B. Cheng, Q. Zhang, *Adv. Mater.* **2016**, *28*, 9551.

[10] a) X. Y. Yu, L. Yu, X. W. D. Lou, *Adv. Energy Mater.* **2016**, *6*, 1501333; b) T. Ling, S. A. Kulinich, Z. L. Zhu, S. Z. Qiao, X. W. Du, *Adv. Funct. Mater.* **2014**, *24*, 707; c) X. L. Zheng, J. P. Song, T. Ling, Z. P. Hu, P. F. Yin, K. Davey, X. W. Du, S. Z. Qiao, *Adv. Mater.* **2016**, *28*, 4935.

[11] Z. Liu, X. Zheng, S. Luo, S. Xu, J. Ding, *J. Mater. Chem. A* **2016**, *4*, 13395.

[12] Z. Yuan, H.-J. Peng, T.-Z. Hou, J.-Q. Huang, C.-M. Chen, D.-W. Wang, X.-B. Cheng, F. Wei, Q. Zhang, *Nano Lett.* **2016**, *16*, 519.

[13] T. Lei, W. Chen, J. Huang, C. Yan, H. Sun, C. Wang, W. Zhang, Y. Li, J. Xiong, *Adv. Energy Mater.* **2016**, *7*, 1601843.

[14] a) S. S. Zhang, D. T. Tran, *J. Mater. Chem. A* **2016**, *4*, 4371; b) H. Wang, Q. Zhang, H. Yao, Z. Liang, H.-W. Lee, P.-C. Hsu, G. Zheng, Y. Cui, *Nano Lett.* **2014**, *14*, 7138; c) Z. W. Seh, J. H. Yu, W. Li, P.-C. Hsu, H. Wang, Y. Sun, H. Yao, Q. Zhang, Y. Cui, *Nat. Commun.* **2014**, *5*, 5017.

[15] H. Wang, H. Dai, *Chem. Soc. Rev.* **2013**, *42*, 3088.

[16] Y. Mi, W. Liu, K. R. Yang, J. Jiang, Q. Fan, Z. Weng, Y. Zhong, Z. Wu, G. W. Brudvig, V. S. Batista, *Angew. Chem.* **2016**, *128*, 15038.

[17] T. Zhu, Z. Wang, S. Ding, J. S. Chen, X. W. D. Lou, *RSC Adv.* **2011**, *1*, 397.

[18] a) Y. Chen, J. Wang, H. Liu, M. N. Banis, R. Li, X. Sun, T.-K. Sham, S. Ye, S. Knights, *J. Phys. Chem. C* **2011**, *115*, 3769; b) J. Zhong, H. Zhang, X. Sun, S. T. Lee, *Adv. Mater.* **2014**, *26*, 7786.

[19] a) Q. Pang, D. Kundu, M. Cuisinier, L. Nazar, *Nat. Commun.* **2014**, *5*, 4759; b) Q. Pang, J. Tang, H. Huang, X. Liang, C. Hart, K. C. Tam, L. F. Nazar, *Adv. Mater.* **2015**, *27*, 6021.

[20] M.-S. Park, J.-S. Yu, K. J. Kim, G. Jeong, J.-H. Kim, Y.-N. Jo, U. Hwang, S. Kang, T. Woo, Y.-J. Kim, *Phys. Chem. Chem. Phys.* **2012**, *14*, 6796.

[21] a) C. Guo, F. Hu, C. M. Li, P. K. Shen, *Biosens. Bioelectron.* **2008**, *24*, 819; b) Z. Wang, C. Nan, D. Wang, Y. Li, *RSC Adv.* **2014**, *4*, 47513.

[22] a) Y. Li, H. Wang, H. Zhang, P. Liu, Y. Wang, W. Fang, H. Yang, Y. Li, H. Zhao, *Chem. Commun.* **2014**, *50*, 5569; b) J. Feng, Q. Wang, *J. Am. Ceram. Soc.* **2009**, *92*, 235; c) F. Guillaume, S. Huang, K. D. Harris, M. Couzi, D. Talaga, *J. Raman Spectrosc.* **2008**, *39*, 1419.

[23] a) J.-T. Yeon, J.-Y. Jang, J.-G. Han, J. Cho, K. T. Lee, N.-S. Choi, *J. Electrochem. Soc.* **2012**, *159*, A1308; b) M. Hagen, P. Schiffels, M. Hammer, S. Dörfler, J. Tübke, M. Hoffmann, H. Althues, S. Kaskel, *J. Electrochem. Soc.* **2013**, *160*, A1205.

[24] I. Kartio, C. Basilio, R.-H. Yoon, *Langmuir* **1998**, *14*, 5274.

[25] X. Liang, A. Garsuch, L. F. Nazar, *Angew. Chem., Int. Ed.* **2015**, *54*, 3907.

[26] a) Z. Li, J. Zhang, B. Guan, D. Wang, L.-M. Liu, *Nat. Commun.* **2016**, *7*, 13065; b) T.-G. Jeong, D. S. Choi, H. Song, J. Choi, S.-A. Park, S. H. Oh, H. Kim, Y. Jung, Y.-T. Kim, *ACS Energy Lett.* **2017**, *2*, 327.

[27] Z. Deng, Z. Zhang, Y. Lai, J. Liu, Y. Li, J. Li, *Solid State Ionics* **2013**, *238*, 44.

[28] a) N. Jayaprakash, J. Shen, S. S. Moganty, A. Corona, L. A. Archer, *Angew. Chem.* **2011**, *123*, 6026; b) C. Zhang, H. B. Wu, C. Yuan, Z. Guo, X. W. D. Lou, *Angew. Chem.* **2012**, *124*, 9730.

[29] a) J. Liang, Y. Zheng, J. Chen, J. Liu, D. Hulicova-Jurcakova, M. Jaroniec, S. Z. Qiao, *Angew. Chem.* **2012**, *124*, 3958; b) F. Xie, L. Zhang, D. Su, M. Jaroniec, S. Z. Qiao, *Adv. Mater.* **2017**, *29*, 1700989.

[30] J. Liu, S. Z. Qiao, H. Liu, J. Chen, A. Orpe, D. Zhao, G. Q. M. Lu, *Angew. Chem. Int. Ed.* **2011**, *50*, 5947.

**ADVANCED
FUNCTIONAL
MATERIALS**

Supporting Information

A 3D Hybrid of Chemically Coupled Nickel Sulfide and Hollow Carbon Spheres for High Performance Lithium–Sulfur Batteries

Chao Ye, Lei Zhang, Chunxian Guo, Dongdong Li, Anthony Vasileff, Haihui Wang,* and Shi-Zhang Qiao*

Supporting Information

A Three-Dimensional Hybrid of Chemically Coupled Nickel Sulfide and Hollow Carbon Spheres for High Performance Lithium-Sulfur Batteries

Chao Ye, [a] *Lei Zhang,* [a] *Chunxian Guo,* [a] *Dongdong Li,* [b] *Anthony Vasileff,* [a] *Haihui Wang,* *[b] *and Shi-Zhang Qiao* *[a]

C. Ye, Dr. L. Zhang, Dr. C. X. Guo, A. Vasileff, Prof. S.-Z. Qiao
School of Chemical Engineering
The University of Adelaide
Adelaide, SA 5005, Australia
E-mail: s.qiao@adelaide.edu.au

D. D. Li, Prof. H. H. Wang
School of Chemistry and Chemical Engineering
South China University of Technology
Guangzhou 510640, China
E-mail: hhwang@scut.edu.cn
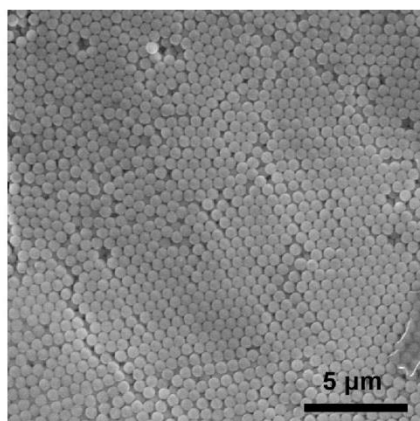
Figure S1. SEM image of SiO_2.
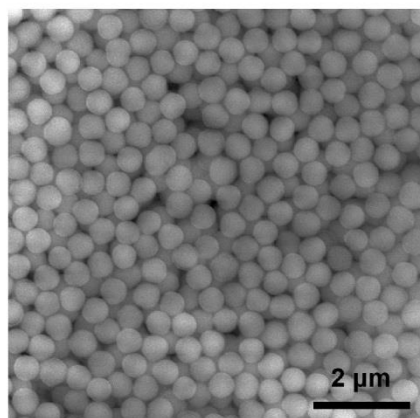
Figure S2. SEM image of $SiO_2@Ni$-silicate.
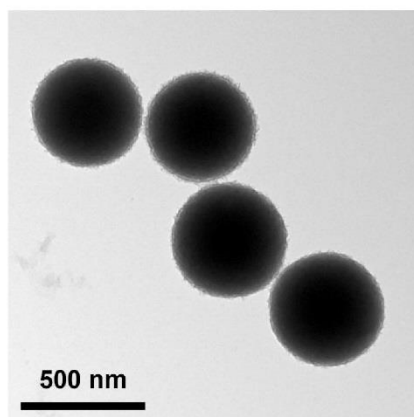
Figure S3. TEM image of SiO$_2$@Ni-silicate.
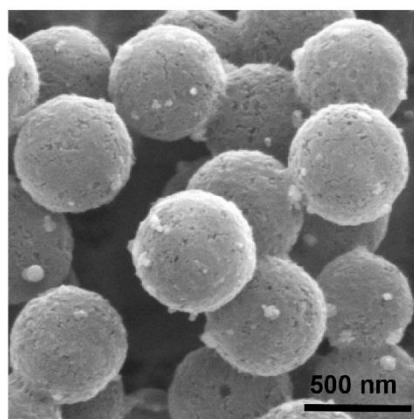
Figure S4. SEM image of NiS@C-HS.
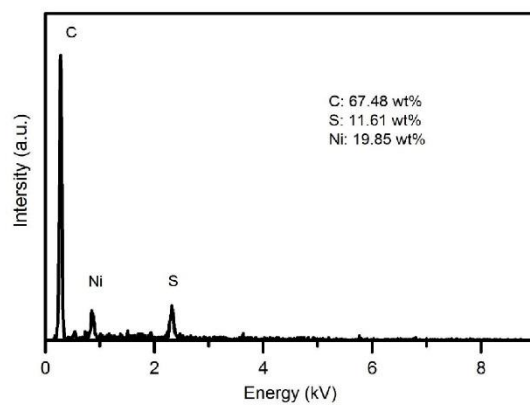
Figure S5. EDX spectrum of NiS@C-HS.
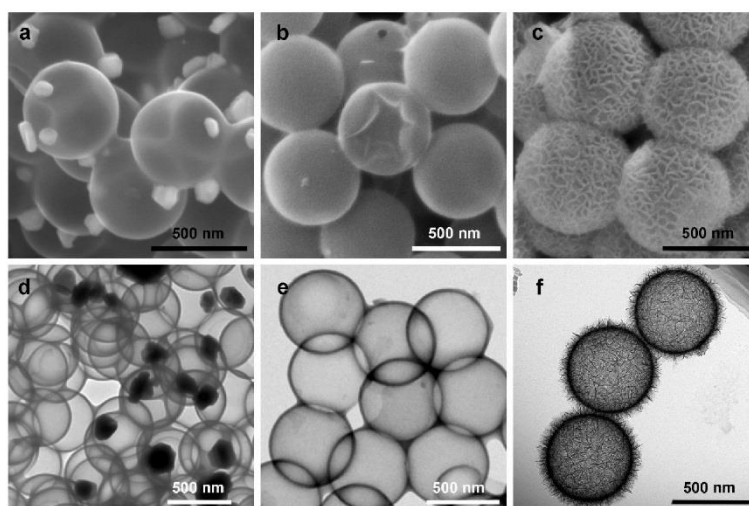
Figure S6. SEM images of a) C-HS@NiS, b) C-HS, and c) NiS-HS, and TEM images of d) C-HS@NiS, e) C-HS, and f) NiS-HS.

74
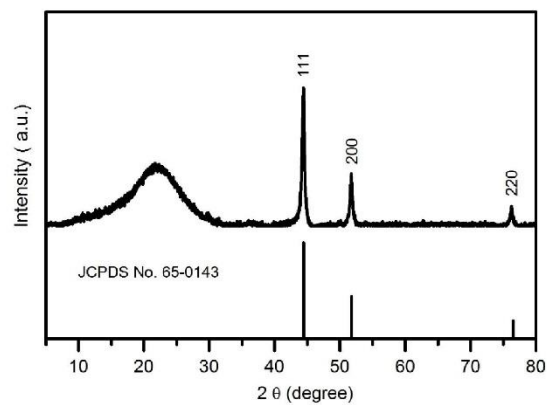
Figure S7. XRD pattern of SiO$_2$@Ni@C.
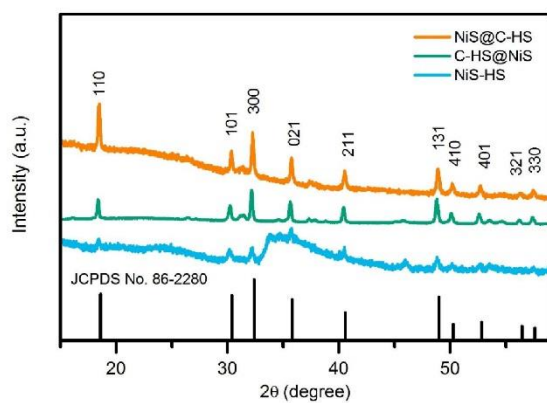
Figure S8. XRD pattern of NiS@C-HS, C-HS@NiS, and NiS-HS.
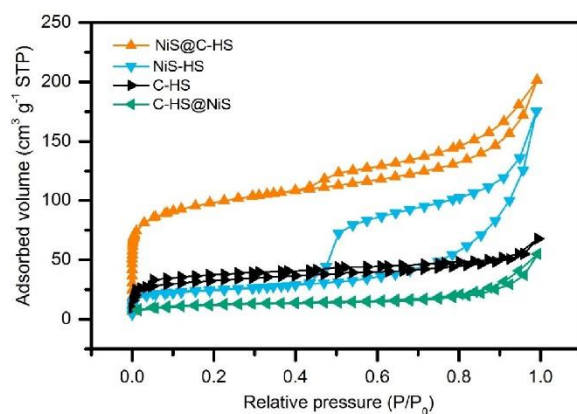
Figure S9. N_2 sorption isotherm of the NiS@C-HS, C-HS@NiS, C-HS and NiS-HS.
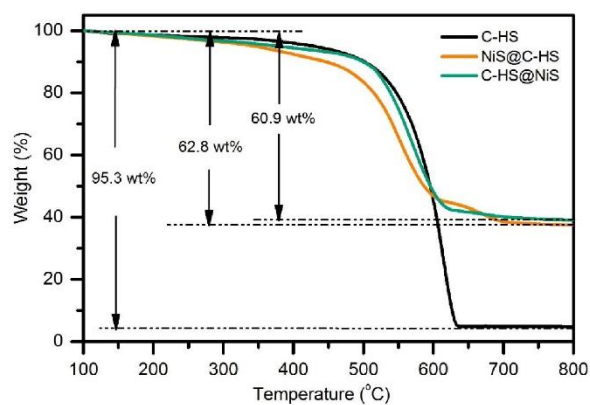
Figure S10. TGA curve of C-HS, NiS@C-HS and C-HS@NiS in air with a heating rate of 20°C min⁻¹.
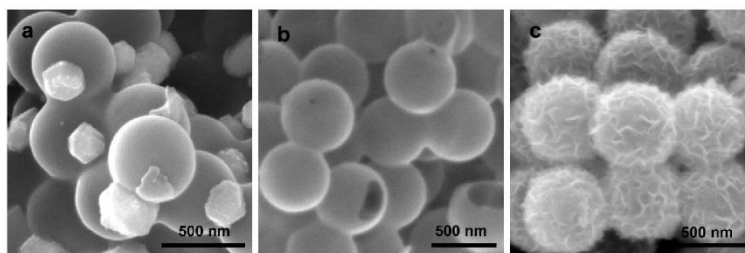
Figure S11. SEM images of a) S/C-HS@NiS, b) S/C-HS, and c) S/NiS-HS.
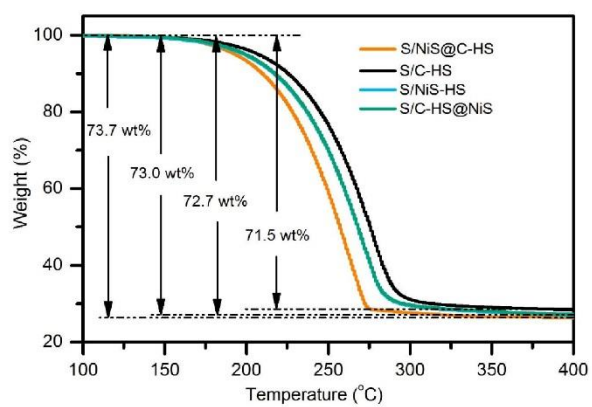
Figure S12. TGA curve of S/NiS@C-HS, S/C-HS@NiS, S/C-HS and S/NiS-HS in nitrogen with a heating rate of 10°C min⁻¹.
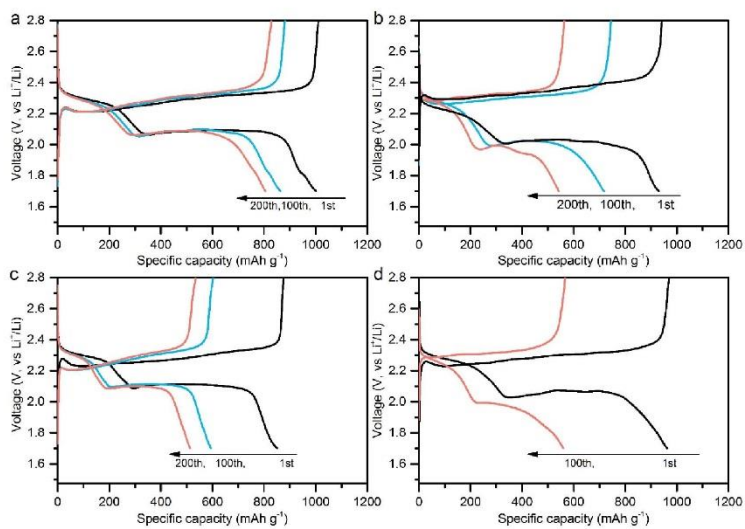
Figure S13. Discharge/charge curves during cycling at 0.2 C of a) S/NiS@C-HS, b) S/C-HS@NiS, c) S/C-HS, and d) S/NiS-HS.
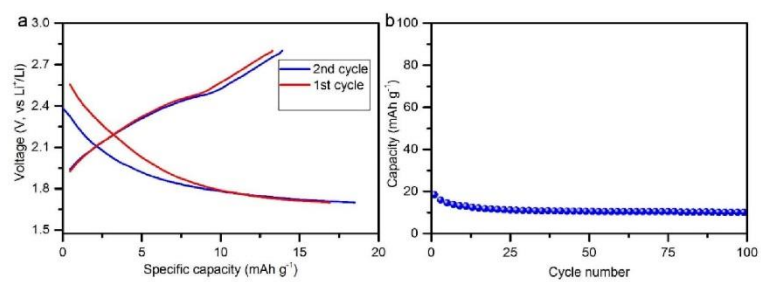
Figure S14. (a) Discharge-charge curves and (b) cycling performance of the NiS@C-HS at a current density of 200 mA g^{-1} in the voltage of 1.7V-2.8V.

Table S1. The performance comparison of this work with some other similar composites.

Sample	S Content	Areal mass loading of S (mg cm^{-2})	Rate	Cycles	Capacity Decay (cycle^{-1})	Capacity (mAh g^{-1})	Ref.
S/NiS@C-HS	73.7%	2.3	0.5C	300	0.013%	695	This work
SiO$_2$ as an additive	70%	≈0.72	0.2	40	≈0.85%	≈647	Ref. S1
S-MnO$_2$ yolk-shell	80%	≈1.5	2C	800	0.048%	480	Ref. S2
S/Hollow carbon fiber-TiO$_2$	67.5%	1.6	0.5C	200	0.188%	650	Ref. S3
S/TiO$_2$-array	45%	0.86	0.2C	200	0.095%	890	Ref. S4
Graphene/TiO$_2$ as interlayer	82%	1.2	0.5C	250	0.101%	600	Ref. S5
S/Ti$_4$O$_7$	64.2%	N/A	0.5C	250	0.012%	604	Ref. S6
S- TiO$_2$ yolk-shell	71%	0.4-0.6	0.2C	1000	0.033%	690	Ref. S7
S/MnO$_2$@hollow carbon fiber	71%	3.5-3.9	0.5C	300	≈0.093%	662	Ref. S8
FeS$_2$ as an additive	62%	2	0.15C	200	0.190%	≈700	Ref. S9
S/Graphene-CoS$_2$	75%	0.4	0.2C	2000	0.034%	554	Ref. S10
S/Co$_9$O$_8$	75%	1.5	0.5C	1500	0.045%	289	Ref. S11
	75%	4.5	0.05	150	≈0.318%	≈500	
S/SnS$_2$-porous carbon	78%	1.5	0.5C	300	0.073%	750	Ref. S12

[1] X. Ji, S. Evers, R. Black, L. F. Nazar, *Nat. Commun.* **2011**, 2, 325.

[2] X. Liang, L. F. Nazar, *ACS nano* **2016**, 10, 4192.

[3] Z. Zhang, Q. Li, S. Jiang, K. Zhang, Y. Lai, J. Li, *Chem. Eur. J.* **2015**, 21, 1343.

[4] Z. Liang, G. Zheng, W. Li, Z. W. Seh, H. Yao, K. Yan, D. Kong, Y. Cui, *ACS nano* **2014**, 8, 5249.

[5] Z. Xiao, Z. Yang, L. Wang, H. Nie, M. e. Zhong, Q. Lai, X. Xu, L. Zhang, S. Huang, *Adv. Mater.* **2015**, 27, 2891.

[6] X. Tao, J. Wang, Z. Ying, Q. Cai, G. Zheng, Y. Gan, H. Huang, Y. Xia, C. Liang, W. Zhang, *Nano Lett.* **2014**, 14, 5288.

[7] Z. W. Seh, W. Li, J. J. Cha, G. Zheng, Y. Yang, M. T. McDowell, P.-C. Hsu, Y. Cui, *Nat. Commun.* **2013**, 4, 1331.

[8] Z. Li, J. Zhang, X. W. D. Lou, *Angew. Chem. Int. Ed.* **2015**, 54, 12886.

[9] S. S. Zhang, D. T. Tran, *J. Mater. Chem. A* **2016**, 4, 4371.

[10] Z. Yuan, H.-J. Peng, T.-Z. Hou, J.-Q. Huang, C.-M. Chen, D.-W. Wang, X.-B. Cheng, F. Wei, Q. Zhang, *Nano Lett.* **2016**, 16, 519.

[11] Q. Pang, D. Kundu, L. F. Nazar, *Mater. Horiz.* **2016**, 3, 130.

[12] X. Li, Y. Lu, Z. Hou, W. Zhang, Y. Zhu, Y. Qian, J. Liang, Y. Qian, *ACS Appl. Mater. Interfaces* **2016**, 8, 19550.

Chapter 4 2D MoN-VN Heterostructure as a Model Sulfur Host to Regulate Polysulfides for Highly Efficient Lithium-Sulfur Batteries

4.1. Introduction and Significance

Lithium-sulfur batteries are acknowledged as the most promising next generation batteries. However, their performance is limited by loss of active sulfur material (polysulfides). This is because of the 'shuttle effect'. Rational design of sulfur hosts could solve this by regulating polysulfides via chemical adsorption of the polysulfides, and through improving their redox efficiency. However, at present an atomic-level understanding of chemical interaction between sulfur hosts and polysulfides is missing.

Here, a 2D MoN-VN heterostructure is designed and fabricated. It is used as a model sulfur host material to overcome the 'shuttle effect' and to gain atomic-level understanding of polysulfides adsorption features. The resulting MoN-VN-based lithium-sulfur battery displayed excellent discharge capacity and cycling stability when compared with many reported sulfur hosts. Density functional theory (DFT) calculations revealed that the electronic structure of MoN can be tailored by VN. This leads to enhanced polysulfides adsorption. In situ synchrotron X-ray Diffraction (synchrotron XRD) and electrochemical results showed efficient sulfur utilization when MoN-VN was used as the sulfur host.

The particular novelty of this work is:

1. Novel 2D MoN-VN heterostructure as a model sulfur host - We present the first report on a 2D heterostructure of MoN-VN as a sulfur host with effective regulation to polysulfides. More importantly, the 2D heterostructure provides a theoretical model for DFT calculations to investigate polysulfides adsorption behaviours.

2. DFT calculations and in situ synchrotron XRD - DFT calculations reveal that the

incorporation of VN can tailor electronic structure of MoN in the MoN-VN heterostructure, leading to enhancement of polysulfides adsorption. Additionally, in situ synchrotron XRD and electrochemical measurements suggested effective sulfur regulation and utilization when MoN-VN is used as a sulfur host.

3.   Superior performance - The 2D MoN-VN-based lithium-sulfur battery offers a highly significant capacity of 708 mA h g-1 at 2C and an excellent operational stability with a low capacity decay of 0.068 % per cycle during 500 cycles. This performance is meaningfully superior to many currently reported.

4.2. 2D MoN-VN Heterostructure as a Model Sulfur Host to Regulate Polysulfides for Highly Efficient Lithium-Sulfur Batteries

This section is included as a journal paper by Chao Ye, Yan Jiao, Huanyu Jin, Ashley D. Slattery, Kenneth Davey, Haihui Wang and Shi-Zhang Qiao, 2D MoN-VN Heterostructure as a Model Sulfur Host to Regulate Polysulfides for Highly Efficient Lithium-Sulfur Batteries, Angew. Chem. Int. Ed., 2018, 57, 16703-16707.

Statement of Authorship

Title of Paper	2D MoN-VN Heterostructure to Regulate Polysulfides for Highly Efficient Lithium-Sulfur Batteries
Publication Status	☑ Published ☐ Accepted for Publication ☐ Submitted for Publication ☐ Unpublished and Unsubmitted work written in manuscript style
Publication Details	Lithium-sulfur batteries hold promise for next-generation batteries. A problem however is rapid capacity fading. Moreover, atomic-level understanding of the chemical interaction between sulfur host and polysulfides is poorly elucidated from a theoretical perspective. Here, a two-dimensional (2D) heterostructured MoN-VN is fabricated and investigated as a new model sulfur host. Theoretical calculations indicate that electronic structure of MoN can be tailored by incorporation of V. This leads to enhanced polysulfides adsorption. Additionally, in situ synchrotron X-ray Diffraction and electrochemical measurements reveal effective regulation and utilization of the polysulfides in the MoN-VN. The MoN-VN-based lithium-sulfur batteries have a capacity of 708 mA h g^{-1} at 2 C and a capacity decay as low as 0.068 % per cycle during 500 cycles with sulfur loading of 3.0 mg cm^{-2}.

Principal Author

Name of Principal Author (Candidate)	Chao Ye
Contribution to the Paper	Chao Ye performed the experiments, conducted the calculations and wrote the manuscript.
Overall percentage (%)	60%
Certification:	This paper reports on original research I conducted during the period of my Higher Degree by Research candidature and is not subject to any obligations or contractual agreements with a third party that would constrain its inclusion in this thesis. I am the primary author of this paper.
Signature	Date 2019.10.31

Co-Author Contributions

By signing the Statement of Authorship, each author certifies that:

i.   the candidate's stated contribution to the publication is accurate (as detailed above);

ii.   permission is granted for the candidate in include the publication in the thesis; and

iii.   the sum of all co-author contributions is equal to 100% less the candidate's stated contribution.

Name of Co-Author	Shi-Zhang Qiao
Contribution to the Paper	Prof. Shi-Zhang Qiao conceived the project, proposed the concept and prepared the manuscript.
Signature	Date 30/10/2019

Name of Co-Author	Haihui Wang
Contribution to the Paper	Prof. Haihui Wang conceived the project, analysed the results and prepared the manuscript.
Signature		Date	2019. 10-31

Name of Co-Author	Yan Jiao
Contribution to the Paper	Dr. Jiao Yan conducted DFT calculations.
Signature		Date	31 Oct 2019

Name of Co-Author	Huanyu Jin
Contribution to the Paper	Huanyu Jin guided material synthesis.
Signature		Date	31/10/2019

Name of Co-Author	Ashley D. Slattery
Contribution to the Paper	Dr. Ashley D. Slattery conducted TEM-related characterizations.
Signature		Date	31/10 2019

Name of Co-Author	Kenneth Davey
Contribution to the Paper	Dr. Kenneth Davey prepared the manuscript.
Signature		Date	31/10/2019

85

Communications

Angewandte
Chemie

2D MoN-VN Heterostructure To Regulate Polysulfides for Highly Efficient Lithium-Sulfur Batteries

Chao Ye[+], Yan Jiao[+], Huanyu Jin[+], Ashley D. Slattery, Kenneth Davey, Haihui Wang,* and Shi-Zhang Qiao*

Abstract: Lithium-sulfur batteries hold promise for next-generation batteries. A problem, however, is rapid capacity fading. Moreover, atomic-level understanding of the chemical interaction between sulfur host and polysulfides is poorly elucidated from a theoretical perspective. Here, a two-dimensional (2D) heterostructured MoN-VN is fabricated and investigated as a new model sulfur host. Theoretical calculations indicate that electronic structure of MoN can be tailored by incorporation of V. This leads to enhanced polysulfides adsorption. Additionally, in situ synchrotron X-ray diffraction and electrochemical measurements reveal effective regulation and utilization of the polysulfides in the MoN-VN. The MoN-VN-based lithium-sulfur batteries have a capacity of 708 mA h g^{-1} at 2 C and a capacity decay as low as 0.068 % per cycle during 500 cycles with sulfur loading of 3.0 mg cm^{-2}.

Compared with lithium-ion batteries, lithium-sulfur batteries are both low-cost and low-contamination and have a high theoretical specific capacity of ≈ 1675 mA h g^{-1}.[1] However, the solubility of the intermediate lithium polysulfides (LiPoSs) results in low Columbic efficiency and rapid capacity fading.[2] Moreover, the atomic-level LiPoSs adsorption behaviour on sulfur hosts are difficult to study because of a lack of theoretical guidance. This significantly impedes design and development of efficient sulfur hosts.[3]

The surface and interface engineering of inorganic materials to construct heterostructured sulfur hosts has received significant attention in lithium-sulfur batteries.[4] This can achieve regulation of LiPoSs via enhancing LiPoSs

chemical adsorption and improving their surface redox kinetics on the heterostructured sulfur hosts, leading to increased charge/discharge capacity and cycling stability of lithium-sulfur batteries.[5] More importantly, LiPoSs adsorption ability on the heterostructured sulfur hosts can be further improved because of the novel physicochemical properties at interfaces offered by the interfacial effect.[3a] This plays an essential role in further regulating LiPoSs and therefore improving the performance of sulfur hosts in lithium-sulfur batteries. However, origin of the LiPoSs adsorption enhancement has been poorly elucidated due to a lack of atomic-level understanding of LiPoSs adsorption behaviour on the heterostructured sulfur hosts.[6]

Owing to their uniformly exposed crystal lattices, two-dimensional (2D) sulfur host materials can serve as an ideal model in density functional theory (DFT) computations—which deals mainly with LiPoSs adsorption energies and adsorption sites' identification.[7] More importantly, DFT computations can calculate electronic structures of the sulfur hosts and reveal their adsorption origin. These therefore play a key role in gaining atomic-level understanding of LiPoSs adsorption behaviour and exploring suitable sulfur host materials for high-performance lithium-sulfur batteries.[8] To date, DFT computations of various 2D one-component inorganic sulfur host materials, including layered metal oxide,[7a] metal disulfides[9] and, metal carbides, have revealed detailed LiPoSs adsorption behaviour on them.[10] However, the lack of suitable 2D heterostructured model sulfur hosts has resulted in a loose connection between DFT calculations and experimental outcomes. This underscores the difficulty in providing theoretical guidance and support for utilization of heterostructured sulfur hosts in lithium-sulfur batteries. A rational calculation model with 2D heterostructure is therefore needed to gain insight into LiPoSs adsorption origins and to guide the design of the sulfur host materials for better performance.

In this work, we design and fabricate a new 2D heterostructured MoN-VN as a model sulfur host to regulate LiPoSs and to gain atomic-level understanding of LiPoSs adsorption behavior on two-component materials. The heterostructured MoN-VN exhibited a high discharge capacity of 708 mA h g^{-1} at 2 C and a low capacity decay of 0.068 % per cycle during 500 cycles with a high sulfur loading of 3.0 mg cm^{-2}. Our DFT calculations indicate that the electronic structure of MoN is tailored by V in the heterostructure, resulting in enhanced LiPoSs adsorption of this heterostructured sulfur host. In addition, synchrotron-based near edge X-ray absorption fine structure (NEXAFS) and in situ synchrotron X-ray diffraction (in situ synchrotron XRD) were used to investigate the

[*] C. Ye,[+] Dr. Y. Jiao,[+] H. Jin,[+] Dr. K. Davey, Prof. S. Z. Qiao
School of Chemical Engineering, The University of Adelaide
Adelaide, SA 5005 (Australia)
E-mail: s.qiao@adelaide.edu.au

Dr. A. D. Slattery
Adelaide Microscopy, The University of Adelaide
Adelaide, SA 5005 (Australia)

Prof. H. Wang
School of Chemistry and Chemical Engineering, South China
University of Technology
Guangzhou, 510640 (China)
E-mail: hhwang@scut.edu.cn

Prof. S. Z. Qiao
School of Materials Science and Engineering, Tianjin University
Tianjin, 300072 (China)

[+] These authors contributed equally to this work.

Supporting information and the ORCID identification number(s) for the author(s) of this article can be found under https://doi.org/10.1002/anie.201810579.

relationship between the MoN-VN heterostructure and electrochemical behaviors.

The 2D heterostructural MoN-VN was fabricated using a modified salt-template method.[11] The morphology and microstructure of the MoN-VN was investigated by atomic force microscopy (AFM), scanning electron microscopy (SEM) and transmission electron microscopy (TEM). As is indicated by the AFM image (Figure 1a), the MoN-VN
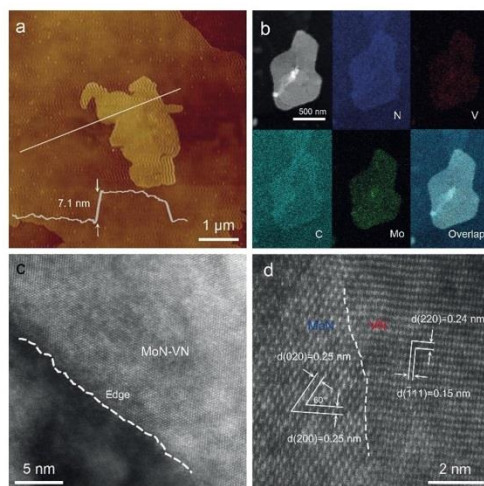

Figure 1. a, b) AFM image, HAADF-STEM image and corresponding EDS elemental maps of MoN-VN. c, d) HAADF-STEM images of the MoN-VN.

heterostructure showed a 2D morphology with a thickness of ≈7.1 nm. This is confirmed by the SEM image of Figure S1 (see Supporting Information). In addition, high-angle annular dark-field scanning transmission-electron microscopy (HAADF-STEM) energy-dispersive spectroscopy (EDS) was adopted to explore the microstructure of MoV-VN. A uniform dispersion of Mo and V indicated a homogeneous distribution of closely coupled MoN and VN nano-domains (Figure 1b). Figure 1c shows a representative 2D MoV-VN heterostrucutre with a sharp edge on graphene that is used as a conductive support (Figure S2). To aid analyzes of the heterostructure, an enlarged area of Figure 1c is presented as Figure 1d, in which the lattice fringes with lattice distance of 0.25 nm correspond to the (020) and (200) facets of the MoN, whilst those of 0.24 and 0.15, nm are ascribed, respectively, to the (220) and ($\bar{1}$11) facets of the VN.[11] In addition, the distinct interfaces seen between the MoN and VN regions demontrate the exsitence of strong coupling. To investigate the electrochemical behavior of the MoN-VN heterostructure, MoN and graphene were prepared and characterized as control samples (Figure S3, S4 and S5). Additionally, the crystal phases of MoN-VN and MoN were analyzed by powder X-ray diffraction (XRD). All of the diffraction peaks

in the pattern of Figure S6a can be indexed to MoN and VN. This verifies that both MoN and VN structures exist in the MoN-VN heterostructure—and is strongly consistent with the HADDF-STEM observation. In contrast, as-prepared MoN was shown to be pure and single-phase (Figure S6b). Despite 2D VN nanosheets also being prepared via similiar method but without addition of Mo-precursor, an impurity of VO_x can be seen in the XRD pattern (Figure S6b).

The electronic structure of the MoN-VN heterostructure was studied by Mo L-edge near-edge X-ray absorption fine structure (NEXAFS) (Figure 2a). The single main peaks in
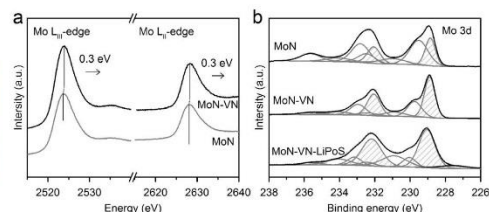
Figure 2. a) Synchrotron NEXAFS Mo L_{III}-edge and L_{II}-edge spectrums of MoN-VN and MoN. b) Mo 3d XPS spectrums of MoN, MoN-VN and MoN-VN-LiPoS, in which red, blue, green and grey curves refer to Mo^{3+}, Mo^{4+}, Mo^{5+} and Mo^{6+}, respectively.

Mo L_{III}-edge and L_{II}-edge spectrums of MoN-VN and MoN represent transitions from $2p_{1/2}$ and $2p_{2/3}$ initial states to 4d states in Mo with a relative low oxidation state. This is strongly consistent with independent reports.[12] Compared with peak positions of L_{III}-edge and L_{II}-edge in MoN (2523.7 eV and 2624.0 eV), the shift of those in MoN-VN to a higher energy (2524.0 eV and 2624.3 eV) implies a higher oxidation state of Mo in MoN-VN. This might originate from a reduced eletron density of Mo in MoN-VN heterostructure due to the strong coupling between MoN and VN.[13] Further, Mo-3d X-ray photoelectron spectra (XPS) of the MoN-VN and MoN were obtained to investigate the change of Mo oxidation states (Figure 2b). In comparison to the peak of Mo^{3+} $3d_{5/2}$ in the MoN (228.9 eV), that of the MoN-VN sample showed a slightly positive shift to 229.0 eV—underscoring the coupling between MoN and VN. In addition, the peak at 513.8 eV in V 2p XPS spectrum of MoN-VN reveals that the main V speice is V^{3+} of VN, and confirms the existence of VN phase in the MoN-VN heterostructure (Figure S7).[14] XPS was also conducted to investigate the chemical adsorption of LiPoSs on the MoN-VN and MoN (Figure 2b and Figure S8). Mo^{3+} $3d_{5/2}$ signals detected in the LiPoS-treated MoN-VN (MoN-VN-LiPoS) and LiPoS-treated MoN (MoN-LiPoS) shifted to a higher energy of 229.1 eV and 229.0 eV, respectively, indicating the transfer of coupled electrons from S_x^{2-} in LiPoS to Mo^{3+}. To compare further adsorption capabilities of LiPoSs of the sulfur hosts, MoN-VN, MoN and graphene were treated with a 0.5 mM LiPoS for 4 h. As illustrated in Figure S9, LiPoSs adsorption capability on the hosts is MoN-VN > MoN > graphene.

The sulfur electrodes were denoted as S/MoN-VN, S/MoN. Sulfur content in the S/MoN-VN was 58.5% (Fig-

ure S10–S12). Rate capabilities of the S/MoN-VN were, respectively about 1436, 1156, 988, 870, and 636 mAh g^{-1} when cycled at 0.1, 0.2, 0.5, 1, and 2 C (Figure 3a and b). When the current density was switched back to 0.2 C,
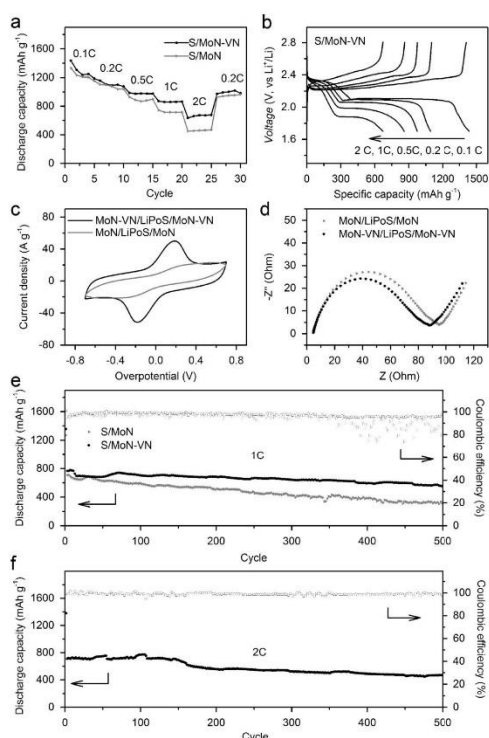

Figure 3. a) Rate capabilities of the two sulfur electrodes. b) Discharge/charge curves of S/MoN-VN at different rates. c) CV curves and d) Nyquist plots of the MoN-VN/LiPoS/MoN-VN and MoN/LiPoS/MoN symmetrical cells. d) cycling performances and CE of the two sulfur electrodes at 1 C.

a discharge capacity of 972 mAh g^{-1} was maintained. In contrast, the S/MoN electrode can deliver only 1332 mAh g^{-1} at 0.2 C—and this was decreased to less than 500 mAh g^{-1} at high rate of 2 C (Figure 3a and S13). Cyclic voltammetric (CV) tests of symmetrical cells were performed to investigate redox kinetics of the LiPoSs in the different sulfur hosts. LiPoSs redox peaks were readily observed when MoN-VN was used as the working electrode (Figure 3c). This suggests that incorporation of VN in the MoN-VN heterostructure accelerates dynamically the redox reactions of LiPoSs when compared with MoN as working electrodes. It is widely accepted that the electrochemically active surface areas (ECSAs) of a material with similar composition, are proportional to the linear slope of current density versus scan rate. CV curves under scan rates from 20 to 200, mVs^{-1} demon-

strated that MoN-VN exhibited meaningfully greater active surface areas than MoN as sulfur hosts. This was owing to its more favorable heterostructures (Figure S14).[15] These were verified by electrochemical impedance spectra (EIS), indicating significant enhancement of redox kinetics of LiPoSs by the MoN-VN heterostructure (Figure 3d). The semicircle in the Nyquist plots, corresponding to the charge transfer resistance (R_{ct}) at electrode/LiPoSs interfaces, reduced when MoN-VN was used as the working electrode. This confirmed an enhancement of the redox kinetics of LiPoSs by the MoN-VN heterostructure.[16] The S/MoN-VN demonstrated an initial capacity of 766 mAh g^{-1} and a capacity retention of 72% (555 mAh g^{-1} after 500 cycles) at 1C (Figure 3e). Importantly, the morphology and structure of the heterostructured sulfur host and the sulfur electrode, remained stable following 700 cycles (Figure S15). In addition, cycling performance of heterostructured sulfur hosts with different Mo:V atomic ratios was also tested. Results showed that a ratio of about 8:1 (Mo:V) is the optimal (Figure S16). In contrast, S/MoN showed a reduced capacity retention of 45%. Reversible capacity at 2 C of S/MoN-VN was 708 mAh g^{-1}, and the corresponding capacity decay was 0.068% per cycle during 500 cycles (Figure 3f and S17). Additionally, the corresponding Colulombic efficiency to S/MoN-VN stabilized at around 99% after 500 cycles. This excellent cycling stability of S/MoN-VN is superior to most metal oxide, metal sulfide, or hybrid electrodes widely reported (Tables S1, Supporting Information). Moreover, the soft-packaged lithium-sulfur batteries with the heterostructured sulfur electrodes exhibited stable performance under different bending states (Figure S18). The electrochemical performances of the S/graphene electrode were also investigated, which showed the lowest rating and cycling performance amongst the three sulfur electrodes (Figure S19).

To gain atomic-level insight into adsorption behaviour of LiPoSs on MoN-VN, we used DFT calculations to investigate the adsorption energy (E_a) of LiPoSs on the MoN (002) surface without and with V doping.[17] To be specific, Mo sites on the (002) surface of MoN were substituted by V atom (denoted as V-MoN) to demonstrate the surface effect on chemical adsorption of Li$_2$S$_2$ and Li$_2$S$_4$. Figure 4a and b show the optimized configurations of the Li$_2$S$_2$ and Li$_2$S$_4$ adsorption on the V-MoN surface (denoted as V-MoN-Li$_2$S$_2$ and V-MoN-Li$_2$S$_4$), in which S atoms of Li$_2$S$_2$ and Li$_2$S$_4$ are on top of the Mo atoms next to the V atom, whilst Li atoms are away from the surface. The adsorption energies for V-MoN-Li$_2$S$_2$ and V-MoN-Li$_2$S$_4$ are −5.80 and −7.70, eV, respectively. This compares with the weaker adsorption of the Li$_2$S$_2$ and Li$_2$S$_4$ to Mo atoms on MoN surface (the adsorption energies are −5.60 and −7.62, eV, Figure 4c and d), Li$_2$S$_2$ and Li$_2$S$_4$ bind more strongly on the V-MoN surface, proving that incorporation of a V atom promotes the adsorption ability of the LiPoSs. When Li$_2$S$_2$/Li$_2$S$_4$ are adsorbed on the substrate surface, the electronic states of the substrate are interacting with that of the adsorbates, and consequently their hybridized energy levels split into two groups: one is the anti-bonding states (σ*) that normally goes across the Fermi level, and the other is the bonding orbital (σ) that is positioned under the
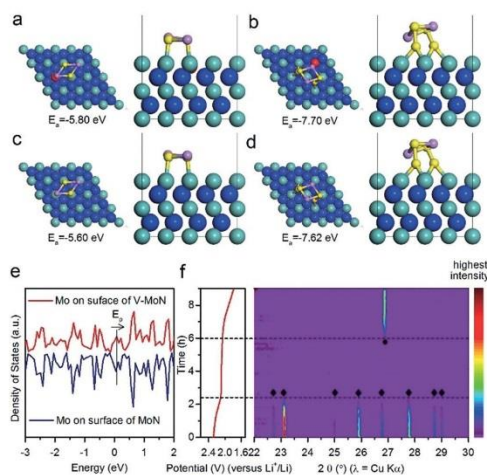
88

Figure 4. Optimized configurations of V-MoN-Li$_2$S$_2$ (a), V-MoN-Li$_2$S$_4$ (b), MoN-Li$_2$S$_2$ (c) and MoN-Li$_2$S$_4$ (d), in which green, red, purple, yellow and blue spheres represent Mo, V, Li, S and N, respectively. e) DOS of Mo on surface of V-MoN and MoN, the black line is guide for the eye. f) In situ synchrotron XRD contour plot of the S/MoN-VN with the corresponding discharge curve, in which the very right is the intensity chart. α-S$_8$ and cubic Li$_2$S are represented by diamond and circular symbols, respectively. The black dashed lines are the guidelines for the changes in the peak's intensity with the potential/time.

Fermi level. Normally, the difference of the adsorption strength comes from the anti-bonding states. Therefore, with a higher location of substrate E_p (nearest peak to Fermi Level), the anti-bonding states move higher with a lower occupancy; this leads to a stronger interaction between adsorbate and catalyst surface, and vice versa.[18] To further study the origin of adsorption enhancement of the LiPoSs on the V doped surface, we analysed the electronic structure of the MoN substrate and V-MoN substrate by calculating the density of state (DOS) of Mo atoms on the surface of MoN and V-MoN substrate (Figure S20). As is shown in Figure 4e, a higher E_p position of the Mo DOS on V-MoN is observed, compared with that of the Mo DOS on MoN. According to orbital hybridization analysis, the higher E_p position results in lower occupancy of σ*, leading to a stronger adsorption of Li$_2$S$_2$ and Li$_2$S$_4$. This explains the origin of stronger adsorption energy on V-MoN, in that Mo atoms in V-MoN exhibits a stronger interaction with adsorbed Li$_2$S$_2$ and Li$_2$S$_4$ compared with the undoped MoN surface. Therefore, the calculated DOS suggests that induction of V atoms can tailor the Mo electronic states on the surface, thereby improving the LiPoSs adsorption ability of heterostructured MoN-VN.

In situ synchrotron XRD measurements were conducted to investigate the different electrochemical behaviors during cycling where MoN-VN and MoN were used as sulfur hosts, in which modified 2032-type coin cell in transmission mode were performed using a Neware battery tester system (China) with an in-house design.[19] As is shown in Figure 4f and Fig-

ure S21, once the discharge process has started, the sharp peaks detected in both sulfur electrodes of S/MoN-VN and S/MoN can be ascribed to crystalline α-S$_8$ (JCPDS No. 008-0247).[20] In the S/MoN-VN, peaks of α-S$_8$ decreased and disappeared completely before the end of the higher plateau. This corresponds to a solid–liquid two-phase and, subsequently, liquid–liquid reaction, in which α-S$_8$ is reduced to Li$_2$S$_4$, indicating that all the α-S$_8$ reacted with lithium ions.[21] The pattern recorded close to the end of the lower voltage plateau in the S/MoN-VN reveals the appearance of a new peak at ≈27°, which can be ascribed to the cubic Li$_2$S phase (JCPDS No. 023-0369).[20] Meanwhile, the peak attributed to Li$_2$S reaches its maximum intensity at the end of the lithiation process. This observation is in good agreement with expected behaviour, according to which the system returns to the solid state.[22] In contrast, α-S$_8$ peaks in S/MoN remained for the whole process of discharge. This implies that a much higher sulfur utilization efficiency can be achieved when MoN-VN is used as a sulfur host compared with MoN (Figure S22).

In summary, we use a 2D heterostructured MoN-VN as a model sulfur host to regulate LiPoSs and gain atomic-level understanding of LiPoSs adsorption features on the MoN-VN. As confirmed by in situ synchrotron XRD, compared with the 2D MoN, the 2D MoN-VN heterostructure showed improved sulfur utilization efficiency. More importantly, according to our DFT calculations, the electronic structure of MoN can be readily tailored by incorporation of V in the heterostructure to result in enhanced adsorption capability to LiPoSs. Therefore, the MoN-VN-based lithium-sulfur batteries offer high charge/discharge capacity and excellent cycling stability. This study of the 2D MoN-VN heterostructure might provide new insight into the origin of polysulfides adsorption in the heterostructured sulfur host materials. In addition, this new 2D heterostructured material is expected to stimulate more 2D hybrid materials that might be applied in other energy storage devices for for example, sodium-sulfur batteries.

Conflict of interest

The authors declare no conflict of interest.

89

[1] F. Pei, L. Lin, D. Ou, Z. Zheng, S. Mo, X. Fang, N. Zheng, *Nat. Commun.* **2017**, *8*, 482–491.

[2] a) J. Xu, T. Lawson, H. Fan, D. Su, G. Wang, *Adv. Energy Mater.* **2018**, *8*, 1702607; b) Z. Jiang, H. Xie, S. Wang, X. Song, X. Yao, H. Wang, *Adv. Energy Mater.* **2018**, *8*, 1801433.

[3] a) Y. Zhong, L. Yin, P. He, W. Liu, Z. Wu, H. Wang, *J. Am. Chem. Soc.* **2018**, *140*, 1455–1459; b) F. Pei, T. An, J. Zang, X. Zhao, X. Fang, M. Zheng, Q. Dong, N. Zheng, *Adv. Energy Mater.* **2016**, *6*, 1502539.

[4] D. Liu, C. Zhang, G. Zhou, W. Lv, G. Ling, L. Zhi, Q. H. Yang, *Adv. Sci.* **2018**, *5*, 1700270.

[5] a) H. J. Peng, Z. W. Zhang, J. Q. Huang, G. Zhang, J. Xie, W. T. Xu, J. L. Shi, X. Chen, X. B. Cheng, Q. Zhang, *Adv. Mater.* **2016**, *28*, 9551–9558; b) J. Shan, Y. Liu, P. Liu, Y. Huang, Y. Su, D. Wu, X. Feng, *J. Mater. Chem. A* **2015**, *3*, 24148–24154; c) T. Ling, D.-Y. Yan, Y. Jiao, H. Wang, Y. Zheng, X. Zheng, J. Mao, X.-W. Du, Z. Hu, M. Jaroniec, *Nat. Commun.* **2016**, *7*, 12876.

[6] E. S. Sim, Y.-C. Chung, *Appl. Surf. Sci.* **2018**, *435*, 210–215.

[7] a) Q. Zhang, Y. Wang, Z. W. Seh, Z. Fu, R. Zhang, Y. Cui, *Nano Lett.* **2015**, *15*, 3780–3786; b) H. J. Peng, T. Z. Hou, Q. Zhang, J. Q. Huang, X. B. Cheng, M. Q. Guo, Z. Yuan, L. Y. He, F. Wei, *Adv. Mater. Interfaces* **2014**, *1*, 1400227.

[8] T. Z. Hou, X. Chen, H. J. Peng, J. Q. Huang, B. Q. Li, Q. Zhang, B. Li, *Small* **2016**, *12*, 3283–3291.

[9] G. Zhou, H. Tian, Y. Jin, X. Tao, B. Liu, R. Zhang, Z. W. Seh, D. Zhuo, Y. Liu, J. Sun, *Proc. Natl. Acad. Sci. USA* **2017**, *114*, 840–845.

[10] C. Lin, W. Zhang, L. Wang, Z. Wang, W. Zhao, W. Duan, Z. Zhao, B. Liu, J. Jin, *J. Mater. Chem. A* **2016**, *4*, 5993–5998.

[11] X. Xiao, H. Yu, H. Jin, M. Wu, Y. Fang, J. Sun, Z. Hu, T. Li, J. Wu, L. Huang, *ACS Nano* **2017**, *11*, 2180–2186.

[12] R. Bjornsson, M. U. Delgado-Jaime, F. A. Lima, D. Sippel, J. Schlesier, T. Weyhermüller, O. Einsle, F. Neese, S. DeBeer, *Z. Anorg. Allg. Chem.* **2015**, *641*, 65–71.

[13] a) C. Ye, L. Zhang, C. Guo, D. Li, A. Vasileff, H. Wang, S. Z. Qiao, *Adv. Funct. Mater.* **2017**, *27*, 1702524; b) K. Fan, H. Chen, Y. Ji, H. Huang, P. M. Claesson, Q. Daniel, B. Philippe, H. Rensmo, F. Li, Y. Luo, *Nat. Commun.* **2016**, *7*, 11981–11989; c) X. Yang, N. Yan, W. Zhou, H. Zhang, X. Li, H. Zhang, *J. Mater. Chem. A* **2015**, *3*, 15314–15323.

[14] A. M. Glushenkov, D. Hulicova-Jurcakova, D. Llewellyn, G. Q. Lu, Y. Chen, *Chem. Mater.* **2009**, *22*, 914–921.

[15] B. You, N. Jiang, M. Sheng, M. W. Bhushan, Y. Sun, *ACS Catal.* **2015**, *6*, 714–721.

[16] Z. Yuan, H.-J. Peng, T.-Z. Hou, J.-Q. Huang, C.-M. Chen, D.-W. Wang, X.-B. Cheng, F. Wei, Q. Zhang, *Nano Lett.* **2016**, *16*, 519–527.

[17] a) J. Xie, S. Li, X. Zhang, J. Zhang, R. Wang, H. Zhang, B. Pan, Y. Xie, *Chem. Sci.* **2014**, *5*, 4615–4620; b) J. Zhang, T. Wang, D. Pohl, B. Rellinghaus, R. Dong, S. Liu, X. Zhuang, X. Feng, *Angew. Chem.* **2016**, *128*, 6814–6819.

[18] Y. Jiao, Y. Zheng, K. Davey, S.-Z. Qiao, *Nat. Energy* **2016**, *1*, 16130–16138.

[19] Q. Gu, J. A. Kimpton, H. E. Brand, Z. Wang, S. Chou, *Adv. Energy Mater.* **2017**, *7*, 1602831.

[20] J. Conder, R. Bouchet, S. Trabesinger, C. Marino, L. Gubler, C. Villevieille, *Nat. Energy* **2017**, *2*, 17069–17075.

[21] J. Nelson, S. Misra, Y. Yang, A. Jackson, Y. Liu, H. Wang, H. Dai, J. C. Andrews, Y. Cui, M. F. Toney, *J. Am. Chem. Soc.* **2012**, *134*, 6337–6343.

[22] G. Zhang, Z.-W. Zhang, H.-J. Peng, J.-Q. Huang, Q. Zhang, *Small Methods* **2017**, *1*, 1700134.

90

2D MoN-VN Heterostructure to Regulate Polysulfides for Highly Efficient Lithium-Sulfur Batteries

Chao Ye[+], Yan Jiao[+], Huanyu Jin[+], Ashley D. Slattery, Kenneth Davey, Haihui Wang,* and Shi-Zhang Qiao*

anie_201810579_sm_miscellaneous_information.pdf

1. Computational Section

Density functional theory (DFT) calculations were carried out using the VASP code.[1] The exchange-correlation interaction was described by generalized gradient approximation (GGA) with the Perdew-Burke-Ernzerhof (PBE) functional.[2] The energy cutoff and Monkhorst-Pack k-point mesh was set to as 500 eV and $2 \times 2 \times 1$, respectively. During the geometry optimization, the convergence tolerance was set as 5.0×10^{-5} eV for energy and 0.05 eV Å^{-1} for force. For the construction of surface models, a vacuum of 15 Å was used to eliminate interactions between periodic images. The DFT-TS method of Grimme was employed to treat the VDW interaction.[3] E_a was calculated from:

$$E_a = E_{total} - E_{Li2Sx} - E_s$$

where E_{total}, E_{Li2Sx}, and E_s are, respectively, the energies of the whole system and polysulfides molecular clusters ($x = 2,4$) and substrate.

2. Experimental Methods

2.1 Synthesis of 2D MoN-VN and other control samples. 0.4 g Mo powder was added to 40 mL of ethanol with stirring for 30 min and 1.2 mL of H_2O_2 (30 wt%) solution was added dropwise to the Mo powder suspension. Following stirring for 48 h, the Mo-precursor solution turned blue. V-precursor solution was prepared using a similar method by adding 0.2 g of V powder in 40 mL of ethanol. Mo,V-precursor solution was obtained by mixing 2.5 mL Mo-precursor solution with 500 μL V-precursor solution with stirring for 30 min. Mo,V-precursor@NaCl was obtained by mixing 40 g of NaCl powder with the precursor solution and drying at 50 °C with stirring. The 2D MoN-VN was produced by annealing as-prepared precursor and ~15 mg graphene oxide (prepared by a modified Hummers' method) at 670 °C for 5 h at a ramp rate of 1 °C min^{-1} under a mixture of NH_3 (5 %, volume fraction) and Ar. The resulting product was washed by deionized water to remove NaCl and dispersed in 400 mL deionized water (solution A). The MoN-VN with different Mo:V atomic ratio was obtained by adjusting dosage of V-precursor. The MoN sample was obtained using the same method but without addition of precursor solution of VN. The graphene sample was obtained by annealing graphite oxide at at 670 °C for 5 h at a ramp rate of 1 °C min^{-1} under a mixture of NH_3 (5 %, volume fraction) and Ar.

2.2 Preparation of S/MoN-VN and other control sulfur electrodes. 100 mL of 0.08 M sodium thiosulfate solution was mixed dropwise with 100 mL 0.4 M PVP (M_W ~ 55 000, the concentration was calculated in terms of the repeating unit). Following stirring for 15 min, 0.8 mL of concentrated hydrochloric acid (36.5 to 38.0, %) was added to the mixture. Following further stirring for 2 h at room

1

temperature, the product was collected by centrifugation at 7000 rpm for 10 min. The product was then dispersed in 0.4 M PVP solution and recollected by centrifugation at 6000 rpm for 10 min. The mass of sulfur typically collected with this process is around 100 mg. The product was dispersed again in distilled water for use (solution B). The S/MoN-VN hybrid sulfur electrodes were fabricated by vacuum filtration of the homogeneous aqueous dispersion of solution A and solution B. The area of the as-prepared sulfur electrodes was controlled to about 1.13 cm^2.

2.3 Characterization methods. The morphologies and structures of the samples were characterized by AFM (Bruker Dimension Fast Scan), scanning electron microscope (SEM, FEI Quanta 450), transmission electron microscope (TEM, FEI Tecnai G2 Spirit), high resolution TEM (HRTEM, FEI Titan Themis 80-200), Scanning transmission electron microscopy (STEM, FEI Titan Themis 80-200), and; energy dispersive X-ray (EDX, FEI Titan Themis 80-200). X-ray diffraction (XRD) data were collected on a Rigaku MiniFlex 600 X-Ray Diffractometer. Sulfur content of the samples was determined by thermogravimetric analysis (TGA, METTLER TOLEDO TGA/DSC 2) under nitrogen with a temperature ramp of 10 °C min^{-1}. *In situ* synchrotron XRD data were collected on the powder diffraction beamline at the Australian Synchrotron with a wavelength (λ) of 0.6888 Å. Data were collected continuously in 30 s acquisitions. The cell used for the data collection was charged at a current density of 0.5 mA cm^{-2} between 1.7 and 2.8, V. The 0.1 M LiPoS solution (Li$_2$S$_x$, x ~ 6) was prepared by dissolving and mixing stoichiometric amounts of Li$_2$S and sulfur in DOL/DME (1:1 volume) at room temperature for 10 h. Five (5) mM LiPoS solution was prepared by mixing 100 μL of the 0.1 M polysulfide solution and 2 mL of DOL/DME (1:1 volume). Five (5) mg of MoN-VN, MoN, graphene was added separately to each solution. All procedures were completed in an Ar-filled glove-box.

2.4 Electrochemical measurements. The 2032-type coin cells were assembled using Celgard 2400 membranes as the separator and Li metal as the anode. The area of the sulfur electrode was approximately 3.0 cm^2. The electrolyte was prepared by dissolving 1.0 M lithium bis(trifluoromethanesulfonyl) imide in a mixture of 1,3-dioxolane (DOL) and dimethoxymethane (1:1 v/v) with the addition of 0.2 M LiNO$_3$. The volume of electrolyte injected in the coin cells was controlled to about 15 μL per 1 mg of sulfur. The galvanostatic charge/discharge measurements were performed using a LAND battery tester. The capacities were calculated based on the mass of sulfur. The electrodes for symmetrical cells were fabricated without the addition of sulfur nanospheres. Host materials (MoN-VN or MoN) were dispersed in distilled water and then filtered and cut as identical working and counter electrodes. 40 μL electrolyte containing 0.05 M as-obtained LiPoS and 0.5M LiTFSI dissolved in DOL/DME (v/v = 1/1) was added. CV measurements of the symmetrical cells were performed at -0.7 to 0.7, V at different scan rates.

2

Electrochemical impedance spectroscopy (EIS) measurements were carried out at 5 mV AC oscillation amplitude over a frequency range of 100 kHz to 100 MHz.

3

3. Supplementary Figures
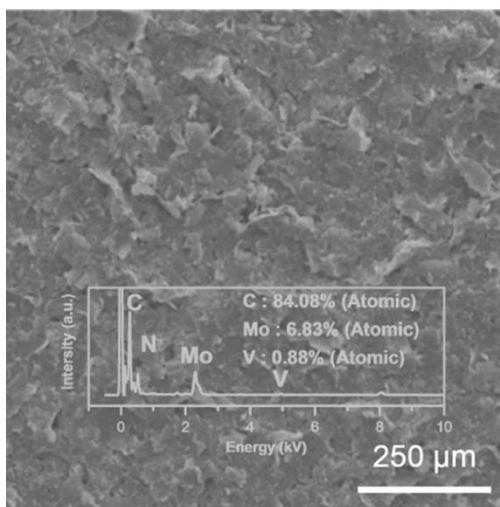
Figure S1. SEM image of MoN-VN on conductive support (inset is the corresponding EDS spectrum).
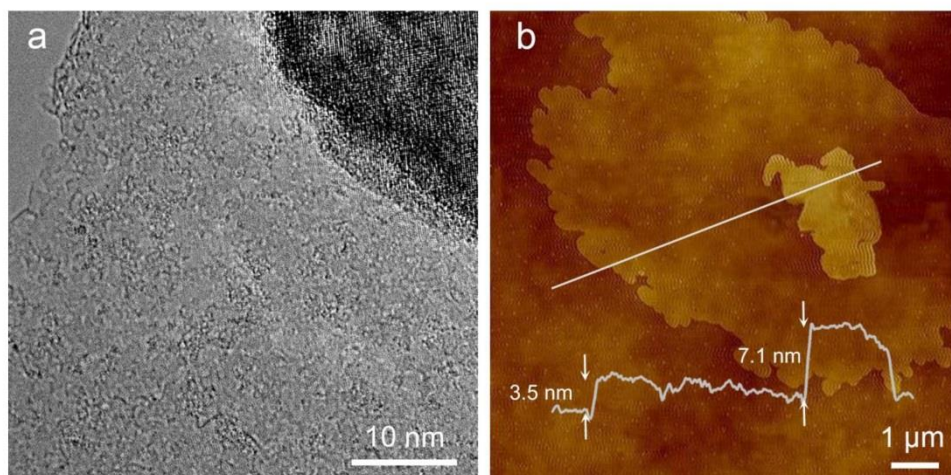
Figure S2. (a) HRTEM image and (b) AFM image of MoN-VN on conductive support.
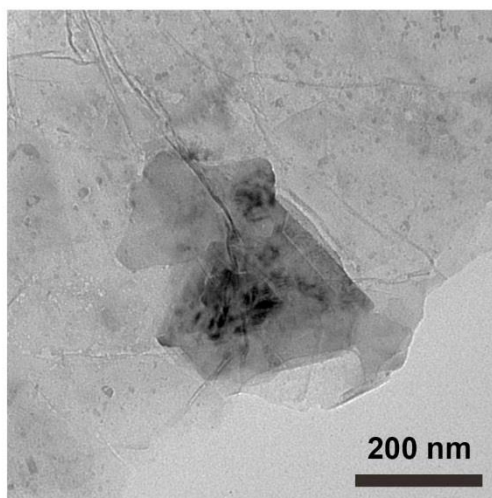
4
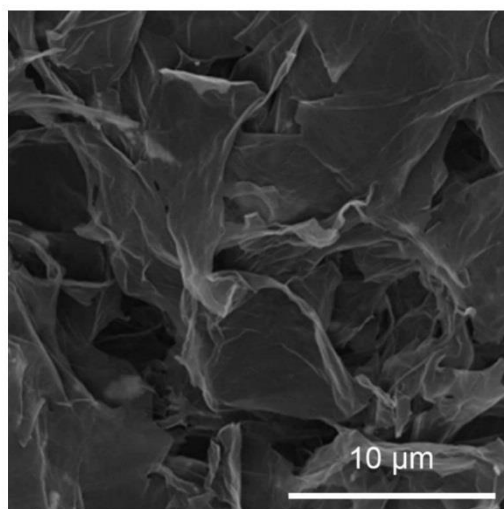
Figure S3. SEM image of graphene.
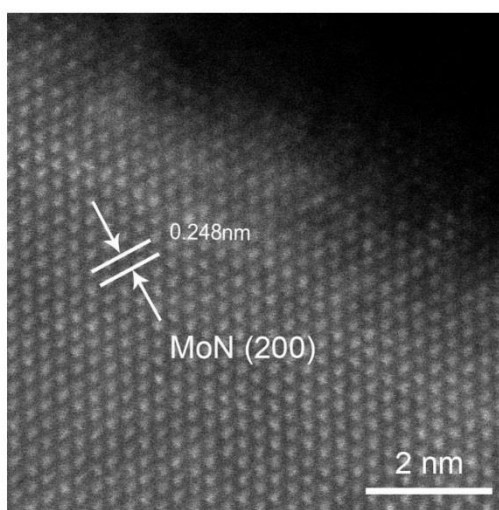

Figure S4. TEM image of MoN on conductive support.

5

Figure S5. HADDF-STEM image of the MoN.
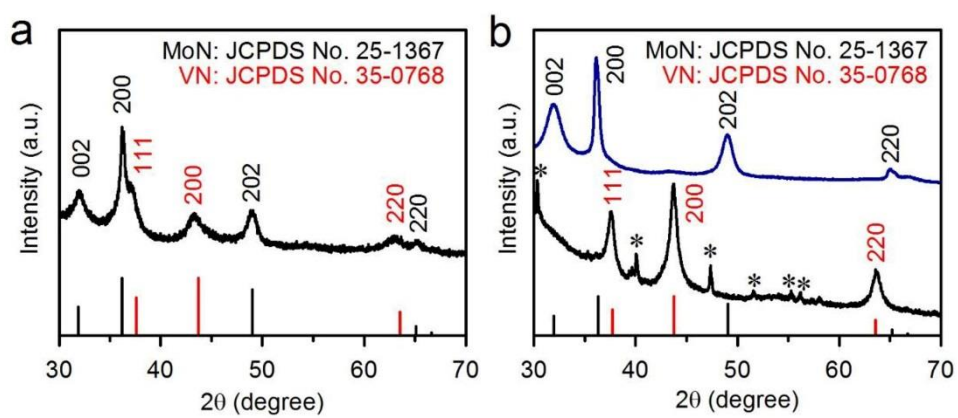
Figure S6. XRD pattern of (a) MoN-VN and (b) MoN and VN/VO$_x$.
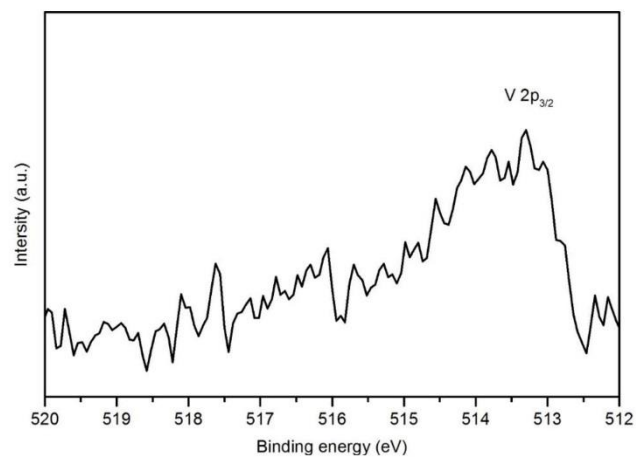
Figure S7. V 2p XPS spectrum of MoN-VN.
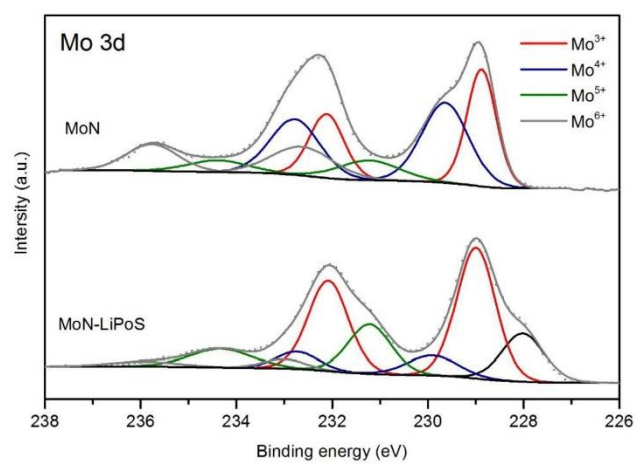
Figure S8. Mo 3d XPS spectrums of MoN and MoN-LiPoS.

7

98
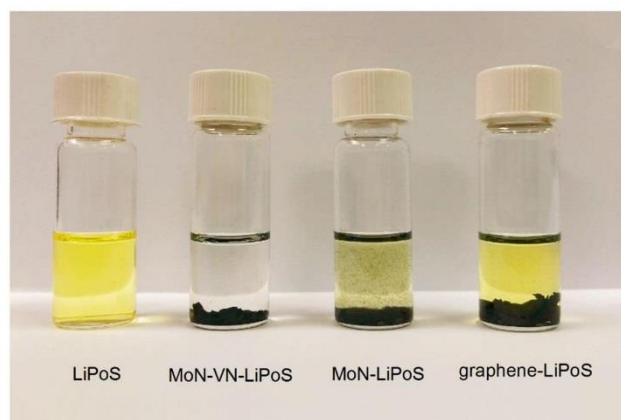
Figure S9. Optical images of blank 0.5 mM LiPoS solution, MoN-VN, MoN, and; graphene, after 4 h treatment of the LiPoS solution.

8
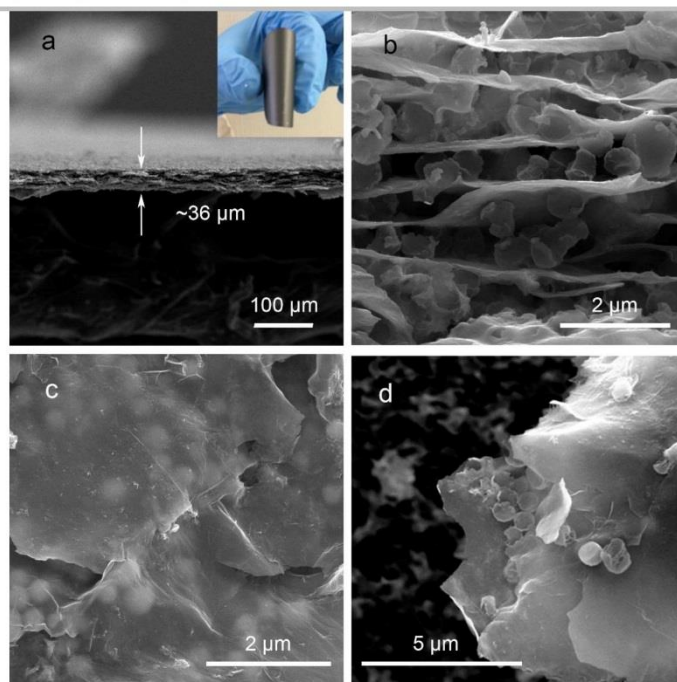
Figure S10. (a, b) Cross-section and (c, d) top-down SEM images of the S/MoN-VN electrode show clearly that the thickness of sulfur electrode was ~ 36 μm and that sulfur nanospheres with a diameter of ~ 500 nm were embedded between the MoN-VN and graphene layersof the S/MoN-VN sulfur electrode.

9
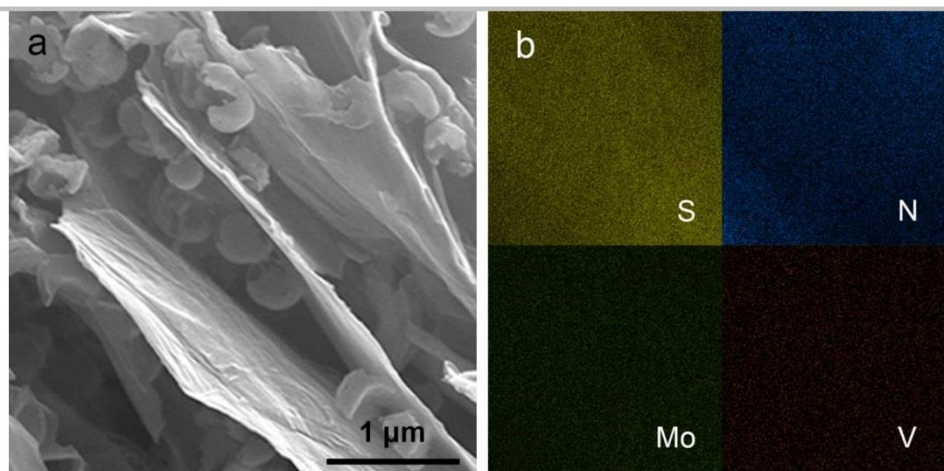
Figure S11. (a) SEM images of S/MoN-VN sulfur electrode and (b) corresponding EDS elemental maps.
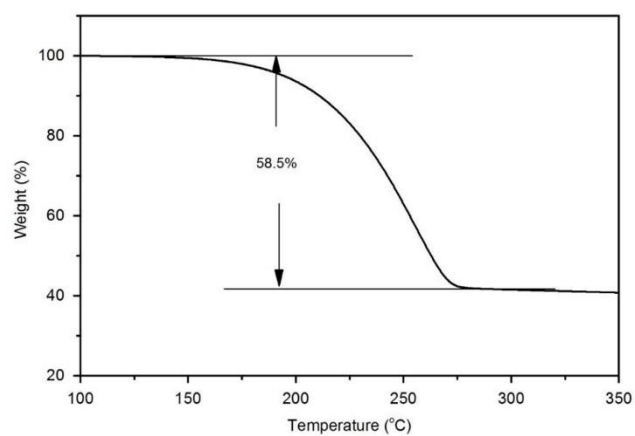
Figure S12. TGA curve of S/MoN-VN in nitrogen with a heating rate of 10 °C min^{-1}.

10
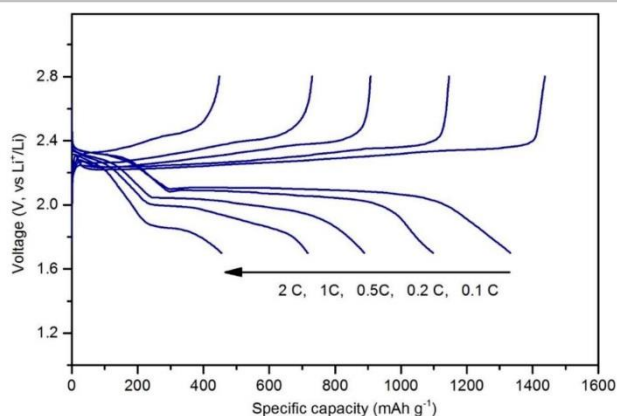
Figure S13. Discharge/charge curves during cycling at different rates of S/MoN.
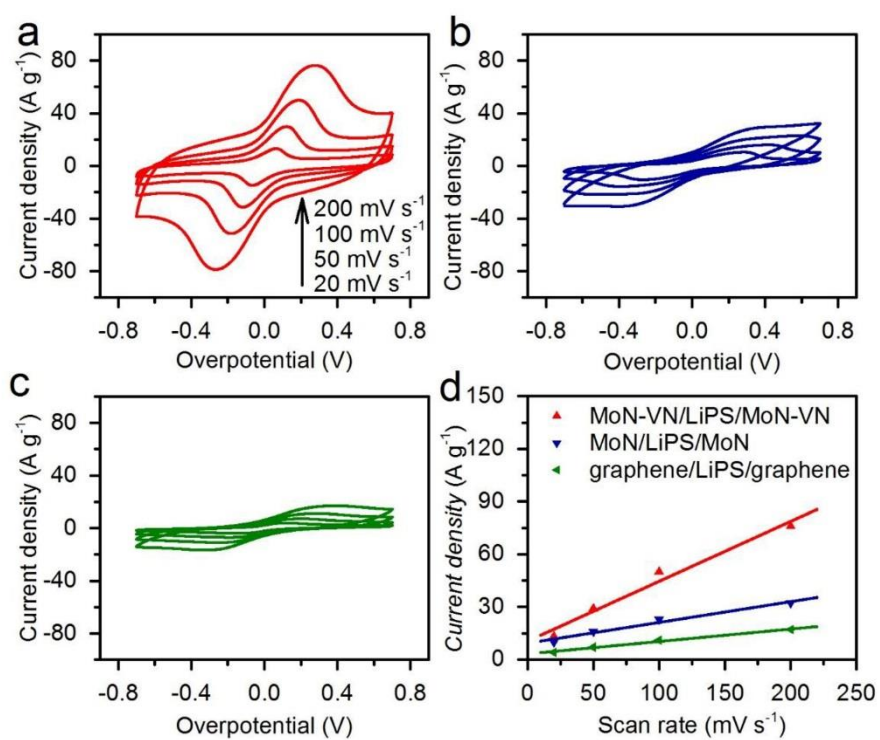
Figure S14. CV curve of (a)MoN-VN/LiPoS/MoN-VN, (b)MoN/LiPoS/MoN and (c) graphene/LiPoS/graphene symmetrical cells. (d) Scan rate dependence of the current densities of the three symmetrical cells at 0 V.

11
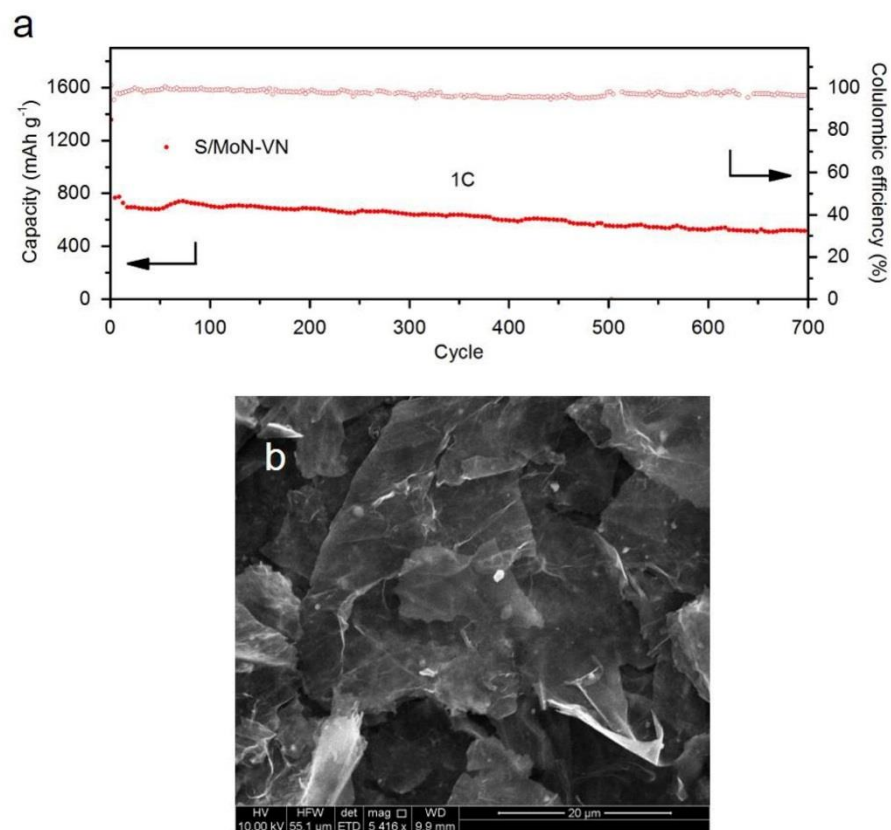
Figure S15. (a) S/MoN-VN cycling performance of 700 cycles under 1C. (b) SEM image of MoN-VN-based electrode after 700 cycles.

12
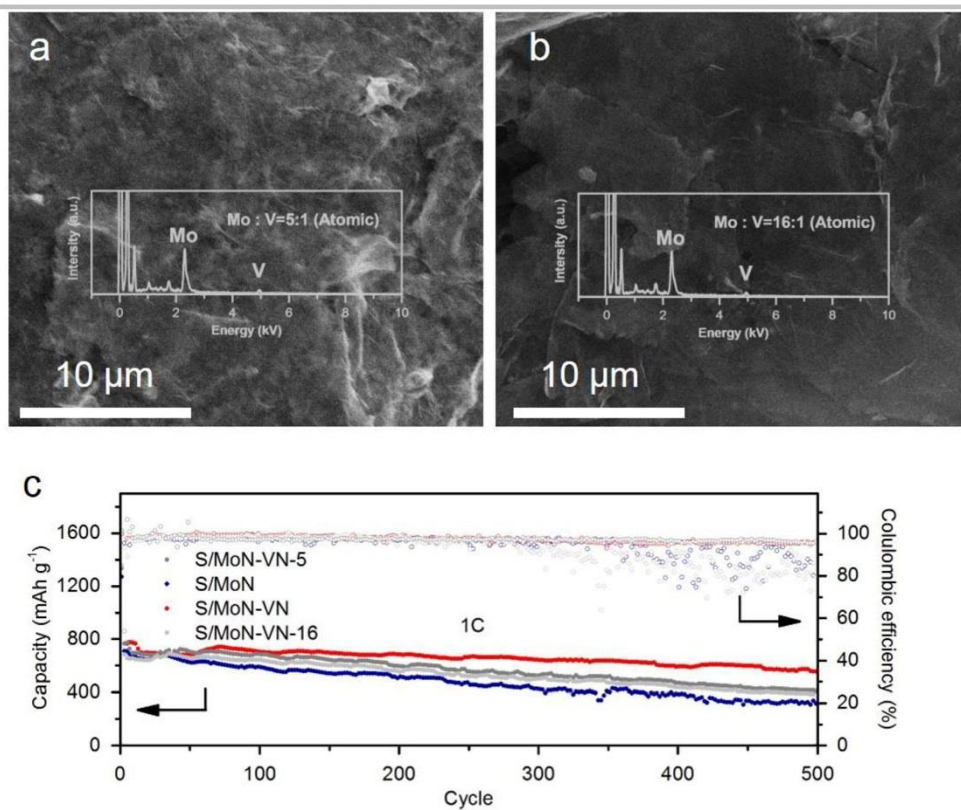
Figure S16. (a, b) SEM image of MoN-VN-5 and MoN-VN-16 with Mo:V atomic ratio of 5:1 and 16:1. (c) Cycling performance of S/MoN-VN-5 and S/MoN-VN-16 under 1C, comparing with S/MoN-VN and S/MoN.

13
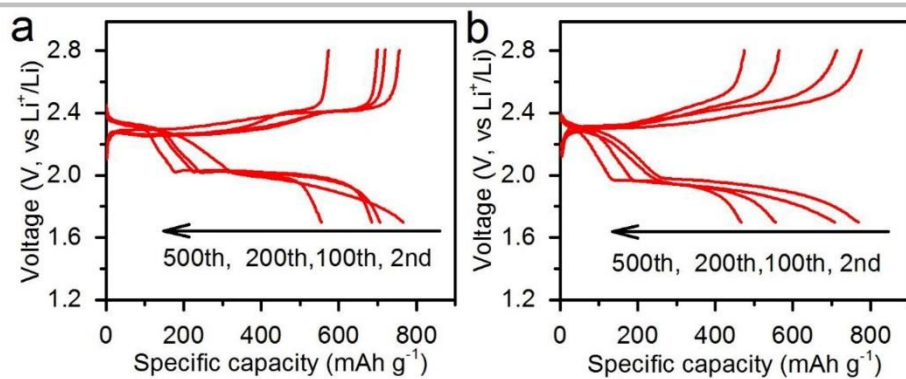
Figure S17. Discharge/charge curves of the 2nd, 100th, 200th and 500th cycle (a) at 1 C and (b) at 2C of S/MoN-VN.
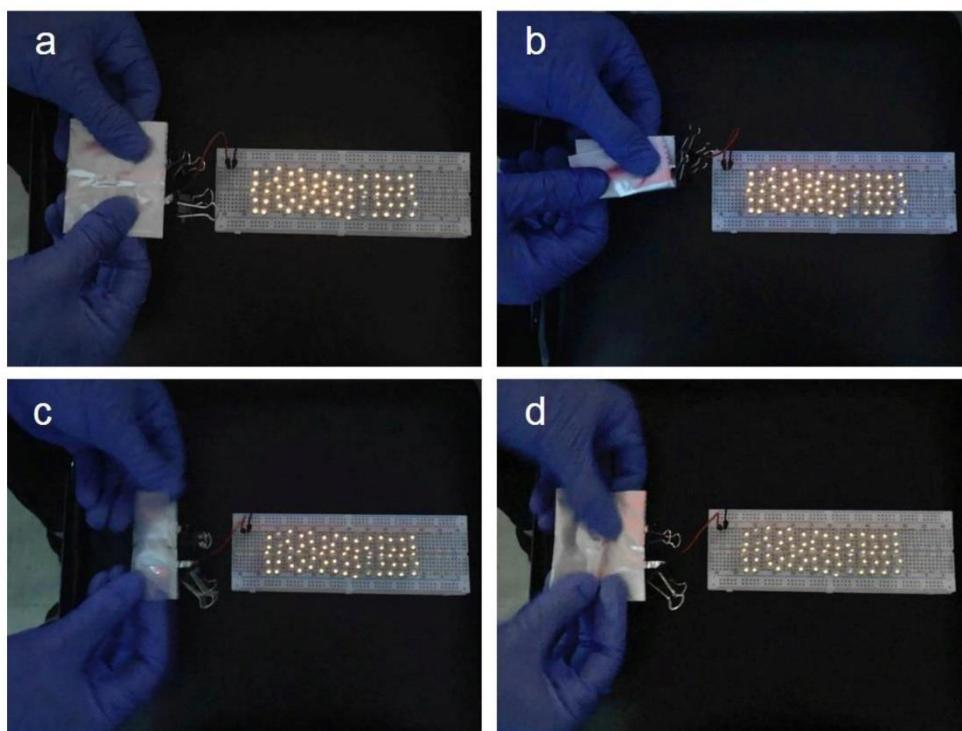
Figure S18. (a-d) Optical photography of soft-packaged lithium-sulfur battery lightening 60 LEDs under different bending states.

14
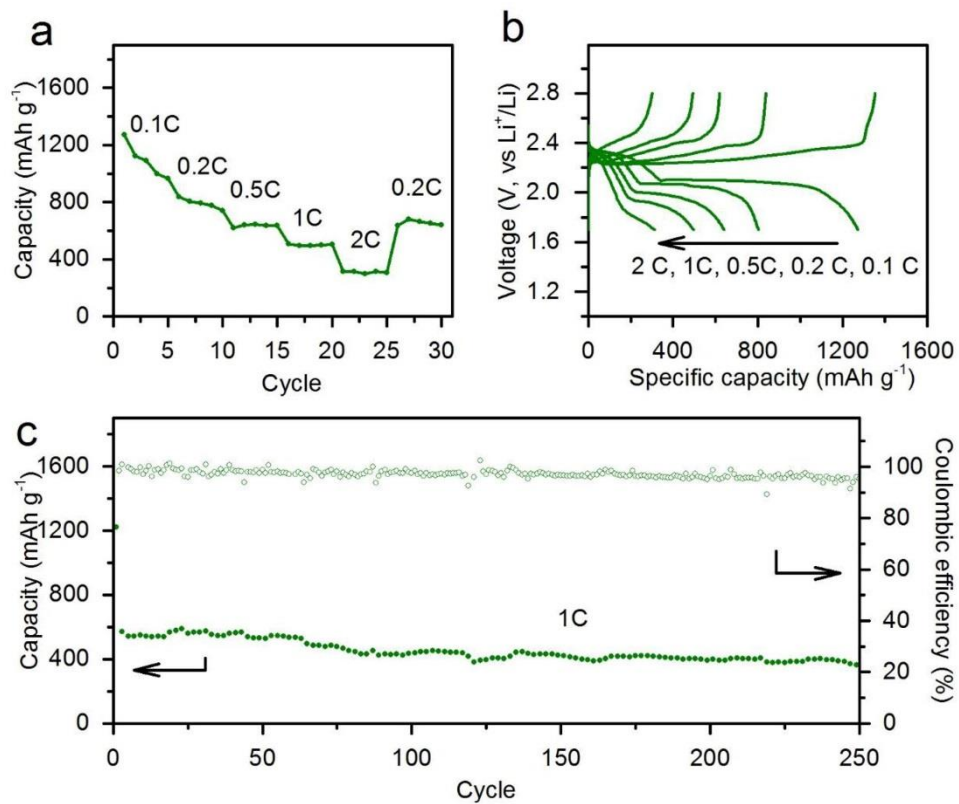
Figure S19. (a) Rating capabilities, (b) discharge-charge curves at different current densities, and; (c) cycling performance of the S/graphene at 1C in the voltage range 1.7 to 2.8, V.

15
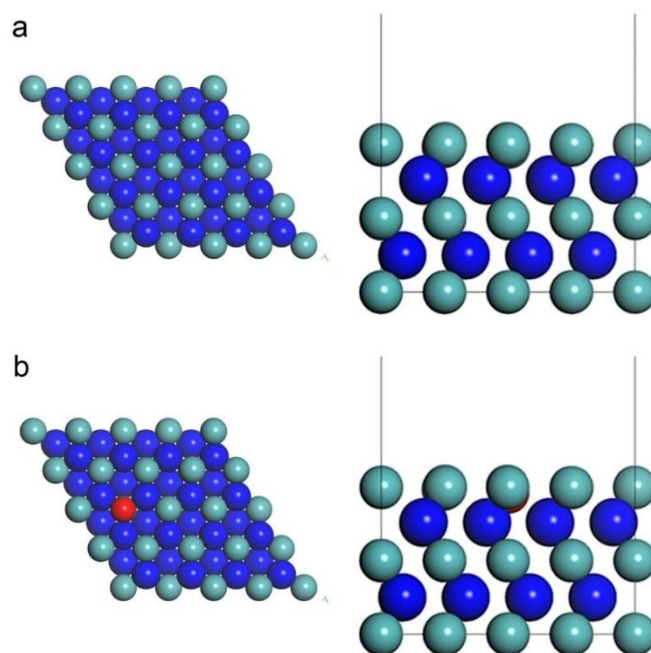
Figure S20. Optimized configurations of MoN substrate (a) and V-MoN substrate (b).
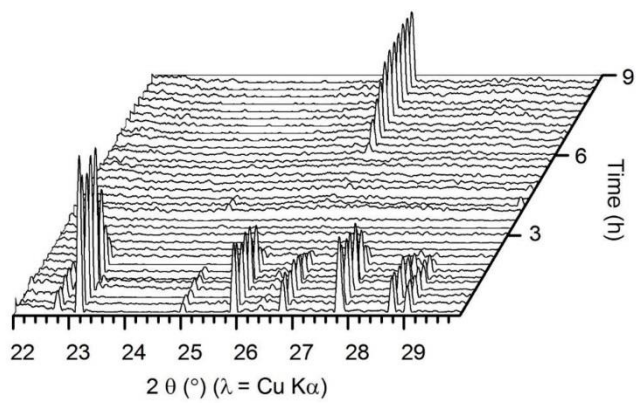
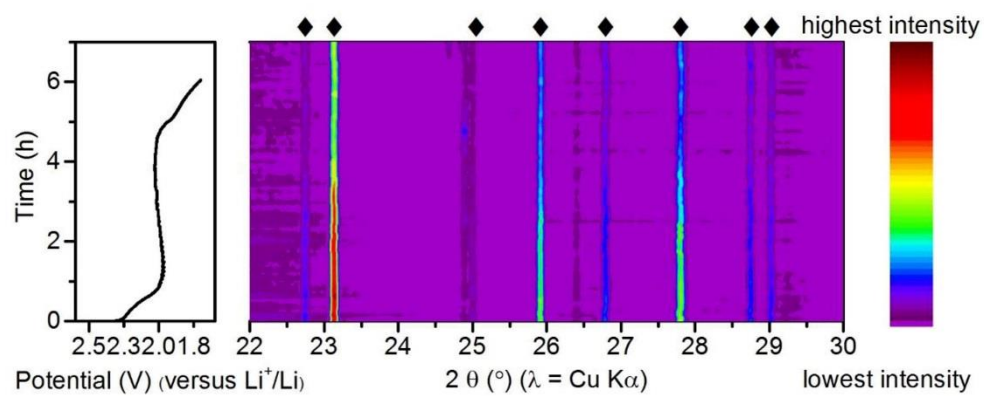**Figure S21.** Waterfall representation of XRD patterns in Figure 4f.

16

Figure S22. *In situ* synchrotron XRD contour plot of the S/MoN with the corresponding discharge curve.

17

4. Supplementary Tables

Table S1. Comparison performance from this work with similar composites.

Sample	Areal mass loading of S (mg cm^{-2})	Rate	Cycles	Capacity Decay (cycle^{-1})	Capacity (mAh g^{-1})	Ref.
S/MoN-VN	3.0	2C	500	0.068 %	708	This work
S/VN/G	3.0	1C	200	0.095 %	1128	Ref. S4[4]
S/CNT/PrNP	1.1	2C	1000	0.055 %	732	Ref. S5[5]
S/Mesoporous TiN	1.0	0.5C	500	0.070 %	988	Ref. S6[6]
S/TiO@carbon	1.5	0.5C	500	0.080 %	1066	Ref. S7[7]
S/mesoporous Ti$_4$O$_7$	0.5	0.2C	400	0.073 %	1198	Ref. S8[8]
S/hollow Co$_3$S$_4$	2.5	1C	450	0.079 %	953	Ref. S9[9]
S/MnO$_2$@hollow carbon fiber	3.5-3.9	0.5C	300	~ 0.093 %	662	Ref. S10[10]
FeS$_2$ as an additive	2	0.15C	200	0.190 %	≈700	Ref. S11[11]
S/Graphene-CoS$_2$	0.4	0.2C	2000	0.034 %	554	Ref. S12[12]
S/Co$_9$O$_8$	1.5	0.5C	1500	0.045 %	289	Ref. S13[13]
	4.5	0.05	150	~ 0.318 %	~ 500	

18

5. Supplementary References

[1]   G. Kresse, J. Furthmüller, *Physical review B* **1996**, 54, 11169-11186.

[2]   J. P. Perdew, *Phys. Rev. Lett.* **1996**, 77, 3865-3868.

[3]   A. Tkatchenko, M. Scheffler, *Phys. Rev. Lett.* **2009**, 102, 073005-073008.

[4]   Z. Sun, J. Zhang, L. Yin, G. Hu, R. Fang, H.-M. Cheng, F. Li, *Nat. Commun.* **2017**, 8, 14627-14634.

[5]   L. Kong, X. Chen, B. Q. Li, H. J. Peng, J. Q. Huang, J. Xie, Q. Zhang, *Adv. Mater.* **2018**, 30, 1705219-1705225.

[6]   Z. Cui, C. Zu, W. Zhou, A. Manthiram, J. B. Goodenough, *Adv. Mater.* **2016**, 28, 6926-6931.

[7]   Z. Li, J. Zhang, B. Guan, D. Wang, L.-M. Liu, X. W. D. Lou, *Nat. Commun.* **2016**, 7, 13065-13075.

[8]   H. Wei, E. F. Rodriguez, A. S. Best, A. F. Hollenkamp, D. Chen, R. A. Caruso, *Adv. Energy Mater.* **2017**, 7, 1601616-1601625.

[9]   H. Xu, A. Manthiram, *Nano Energy* **2017**, 33, 124-129.

[10]   Z. Li, J. Zhang, X. W. Lou, *Angew. Chem.* **2015**, 127, 13078-13082.

[11]   S. S. Zhang, D. T. Tran, *J. Mater. Chem. A* **2016**, 4, 4371-4374.

[12]   Z. Yuan, H.-J. Peng, T.-Z. Hou, J.-Q. Huang, C.-M. Chen, D.-W. Wang, X.-B. Cheng, F. Wei, Q. Zhang, *Nano Lett.* **2016**, 16, 519-527.

[13]   Q. Pang, D. Kundu, L. F. Nazar, *Mater. Horiz.* **2016**, 3, 130-136.

19

Chapter 5 Electron-state confinement of polysulfides for highly stable sodium-sulfur batteries

5.1. Introduction and Significance

Confinement of polysulfides in sulfur cathodes is widely acknowledged as an important issue in eliminating the 'shuttle effect' in metal-sulfur batteries, and for subsequent practical application to large-scale, sustainable energy storage. However, there is presently no adequate mechanistic explanation for polysulfide confinement that could lead to highly stable metal-sulfur batteries.

Here we report a new mechanism for polysulfides confinement. Based on a two-dimensional met-al-organic framework (2D MOF), this new mechanism highlights for the first time a correlation be-tween local electron-states of the sulfur cathode materials and the facilitated polysulfides conversion kinetics. The performance of a room-temperature sodium-sulfur (RT Na-S) battery is amongst the best reported and surpasses that for all sulfur cathode materials in RT Na-S batteries. We conclude that our findings offer a practical means to address the shuttle effect in metal-sulfur batteries for production of highly stable metal-sulfur batteries. Highlights of this work include:

1. Confinement mechanism - We demonstrate, based on in-situ synchrotron X-ray diffraction (XRD), electrochemical experiments and density functional theory (DFT) computations, that this new mechanism involves two features: 1) Electron-rich N sites on

the MOF facilitate strong poly-sulfide adsorption by Na-N interaction, and; 2) Dynamic electron states of Ni centers enable tun-ing of Na-N interaction to further facilitates fast polysulfide conversion kinetics.

2. A chemical origin - Based on a combination of both synchrotron-based near-edge X-ray absorp-tion fine structure (NEXAFS) analyses, and DFT computations, we reveal that the generation of electron-rich N sites and dynamic electron states on Ni centers originate from charge redistribution from the bulk MOF to the 2D MOF.

3. Superior performance - We demonstrate that sulfur cathodes with 2D MOF exhibit a significantly high, reversible capacity of 347 mAh g−1 after 1000 continuous cycles under a current density of 1 C, together with an ultra-low decay of 0.042 % per cycle. This performance is amongst the best reported and is superior to all sulfur cathode materials in RT Na-S batteries.

5.2. Electron-state confinement of polysulfides for highly stable sodium-sulfur batteries
This section is included as a submitted manuscript by Chao Ye, Yan Jiao, Dongliang Chao, Tao Ling, Jieqiong Shan, Binwei Zhang, Qinfen Gu, Kenneth Davey, Haihui Wang, Shi-Zhang Qiao, Electron-state confinement of polysulfides for highly stable sodium-sulfur batteries.

Statement of Authorship

Title of Paper	Electron-state confinement of polysulfides for highly stable sodium-sulfur batteries
Publication Status	☐ Published ☐ Accepted for Publication ☑ Submitted for Publication ☐ Unpublished and Unsubmitted work written in manuscript style
Publication Details	Confinement of polysulfides in sulfur cathodes is pivotal for eliminating 'shuttle effect' in metal-sulfur batteries, which represent promising solutions for large-scale and sustainable energy storage. However, mechanistic explorations and in-depth understanding for the polysulfides confinement remain limited. Consequently, it has been a critical challenge to achieve highly stable metal-sulfur batteries. Here, we propose a new mechanism to realize effective polysulfides confinement based on a two-dimensional metal-organic framework (2D MOF). Combination of in-situ synchrotron X-ray diffraction, electrochemical measurements and theoretical computations reveals that dynamic electron states of Ni centers in the MOF enable tuning of Na-N interaction between polysulfides and the MOF in the discharge/charge process, resulting in strong polysulfides adsorption and fast polysulfides conversion kinetics. The resultant room-temperature sodium-sulfur batteries (RT Na-S) are amongst the most stable ones so far, thus demonstrating that the new mechanism opens a promising avenue for development of high-performance metal-sulfur batteries.

Principal Author

Name of Principal Author (Candidate)	Chao Ye
Contribution to the Paper	Chao Ye performed the experiments, conducted the calculations and wrote the manuscript.
Overall percentage (%)	60%
Certification:	This paper reports on original research I conducted during the period of my Higher Degree by Research candidature and is not subject to any obligations or contractual agreements with a third party that would constrain its inclusion in this thesis. I am the primary author of this paper.
Signature		Date	2019. 10-31

Co-Author Contributions

By signing the Statement of Authorship, each author certifies that:

i.   the candidate's stated contribution to the publication is accurate (as detailed above);

ii.   permission is granted for the candidate in include the publication in the thesis; and

iii.   the sum of all co-author contributions is equal to 100% less the candidate's stated contribution.

Name of Co-Author	Shi-Zhang Qiao
Contribution to the Paper	Prof. Shi-Zhang Qiao conceived the project, proposed the concept and prepared the manuscript.
Signature		Date	31/10/ 2019

114

Name of Co-Author	Qinfen Gu		
Contribution to the Paper	Dr. Qinfen Gu guided synchrotron XRD characterization.		
Signature		Date	2019. 10·31

Name of Co-Author	Kenneth Davey		
Contribution to the Paper	Dr. Kenneth Davey prepared the manuscript.		
Signature		Date	31 10 2019

Electron-state confinement of polysulfides for highly stable sodium-sulfur batteries

Chao Ye[1], Yan Jiao[1], Dongliang Chao[1], Tao Ling[2], Jieqiong Shan[1], Binwei Zhang[1], Qinfen Gu[3], Kenneth Davey[1], Haihui Wang[4,*], Shi-Zhang Qiao[1,*]

[1] School of Chemical Engineering & Advanced Materials, The University of Adelaide, Adelaide, SA 5005, Australia.

[2] School of Materials Science and Engineering, Tianjin University, Tianjin, 300072, China

[3] Australian Synchrotron (ANSTO), 800 Blackburn Rd, Clayton, VIC 3168, Australia.

[4] School of Chemistry and Chemical Engineering, South China University of Technology, Guangzhou, 510640, China

*Email: s.qiao@adelaide.edu.au ; hhwang@scut.edu.cn

Confinement of polysulfides in sulfur cathodes is pivotal for eliminating 'shuttle effect' in metal-sulfur batteries, which represent promising solutions for large-scale and sustainable energy storage. However, mechanistic explorations and in-depth understanding for the polysulfides confinement remain limited. Consequently, it has been a critical challenge to achieve highly stable metal-sulfur batteries. Here, we propose a new mechanism to realize effective polysulfides confinement based on a two-dimensional metal-organic framework (2D MOF). Combination of *in-situ* synchrotron X-ray diffraction, electrochemical measurements and theoretical computations reveals that dynamic electron states of Ni centers in the MOF enable tuning of Na-N interaction between polysulfides and the MOF in the discharge/charge process, resulting in strong polysulfides adsorption and fast polysulfides conversion kinetics. The resultant room-temperature sodium-sulfur batteries (RT Na-S) are amongst the most stable ones so far, thus demonstrating that the new mechanism opens a promising avenue for development of high-performance metal-sulfur batteries.

As a promising electrode material, sulfur benefits from low cost and high-theoretical specific capacity of ~1675 mAh g^{-1} (ref. [1]). Additionally, sulfur cathodes can be conjugated with a range of metal anodes in metal-sulfur batteries. This holds promise for practical energy-storage applications[2, 3]. However, a major drawback with metal-sulfur batteries is the 'shuttle effect'. This arises from solubility of the intermediate metal polysulfides, together with a parasitic reaction between the polysulfides and the metal anodes. This leads to a low Coulombic efficiency (CE) and a rapid capacity decay in metal-sulfur batteries[4]. For example, the shuttle effect severely hinders practical application of room-temperature sodium-sulfur (RT Na-S) batteries because of highly reactive Na[5-7]. Therefore confinement

of polysulfides in sulfur cathodes is critical to long-term stability and development of metal-sulfur batteries[2, 8].

Currently, polysulfides confinement with weak physical adsorption on carbon-based materials would inevitably inhibit their conversion kinetics, resulting in a compromise between high discharge capacity and low capacity decay of the sulfur cathodes[9]. On the other hand, too strong polysulfides adsorption would cause decomposition of the polysulfides, resulting in block of the adsorption sites[10]. The keys for efficient polysulfides confinement lie in appropriate adsorption of the polysulfides and their facilitated conversion kinetics, which are largely determined by local electronic state of a sulfur cathode material[11-16]. For example, on N-doped graphene, pyridinic N with an extra pair of electrons interacts with terminal Li in lithium polysulfides to form Li bond, which greatly promote lithium polysulfides confinement[17]. However, systematic investigation to correlate local electron state with adsorption behaviors of a series of polysulfides remains very limited, which is due to the complexity of the polysulfide conversion process. For example, in the case of the RT Na-S batteries, at least five sodium polysulfides (NaPoSs) including Na_2S_5, Na_2S_4, Na_2S_2 and Na_2S are involved[18, 19]. Consequently, realizing efficient polysulfides confinement in sulfur cathodes has been a challenging topic in high-energy density metal-sulfur batteries.

Although polysulfides are too sensitive to be detected in air, advances in *in situ* synchrotron-based characterizations permit the identification of specific polysulfides and the tracking of dynamic macroscopic polysulfides conversions[6, 20, 21]. In-depth comprehension can thus be offered for macroscopic polysulfides conversion kinetics[22]. Nevertheless, atomic-level understanding for the polysulfides adsorption behaviors is imperative and remains difficult to achieve experimentally[23]. Extraordinary progress in density functional

theory (DFT) that take into account the surface chemistry and local electron state of the sulfur cathode materials is essential for investigating the polysulfides adsorption behaviors[24]. For instance, d-orbital electron numbers of the transitional metal sulfides strongly determine adsorption energies of lithium polysulfides[25]. Therefore, combination of the advanced *in-situ* synchrotron characterizations and computational quantum chemistry can reveal the mechanism of polysulfides confinement on cathode materials. One can engineer potential sulfur cathode materials with efficient polysulfides confinement by tailoring their electron states. It is thus urgently required for introducing the aforementioned advanced methodology to the field of metal-sulfur batteries.

Here we report a new mechanism for polysulfides confinement based on a two-dimensional metal-organic framework (2D MOF). Using the MOF as a model together with a judicial combination of *in situ* synchrotron X-ray diffraction (XRD), electrochemical tests and DFT computations, we demonstrate that dynamic electron states of Ni centers in the MOF enable tuning of Na-N interaction between polysulfides and the MOF in the discharge/charge process, facilitating strong polysulfide adsorption and rapid polysulfides conversion kinetics. The resulting performance of the RT Na-S batteries is amongst the best ones reported so far. We report for the first time the correlation between the local electron state of the sulfur cathode materials and facilitated polysulfides conversion kinetics. Our findings offer a practical means to address the shuttle effect in metal-sulfur batteries for production of highly stable metal-sulfur batteries.

Results

Structural and electron-state characterizations of 2D Ni (II) MOFs.

A hydrothermal method was adopted to fabricate a single crystal bulk $Ni_2(PymS)_4$ MOFs (Ni-MOF-bulk, PymSH = 2-mercaptopyrimidine)[26]. Morphology of the Ni-MOF-bulk was characterized by scanning electron microscopy (SEM) to reveal its layered structure (Supplementary Fig. 1). High-angle annular dark-field scanning transmission-electron microscopy (HAADF-STEM) images and corresponding energy-dispersive spectroscopy (EDX) elemental maps revealed a uniform distribution of C, N, S and Ni (Supplementary Fig. 2). Mechanical exfoliation was used on the Ni-MOF-bulk via wet ball-milling in acetone. Because of weak interaction between its layers, the Ni-MOF-bulk was readily exfoliated into 2D MOF nanosheets (Ni-MOF-2D)[27]. This was evidenced by a broad signal from 3100 to 3150 cm^{-1} in the Raman spectrum that is assigned to N$\cdots$H hydrogen bonds between layers of the Ni-MOF-bulk (Supplementary Fig. 3). In contrast, a negligible corresponding signal in the Ni-MOF-2D would imply breaking of the N$\cdots$H hydrogen bonds as a result of exfoliation[28]. The schematic, Fig. 1a, shows this layered structure of Ni-MOF-2D with a (002) interlayer-space of 0.84 nm. X-ray diffraction (XRD) patterns demonstrate that the Ni-MOF-2D maintains the original crystalline phase of the Ni-MOF-bulk, (Fig. 1b). The inset high-resolution transmission electron microscopy (HRTEM) image shows an outstanding (002) peak in Ni-MOF-2D pattern to evidence successful exfoliation of the bulk MOF[26]. Representative SEM and transmission electron microscopy (TEM) measurements were performed to aid visualization of the morphology of Ni-MOF-2D. These showed a 2D nanosheet structure (inset of Fig. 1c, Supplementary Figs. 4a and 5a). Atomic force microscopy (AFM) images confirmed this 2D morphology with a thickness of ~ 8.6 nm (Supplementary Fig. 4b). HRTEM images (Fig. 1c) together with the selected-area-electron-diffraction (SAED) pattern (Supplementary Fig. 5b) gave measured lattice distances of 0.23 nm and 0.27 nm, corresponding respectively, to the (244) and (241) facets of $Ni_2(PymS)_4$ MOFs. To provide a more detailed composition of Ni-MOF-2D, HAADF-STEM image and corresponding EDX elemental map are presented as Fig. 1d. This shows that the C, N, S and

Ni elements are uniformly distributed and confirms that the Ni-MOF-2D maintains the physical phase of pristine Ni-MOF-bulk.

Because it is reported that an optimized electron-state of cathode materials is favorable for improving discharge capacity and cycling stability of sulfur cathodes[29]. We performed density functional theory (DFT) calculations and conducted Bader charge analysis to predict the charge redistribution from the Ni-MOF-bulk to the Ni-MOF-2D[30]. Findings show that ~10 % of electrons from S transfer to Ni in processing of Ni-MOF-bulk to Ni-MOF-2D (Supplementary Fig. 6 and Supplementary Table 1)[31]. Synchrotron-based near-edge X-ray absorption fine structure (NEXAFS) characterizations were performed on both Ni-MOF-bulk and Ni-MOF-2D to investigate any structural impact on electron transfer behavior. NEXAFS is a powerful tool to provide reliable information on local electron-states. As is seen in the white-line region of N and C K-edge of Fig. 1e and 1f, the white-line adsorption energies of the Ni-MOF-bulk decrease following exfoliation. This finding indicates increased N and C electron densities in the Ni-MOF-2D nanosheets[32, 33]. Equally, according to the white-line adsorption energies, Fig. 1g and inset present a clear view of the Ni L-edge spectra in which Ni-MOF-2D exhibits increased electron density following exfoliation from Ni-MOF-bulk[24, 25]. In contrast the S K-edge spectra demonstrate a decreased electron density of S following exfoliation (Fig. 1h). X-ray photoelectron spectra (XPS) measurements were performed on the four elements of the Ni-MOF-bulk and Ni-MOF-2D to substantiate electron transfer behavior[34-38] (Supplementary Fig. 7 and Note 1). Compared with Ni-MOF-bulk, Ni-MOF-2D showed a lower valence state for C, N and Ni, and a higher for S. It is concluded that the electrons transfer from S to N, C and Ni. This is consistent with the computational results. Overall, these findings confirm a charge redistribution during the exfoliation from Ni-MOF-bulk to Ni-MOF-2D, which can be attributed to the breaking of N···H bonds between the layers[39, 40].

Electrochemical properties of NaPoSs on Ni-MOF-2D.

To investigate the electrochemical performance of the as-prepared Ni-MOFs in RT Na-S batteries, we assembled three sulfur electrodes of S/Ni-MOF-2D, S/Ni-MOF-bulk and S/conductive carbon using active materials with a sulfur mass ratio of 48.6 % (Supplementary Fig. 8). As is seen in Figs. 2a and 2b S/Ni-MOF-2D exhibited a series of advantageous discharge capacities of 516, 416, 372, 331 and 284 mAh g^{-1} when cycled at, respectively, 0.1, 0.2, 0.5, 1 and 2 C (1 C = 1675 mA g^{-1}). When current density was switched back to 0.2 C, a high discharge capacity of 406 mAh g^{-1} was maintained. In contrast, S/Ni-MOF-bulk and S/conductive carbon cathodes showed a poor rate performance with limited capacities under a high rate (Supplementary Fig. 9). As is shown in Supplementary Figs. 10 and 11 following further cycling at 0.2 C, the S/Ni-MOF-2D exhibited an ultra-low capacity decay of 0.024 % per cycle (406 to 313 mAh g^{-1} in 970 cycles). This was significantly better than that for either S/Ni-MOF-bulk (0.074 %) or S/conductive carbon (0.095 %). Long-term cycling experiments at a high rate of 1 C and 2 C were conducted to investigate electrochemical performance of S/Ni-MOF-2D (Fig. 2c and 2d, Supplementary Figs. 12-14). High capacities of 347 and 241 mAh g^{-1} were maintained after 1000 continuous cycles under 1 C and 2 C that refer respectively to low capacity decay of 0.042 % and 0.052 % per cycle, together with a stabilized CE held at around 100 %. This excellent cycling stability of S/Ni-MOF-2D is superior to those of the metal oxides, metal sulfides, or hybrid sulfur cathodes reported recently (Fig. 2e and Supplementary Table 2).

Cyclic voltammetry (CV) tests under a low scan rate of 0.1 mV s^{-1} between 0.5 and 2.8 V were performed to investigate electrochemical behaviour of sulfur and electrochemical evolution of NaPoSs from S/Ni-MOF-2D cathode. During the initial cathodic scan (Fig. 3a), two prominent peaks centered at around 2.08 and 0.73 V were observed. These corresponded

to the solid-liquid transition from elemental sulfur to Na_2S_x (long-chain NaPoSs, $6 \leq x \leq 8$) and a further reduction to, respectively, less-soluble Na_2S_2 and Na_2S. In the ensuing cathodic scan, two strong cathodic peaks at 1.59 and 0.94 V were observed that were highly-reproducible. These are related to reduction of Na_2S_x. For the anodic scan, only one reproducible peak at 1.78 V was observed. This corresponds to oxidation of Na_2S_2 and Na_2S into Na_2S_x. In contrast, CV curves of the S/Ni-MOF-bulk exhibited reduction peaks at lower potentials of 1.98, 1.58, 0.92 and 0.70 V, and an oxidation peak at a greater potential of 2.06 V. The lower potential gap between first reduction and oxidation peaks in S/Ni-MOF-2D suggests lower polarization and faster kinetics compared with those for S/Ni-MOF-bulk (Supplementary Fig. 15)[41]. Additionally, we estimated the voltage gaps (ΔE) at 50 % depth of discharge (DOD). These are closely related to electrode polarization (Supplementary Table 3). S/Ni-MOF-2D exhibited a lower ΔE_{2D} than either S/Ni-MOF-bulk or S/conductive carbon. This finding indicates significant enhancement of NaPoSs redox kinetics on the Ni-MOF-2D and is consistent with the CV observations[42].

To further investigate the NaPoSs'electrochemical and adsorption behavior on Ni-MOF-2D, *in situ* synchrotron XRD measurements were conducted in transmission mode. A modified 2032-type coin cell of S/Ni-MOF-2D was performed using an in-house design[43]. As can be seen in Fig. 3b during the initial discharge from ~ 2.2 V, two peaks at 20.2° and 12.9° were observed in the XRD patterns. These are assigned to soluble Na_2S_x (ref. 6, 13). When the battery was discharged to ~1.6 V, three new peaks emerged at 11.9°, 20.1° and 20.6°, corresponding, respectively, to (131), (341) and (302) facets of Na_2S_5 (JCPDF no. 77-0294). This finding reveals that the peak in the CV scan at 1.59 V is a result of the reduction of Na_2S_x to Na_2S_5. The peak at 11.6° is derived from the (220) facet of Na_2S_4 (JCPDF no.

71-0516) and was generated when the battery was discharged further to ~ 1.0 V. This indicates that the peak at 0.94 V in the CV curves can be reliably assigned to the formation of Na_2S_4. This peak for Na_2S_4 faded into a new (200) peak for Na_2S_2 (JCPDF no. 81-1771) at 12.1° when the battery was further discharged to 0.8 V. The final discharge to ~ 0.7 V revealed a peak at 10.6°. This is attributed to the (111) facet of Na_2S (JCPDF no. 77-2149). In the discharge from 0.5 to 2.8 V, most of the Na_2S in the battery was oxidized to Na_2S_x. It is notable that broader peaks are related to Na_2S_2, Na_2S_4 and Na_2S_5 when compared with narrow peaks for Na_2S_x. This is attributed to the formation of an organized Na_2S_4 and Na_2S_5 layer that is the result of strong adsorption on Ni-MOF-2D[44]. Importantly, overall results from the combination of the *in situ* synchrotron XRD and CV measurements underscore the facilitated conversion kinetics of all NaPoSs on Ni-MOF-2D.

To study the origin of the electrochemical performance of Ni-MOF-2D, we used PymSH and another Ni-based MOFs (Ni-BDC MOFs) as controls and investigated the individual roles of the heterocyclic linker and the Ni center (Supplementary Figs. 16 and 17). Results showed that both PymSH (without the Ni) and Ni-BDC MOFs (without the PymSH ligand) are inactive in sulfur cathodes. To provide an objective view of electrochemical performance of Ni-MOF-2D, we evaluated capacities normalized by electrochemically active surface areas (ECSAs) on S/Ni-MOF-2D, S/Ni-MOF-bulk and S/conductive carbon cathodes (Supplementary Fig. 18)[45, 46]. S/Ni-MOF-2D exhibted the greatest ECSA together with greatest normalized capacity under 0.2 C, 1 C and 2 C (Supplementary Table 4). The former finding is attributed to the more exposed active sites of the 2D morphology. The latter demonstrates a highly efficient NaPoSs confinement on Ni-MOF-2D from strong chemical adsorption and fast redox kinetics towards NaPoSs[47]. It is concluded therefore that the linkers and Ni centers synergistically contribute to NaPoSs adsorption and conversion kinetics on Ni-MOF-2D.

Mechanistic investigation of NaPoSs adsorption on Ni-MOF-2D

To explore the mechanism of NaPoSs adsorption on Ni-MOF-2D, a series of spectra surveys were carried out. Raman spectra of Ni-MOF-2D and NaPoSs-treated Ni-MOF-2D (Ni-MOF-2D-NaPoSs) were investigated to study the change in the chemical environment of the heterocyclic linker. As is shown Fig. 4a, right inset, stretching bands (ν ring) of heterocyclic linker ring were observed in the range 1450-1650 cm^{-1}. These are good indicators of the electron density of the linker[48]. The bands centered at 1565 and 1533 cm^{-1} in the Ni-MOF-2D actually downshift to 1563 and 1533 cm^{-1} following treatment with NaPoSs. This finding suggests that the heterocyclic linker interacts with NaPoSs via electron transfer[49]. Importantly, the left inset shows that the C-S bond stretching vibration band (ν C-S) at 1167 cm^{-1} in Ni-MOF-2D upshifts to 1179 cm^{-1} in Ni-MOF-2D-NaPoS. This finding indicates a decrease in electron density on S following interaction with NaPoSs. NEXAFS characterizations were carried out on Ni-MOF-2D-NaPoS to investigate the change in local electron density. As is shown in the regions of N K-edge, Figs. 4b and 4c, the Ni-MOF-2D exhibits increased white-line adsorption energies in comparison with those for Ni-MOF-2D-NaPoS. This finding indicates electron transfer from N to NaPoSs is due to interaction between Ni-MOF-2D and NaPoSs. This is in good agreement with results of the Raman spectrum. It is therefore concluded that this interaction leads to decreased electron density on S and N and is responsible for the conjugation effect in the heterocyclic linker rings. In the C K-edge, no electron gain or loss is observed. However, a decreased Ni electron density for Ni-MOF-2D-NaPoS is demonstrated by the increased white-line adsorption energy of Ni L-edge (Fig. 4d). This is different to reported open-metal sites in 3D MOFs in which electron density would be expected to increase due to interaction with S in the lithium polysulfides.[50] Our results imply therefore that electrons of Ni are transferred to NaPoSs through the linker[51]. In contrast, Ni-MOF-bulk exhibited weak interaction with NaPoSs (Supplementary Figs. 19

and 20) as is evidenced in the Raman and NEXAFS spectra. To confirm NaPoSs adsorption capabilities of Ni-MOF-2D, Ni-MOF-bulk and the PymSH, samples were treated with a 5 mM NaPoSs solution for 1 h. As is illustrated in Supplementary Fig. 21, the adsorption capabilities of the materials are: Ni-MOF-2D > Ni-MOF-bulk > PymSH. Overall, these results underscore that NaPoSs are adsorbed on Ni-MOF-2D through interaction with the heterocyclic linker as an electron donor and NaPoSs as an electron acceptor. Notably, electron transfer behaviors are also observed on Ni centers, which might contribute to the interaction between the polysulfides and Ni-MOF-2D.

Discussion

To further gain atomic-level insights into the polysulfides confinement on Ni-MOF-2D, we performed theoretical calculations. The (002) facet was determined as an exposed surface of the Ni-MOF-2D based on the HRTEM images. *Ab initio* molecular dynamics (AIMD) calculations were applied to investigate NaPoSs adsorption energies on Ni-MOF-2D[36, 37]. The energy profile (E_a) of all five Na_2S_n molecules (n = 1, 2, ..., 5) adsorbed on the Ni-MOF-2D surface (Ni-MOF-2D-Na_2S_n) were evaluated for 4000 fs (Fig. 5a). AIMD simulations predicted E_a increases with the length of the Na_2S_n chain as approximately -4.4, -4.0, -3.9, -2.6, -2.5 eV, respectively. These high adsorption energies indicate strong adsorption of the NaPoS on Ni-MOF-2D when compared with those of reported materials in sulfur cathodes for lithium/sodium polysulfides adsorption[9]. DFT calculations were carried out to optimize the Ni-MOF-2D-Na_2S_n configurations for analyses of electron transfer induced by the adsorption. As is shown in Supplementary Fig. 22, Na in Na_2S_n locates atop the N atoms on the outermost part of the Ni-MOF-2D structure, whilst the S in Na_2S_n locates away from the surface. This finding implies that N can function as a dominant adsorption site to interact with Na in Na_2S_n. Charge difference analyses were performed to investigate the chemical

126

origin of the Na_2S_n adsorption behavior. The interaction between the Ni-MOF-2D and Na_2S_n triggers an electron transfer from the N in Ni-MOF-2D to the Na in Na_2S_n, leading to electron accumulation between N and Na together with electron depletion near N in the Ni-MOF-2D (Supplementary Figs. 22). Therefore, the electron-rich N can interact with Na in Na_2S_n as electron donors and acceptors through Na-N interaction. This finding agrees well with both the Raman and NEXAFS results. Importantly, as is shown in Fig. 5b, with Na_2S_n adsorption energies increasing from Ni-MOF-2D-Na_2S_5 to Ni-MOF-2D-Na_2S, electron states of the Ni centers tend to change from an electron accummulation state (in Ni-MOF-2D-Na_2S_5) to an electron depletion state (in Ni-MOF-2D-Na_2S). This indicates that electron transfer from Ni to N correlates with the strengthened Na-N interaction and increased adsorption energy from Na_2S_5 to Na_2S on Ni-MOF-2D, which agrees well with the NEXAFS results of Ni-MOF-2D-NaPoS.

The schematic Fig. 5c illustrates effect of the Ni centers' electron states on NaPoSs confinement. Basically, the Ni centers with high redox capability are understood to strengthen the Na-N interaction through electron transfer from the Ni-MOF-2D to the NaPoSs. This strengthened Na-N interaction should facilitate the sodiation process from Na_2S_5 to Na_2S during discharge. During charge, the weakened Na-N interaction also facilitates the desodiation process of Na_2S to Na_2S_5 due to electron transfer from the NaPoSs to the Ni-MOF-2D. Therefore, this dynamic electron transfer between Ni-MOF-2D and NaPoSs facilitates NaPoSs sodiation-desodiation kinetics on Ni-MOF-2D. The Ni centers with high redox capability appears to result from the charge redistribution of the Ni-MOF-2D[14, 52, 53]. As a result, enhanced NaPoSs adsorption and conversion kinetics on Ni-MOF-2D significantly boosts the discharge capacities and capacity retention. In contrast, the

Ni-MOF-bulk suffers from weak NaPoSs confinement. As is evidenced in the N K-edge and Ni L-edge NEXAFS spectrum of Ni-MOF-bulk-NaPoS, there is neither electron gain or loss on N and Ni atoms (see Supplementary Fig. 23). Density of states (DOS) analysis revealed a semiconducting property of Ni-MOF-2D with a smaller band gap of ~ 0.56 eV compared with those of reported MOFs in sulfur cathodes (Supplementary Fig. 24). The semiconducting property of Ni-MOF-2D is believed responsible for the enhanced electron transfer between Ni centers and the linkers. All these results demonstrate that dynamic electron states on Ni centers facilitate the polysulfides adsorption and conversion kinetics.

We conclude that our work demonstrates a new mechanism for effective polysulfides confinement on a 2D Ni (II) MOF and its chemical origin. The electrochemical performances of the resulting sulfur cathodes are shown to be superior to those of all sulfur cathode materials in RT Na-S batteries. On the basis of synchrotron-based *in situ* XRD, NEXAFS characterizations, electrochemical tests and systematic DFT computations, we demonstrated that this new mechanism includes two features: first, strong polysulfide adsorption can be facilitated by electron-rich N sites on the MOF via Na-N interaction; second, fast polysulfides conversion kinetics can be realized by tuning Na-N interaction via dynamic electron states of Ni centers, thus results in strong polysulfides adsorption and fast polysulfides conversion kinetics. We conclude that our findings offer a practical means for production of highly stable metal-sulfur batteries and for the design of electrode materials for broader applications in energy storage and conversion.

Methods

Fabrication of Ni-MOF-bulk and Ni-MOF-2D. Ni-MOF-bulk was fabricated by a hydrothermal method.[26] In a typical procedure Ni (II) acetate tetrahydrate (0.45 mmol), Potassium hydroxide (0.9 mmol) and PymSH (0.9 mmol) are placed in a 23 mL Teflon-lined stainless-steel reactor with 8 mL of water. The mixture is heated to 348 K and maintained at

this temperature for 48 h, then cooled to room-temperature (RT = 22 ^{O}C) over 5 h. Green crystals of Ni-MOF-bulk are collected, washed with water and ethanol several times and dried in air. Wet ball-milling is used to exfoliate the bulk with Ni-MOF-bulk particles dispersed in 2 mL of acetone solvent and milled continuously for 4 h on a planetary mill (with zirconia balls and vials) at a low speed of 400 rpm. The obtained green dispersion is centrifuged at 3000 rpm for 3 min to remove any large particles, including un-exfoliated Ni-MOF-bulk particles, to give a light-green colloidal suspension of Ni-MOF-2D nanosheets in ethanol. Ni-MOF-2D in the form of powder is obtained following evaporation of the ethanol from the supernatant under vacuum.

Materials characterization. The morphologies and structure of the samples were characterized by AFM (Bruker Dimension Fast Scan), SEM (FEI Quanta 450), TEM (FEI Tecnai G2 Spirit). HRTEM, HAADF-STEM and EDX images were recorded at 200 kV (Talos F200X). XRD data were recorded on a Rigaku MiniFlex 600 X-Ray Diffractometer. Sulfur content of the active material was determined by TGA (METTLER TOLEDO TGA/DSC 2) under nitrogen. *In situ* synchrotron XRD (with a wavelength λ = 0.6888 Å) and NEXAFS data were detected on the powder diffraction and the soft X-ray spectroscopy beamline in the Australian Synchrotron. The 0.1 M Na_2S_x solution (x ≈ 4) was prepared by dissolving and mixing stoichiometric amounts of Na_2S and sulfur in ethylene carbonate/propylene carbonate (EC/PC with a volume ratio of 1:1) at room temperature for 10 h. 0.5 mM Na_2S_x solution was prepared by mixing 10 µL of the 0.1 M Na_2S_x solution and 2 mL of EC/PC (volume ratio of 1:1). 5.0 mg of Ni-MOF-2D, Ni-MOF-bulk and PymSH were added separately to each solution. All procedures were completed in an Argon-filled glovebox. NaPoSs-treated samples were prepared by repeatedly washing of the as-obtained samples with ethanol before characterization.

Electrochemical characterization. For battery performance measurement, active material of the elemental sulfur and conductive carbon with mass ratio of 1:1 was sealed in a quartz

ampoule and thermally treated at 300 °C for 2 h in a nitrogen atmosphere. The slurry mixture, containing 80 wt% obtained active material, 10 wt% of conductive carbon and 10 wt% N-lauryl acrylate (LA133, purchased from Chengdu Yindile Power Supply Technology) was cast on aluminum-foil and dried at 50 °C overnight to fabricate S/conductive carbon. S/Ni-MOF-2D was fabricated by adopting 5 wt% Ni-MOF-2D instead of the conductive carbon in the S/conductive carbon. Other sulfur cathodes were fabricated via similar method. The 2032-type coin cells were assembled using glass-fiber as the separator and Na metal as the anode. The electrolyte consisted of 1.0 M NaClO$_4$ in EC/PC with a volume ratio of 1:1 and 5 wt% fluoroethylene carbonate (FEC) additive. The volume of electrolyte injected into the coin cells was controlled to 20 μL per 1 mg of elemental S. The areal active material loading in the cathode for rating performance was ~ 1.0 mg cm^{-2}. The galvanostatic charge/discharge measurements were performed using a NEWARE battery tester. The capacities were calculated based on the mass of the elemental S. The electrodes for symmetrical cells were fabricated with above sulfur cathodes as identical working and counter electrodes.

Computational methods. DFT calculations were carried out using the Vienna Ab-initio Simulation Package (VASP)[54, 55]. The exchange-correlation interaction was described by generalized gradient approximation (GGA) with the Perdew-Burke-Ernzerhof (PBE) functional[56]. The DFT-TS method of Grimme was employed to treat the VDW interaction[57].

All calculations were carried out using a plane wave kinetic energy cut-off of 600 eV. All structures in the calculations were spin-polarized and relaxed until the convergence tolerance of force on each atom was smaller than 0.05 eV. The energy convergence criteria were set to 10^{-4} eV for self-consistent calculations with a Gamma centered 2×2×1 K-point. All periodic slabs had a vacuum spacing of at least 12 Å. The slab model for Ni-MOF-2D was established based on a published Ni-MOF-bulk model[26] by keeping the Ni atoms and atoms below these fixed in the Ni-MOF-bulk as is shown in Supplementary Fig. 7b. The

dimension of such a unit cell was 8.07 × 15.75 × 17.68, Å. For AIMD simulation, cut-off energy was set to 600 eV and a Gamma centered 1×1×1 K-point was used. For charge differences and DOS calculation conducted following the AIMD tests the K-point mesh was set to, respectively, 600 eV and 6×6×1. Na_2S_n (n = 1 - 5) adsorption energies were investigated for 4000 fs (1 fs/step) within the canonical constant-temperature at 330 K, constant-volume (NVT) ensemble. E_a for each configuration was calculated from:

$$E_a = E_{total} - E_{Na2Sn} - E_s$$

where E_{total}, E_{Na2Sn} and E_s are, respectively, the energies of the whole system, Na_2S_n and substrate.

References

1. Yang, Y., Zheng, G., Cui, Y. Nanostructured sulfur cathodes. *Chem. Soc. Rev.* **42**, 3018-3032 (2013).

2. Salama, M. *et al.* Metal-sulfur batteries: overview and research methods. *ACS Energy Lett.* **4**, 436-446 (2019).

3. Hong, X. *et al.* Nonlithium metal-sulfur batteries: Steps toward a leap. *Adv. Mater.* **31**, 1802822 (2019).

4. Manthiram, A., Fu, Y., Chung, S.-H., Zu, C., Su, Y.-S. Rechargeable lithium-sulfur batteries. *Chem. Rev.* **114**, 11751-11787 (2014).

5. Xu, X. *et al.* A room-temperature sodium-sulfur battery with high capacity and stable cycling performance. *Nat. Commun.* **9**, 3870 (2018).

6. Wang, Y.-X. *et al.* Achieving high-performance room-temperature sodium-sulfur batteries with S@interconnected mesoporous carbon hollow nanospheres. *J. Am. Chem. Soc.* **138**, 16576-16579 (2016).

7. Zhang, B.-W. *et al.* Long-life room-temperature sodium-sulfur batteries by virtue of transition-metal-nanocluster-sulfur interactions. *Angew. Chem. Int. Ed.* **58**, 1484-1488 (2019).

8. Seh, Z. W., Sun, Y., Zhang, Q., Cui, Y. Designing high-energy lithium-sulfur batteries. *Chem. Soc. Rev.* **45**, 5605-5634 (2016).

9. Pang, Q., Liang, X., Kwok, C. Y., Nazar, L. F. Advances in lithium-sulfur batteries based on multifunctional cathodes and electrolytes. *Nat. Energy* **1**, 16132 (2016).

10. Chen, X., Hou, T., Persson, K. A., Zhang, Q. Combining theory and experiment in lithium-sulfur batteries: current progress and future perspectives. *Mater. Today* **22**, 142-158 (2019).

11. Li, Z., Guan, B. Y., Zhang, J., Lou, X. W. A compact nanoconfined sulfur cathode for high-performance lithium-sulfur batteries. *Joule* **1**, 576-587 (2017).

12. Zhou, J. *et al.* Rational design of a metal-organic framework host for sulfur storage in fast, long-cycle Li-S batteries. *Energy Environ. Sci.* **7**, 2715-2724 (2014).

13. Zhang, B.-W. *et al.* Atomic cobalt as an efficient electrocatalyst in sulfur cathodes for superior room-temperature sodium-sulfur batteries. *Nat. Commun.* **9**, 4082 (2018).

14. Xu, L. *et al.* Oxygen vacancies on layered niobic acid that weaken the catalytic conversion of polysulfides in lithium-sulfur batteries. *Angew. Chem. Int. Ed.* **58**, 11491-11496 (2019).

15. Zhao, M. *et al.* Activating inert metallic compounds for high-rate lithium-sulfur batteries through in situ etching of extrinsic metal. *Angew. Chem. Int. Ed.* **131**, 3819-3823 (2019).

16. Liang, J. *et al.* Kinetically enhanced electrochemical redox of polysulfides on polymeric carbon nitrides for improved lithium-sulfur batteries. *ACS Appl. Mater. Interfaces* **8**, 25193-25201 (2016).

17. Hou, T.-Z., Xu, W.-T., Chen, X., Peng, H.-J., Huang, J.-Q., Zhang, Q. Lithium bond chemistry in lithium-sulfur batteries. *Angew. Chem. Int. Ed.* **56**, 8178-8182 (2017).

18. Yu, X., Manthiram, A. Capacity enhancement and discharge mechanisms of room-temperature sodium-sulfur batteries. *ChemElectroChem* **1**, 1275-1280 (2014).

19. Kim, I. *et al.* Sodium polysulfides during charge/discharge of the room-temperature Na/S battery using tegdme electrolyte. *J. Electrochem. Soc.* **163**, A611-A616 (2016).

20. Yan, Y., Cheng, C., Zhang, L., Li, Y., Lu, J. Deciphering the reaction mechanism of lithium-sulfur batteries by in situ/operando synchrotron-based characterization techniques. *Adv. Energy Mater.* **9**, 1900148 (2019).

21. Chen, X., He, W., Ding, L.-X., Wang, S., Wang, H. Enhancing interfacial contact in all solid state batteries with a cathode-supported solid electrolyte membrane framework. *Energy Environ. Sci.* **12**, 938-944 (2019).

22. Zheng, Y., Jiao, Y., Jaroniec, M., Qiao, S. Z. Advancing the electrochemistry of the hydrogen-evolution reaction through combining experiment and theory. *Angew. Chem. Int. Ed.* **54**, 52-65 (2015).

23. Zhang, Q., Wang, Y., Seh, Z. W., Fu, Z., Zhang, R., Cui, Y. Understanding the anchoring effect of two-dimensional layered materials for lithium-sulfur batteries. *Nano Lett.* **15**, 3780-3786 (2015).

24. Hou, T. Z. *et al.* Design principles for heteroatom-doped nanocarbon to achieve strong anchoring of polysulfides for lithium-sulfur batteries. *Small* **12**, 3283-3291 (2016).

25. Chen, X. *et al.* An analogous periodic law for strong anchoring of polysulfides on polar hosts in lithium sulfur batteries: S- or Li-binding on first-row transition-metal sulfides? *ACS Energy Lett.* **2**, 795-801 (2017).

26. Zhao, Y. *et al.* A paramagnetic lamellar polymer with a high semiconductivity. *Chem. Commun.*, 1020-1021 (2001).

27. Yao, Y., Lin, Z., Li, Z., Song, X., Moon, K.-S., Wong, C.-P. Large-scale production of two-dimensional nanosheets. *J. Mater. Chem.* **22**, 13494-13499 (2012).

28. Yadav, R., Swain, D., Kundu, P. P., Nair, H. S., Narayana, C., Elizabeth, S. Dielectric and raman investigations of structural phase transitions in $(C_2H_5NH_3)_2CdCl_4$. *Phys. Chem. Chem. Phys.* **17**, 12207-12214 (2015).

29. Liu, D. *et al.* Catalytic effects in lithium-sulfur batteries: Promoted sulfur transformation and reduced shuttle effect. *Adv. Sci.* **5**, 1700270 (2018).

30. Tang, W., Sanville, E., Henkelman, G. A grid-based bader analysis algorithm without lattice bias. *J. Phys.: Condens. Matter* **21**, 084204 (2009).

31. Zheng, Y. *et al.* Hydrogen evolution by a metal-free electrocatalyst. *Nat. Commun.* **5**, 3783 (2014).

32. Bolognesi, P. *et al.* Pyrimidine and halogenated pyrimidines near edge x-ray absorption fine structure spectra at C and N k-edges: Experiment and theory. *J. Chem. Phys.* **133**, 034302 (2010).

33. Jiao, Y., Zheng, Y., Davey, K., Qiao, S.-Z. Activity origin and catalyst design principles for electrocatalytic hydrogen evolution on heteroatom-doped graphene. *Nat. Energy* **1**, 16130-16138 (2016).

34. Pei, F. *et al.* Self-supporting sulfur cathodes enabled by two-dimensional carbon yolk-shell nanosheets for high-energy-density lithium-sulfur batteries. *Nat. Commun.* **8**, 482 (2017).

35. Chen, B. *et al.* Controllable graphene incorporation and defect engineering in MoS_2-TiO_2 based composites: Towards high-performance lithium-ion batteries anode materials. *Nano Energy* **33**, 247-256 (2017).

36. Zhang, H.-L., Evans, S. D., Henderson, J. R., Miles, R. E., Shen, T. Spectroscopic characterization of gold nanoparticles passivated by mercaptopyridine and mercaptopyrimidine derivatives. *J. Phys. Chem. B* **107**, 6087-6095 (2003).

37. Jiang, Z., Xie, H., Wang, S., Song, X., Yao, X., Wang, H. Perovskite membranes with vertically aligned microchannels for all-solid-state lithium batteries. *Adv. Energy Mater.* **8**, 1801433 (2018).

38. Xiang, H., Chen, J., Li, Z., Wang, H. An inorganic membrane as a separator for lithium-ion battery. *J. Power Sources* **196**, 8651-8655 (2011).

39. Shan, J. *et al.* Charge-redistribution-enhanced nanocrystalline Ru@IrO$_x$ electrocatalysts for oxygen evolution in acidic media. *Chem* **5**, 445-459 (2019).

40. Leikin, S., Parsegian, V. A., Yang, W. H., Walrafen, G. E. Raman spectral evidence for hydration forces between collagen triple helices. *Proc. Natl. Acad. Sci. U. S. A.* **94**, 11312 (1997).

41. Chao, D. *et al.* A high-rate and stable quasi-solid-state zinc-ion battery with novel 2d layered zinc orthovanadate array. *Adv. Mater.* **30**, 1803181 (2018).

42. Zhang, J., Li, Z., Chen, Y., Gao, S., Lou, X. W. Nickel-iron layered double hydroxide hollow polyhedrons as a superior sulfur host for lithium-sulfur batteries. *Angew. Chem. Int. Ed.* **57**, 10944-10948 (2018).

43. Gu, Q., Kimpton, J. A., Brand, H. E., Wang, Z., Chou, S. Solving key challenges in battery research using in situ synchrotron and neutron techniques. *Adv. Energy Mater.* **7**, 1602831 (2017).

44. Conder, J., Bouchet, R., Trabesinger, S., Marino, C., Gubler, L., Villevieille, C. Direct observation of lithium polysulfides in lithium-sulfur batteries using operando X-ray diffraction. *Nat. Energy* **2**, 17069 (2017).

45. You, B., Jiang, N., Sheng, M., Bhushan, M. W., Sun, Y. Hierarchically porous urchin-like Ni$_2$P superstructures supported on nickel foam as efficient bifunctional electrocatalysts for overall water splitting. *ACS Catal.* **6**, 714-721 (2015).

46. Li, H. *et al.* Dense graphene monolith for high volumetric energy density Li-S batteries. *Adv. Energy Mater.* **8**, 1703438 (2018).

47. Jin, H. *et al.* Emerging two-dimensional nanomaterials for electrocatalysis. *Chem. Rev.* **118**, 6337-6408 (2018).

48. Pang, Y. S., Hwang, H. J., Kim, M. S. Adsorption of 2-mercaptopyridine and 2-mercaptopyrimidine on a silver colloidal surface investigated by raman spectroscopy. *J. Mol. Struct.* **441**, 63-76 (1998).

49. Tripathi, G. N. R., Clements, M. Adsorption of 2-mercaptopyrimidine on silver nanoparticles in water. *J. Phys. Chem. B* **107**, 11125-11132 (2003).

50. Zheng, J. *et al.* Lewis acid-base interactions between polysulfides and metal organic framework in lithium sulfur batteries. *Nano Lett.* **14**, 2345-2352 (2014).

51. Ling, T. *et al.* Atomic-level structure engineering of metal oxides for high-rate oxygen intercalation pseudocapacitance. *Sci. Adv.* **4**, eaau6261 (2018).

52. Li, G. *et al.* Chemisorption of polysulfides through redox reactions with organic molecules for lithium-sulfur batteries. *Nat. Commun.* **9**, 705 (2018).

53. Liang, X. *et al.* Tuning transition metal oxide-sulfur interactions for long life lithium sulfur batteries: The "goldilocks" principle. *Adv. Energy Mater.* **6**, 1501636 (2015).

54. Kresse, G., Furthmüller, J. Efficient iterative schemes for ab initio total-energy calculations using a plane-wave basis set. *Phys. Rev. B* **54**, 11169-11186 (1996).

55. Kresse, G. Efficiency of ab-initio total energy calculations for metals and semiconductors using a plane-wave basis set. *Comput. Mater. Sci.* **6**, 15 (1996).

56. Perdew, J. P. Generalized gradient approximation made simple. *Phys. Rev. Lett.* **77**, 3865-3868 (1996).

57. Tkatchenko, A., Scheffler, M. Accurate molecular van der waals interactions from ground-state electron density and free-atom reference data. *Phys. Rev. Lett.* **102**, 073005 (2009).

Acknowledgements

Author contributions

C. Ye, H. Wang, and S-Z. Qiao conceived the project and designed the experiments. C. Ye and D. Chao performed the experiments. C. Ye and Y. Jiao conducted the DFT calculations. T. Ling carried out the TEM and HADDF-STEM characterizations. C. Ye and Q. Gu conducted *in situ* synchrotron XRD characterization. J. Shan, and B. Zhang were involved in NEXAFS, Raman and XPS characterizations. All authors discussed the results and prepared the manuscript.

Additional information

The authors declare no competing financial interests. Supplementary information accompanies this paper on www.nature.com/naturematerials. Reprints and permissions information is available online at http://npg.nature.com/reprintsandpermissions. Correspondence and requests for materials should be addressed to S-Z. Qiao.

Competing financial interests

The authors declare no competing financial interests.
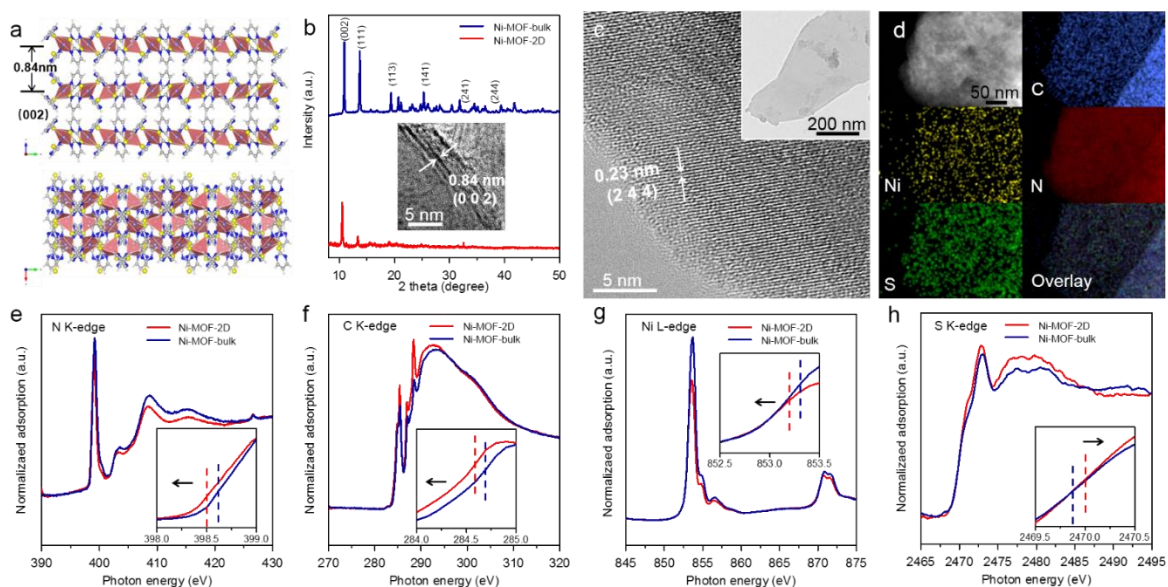
Figure 1 | Structural characterization and electron-state analyses of Ni-MOF-2D nanosheets. a, Schematic of Ni-MOF-2D with few-layer structure from side-view and top-view, in which blue, light grey, yellow, purple and white spheres represent, respectively, N, C, S, Ni and H. **b**, XRD patterns of Ni-MOF-bulk and Ni-MOF-2D. Inset is HRTEM image of the few-layer Ni-MOF-2D. **c**, HRTEM and **d**, HAADF-STEM image and corresponding EDX mapping images of Ni-MOF-2D. Inset of **c** is a representative TEM image of Ni-MOF-2D. **e-h**, N and C K-edges, Ni L-edge and S K-edge NEXAFS spectra of Ni-MOF-2D and Ni-MOF-bulk. Insets show the enlarged white-line regions.
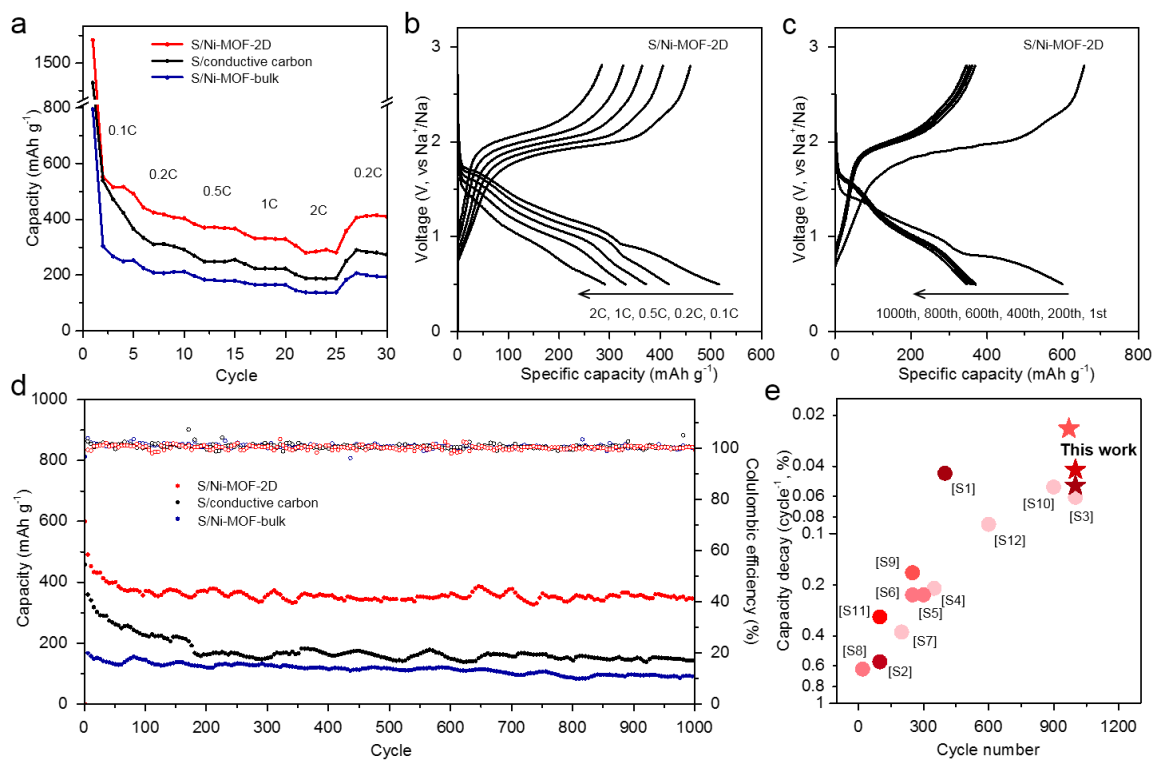
Figure 2 | Electrochemical performance of S/Ni-MOF-2D in RT Na-S batteries. a, Rating capacities of S/Ni-MOF-2D, S/Ni-MOF-bulk and S/conductive carbon. **b**, Corresponding discharge/charge curves of S/Ni-MOF-2D at different rates in **a**. **c**, Discharge/charge curves of S/Ni-MOF-2D at 1 C during 1000 cycles. **d**, Cycling performances and Coulombic Efficiencies (CE) of the three sulfur electrodes at 1 C after 0.1 C activation. **e**, Comparison of cycle numbers and capacity retentions of recently reported RT Na-S batteries with the current work in which deeper colour refers to greater current density. References for [S1] etc. are given in Supplementary References.
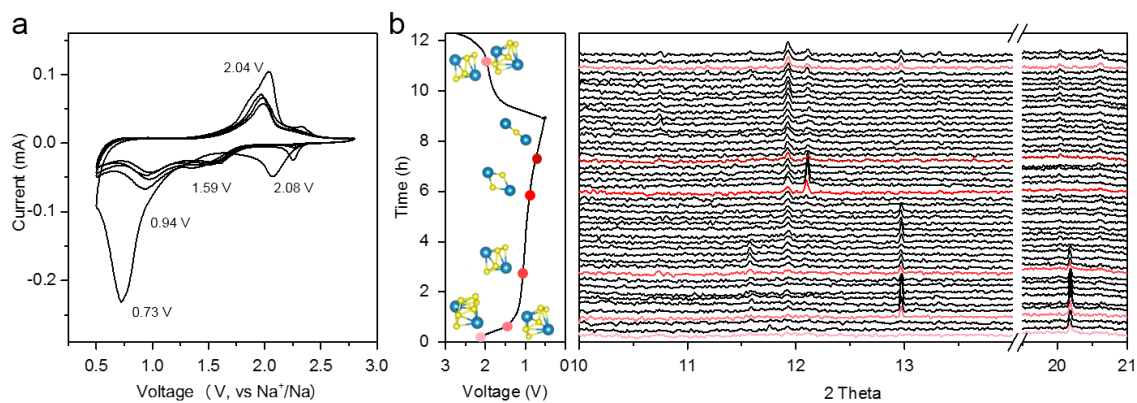
Figure 3 | Electrochemical behaviour of NaPoSs on Ni-MOF-2D. a, CV curves of S/Ni-MOF-2D at scan rate of 0.1 mV S^{-1}. **b**, Initial galvanostatic discharge/charge curve and corresponding *in situ* synchrotron XRD patterns of S/Ni-MOF-2D in which the colored patterns indicate major changes along the discharge/charge process, and; yellow and cyan spheres represent S and Na atoms, respectively.
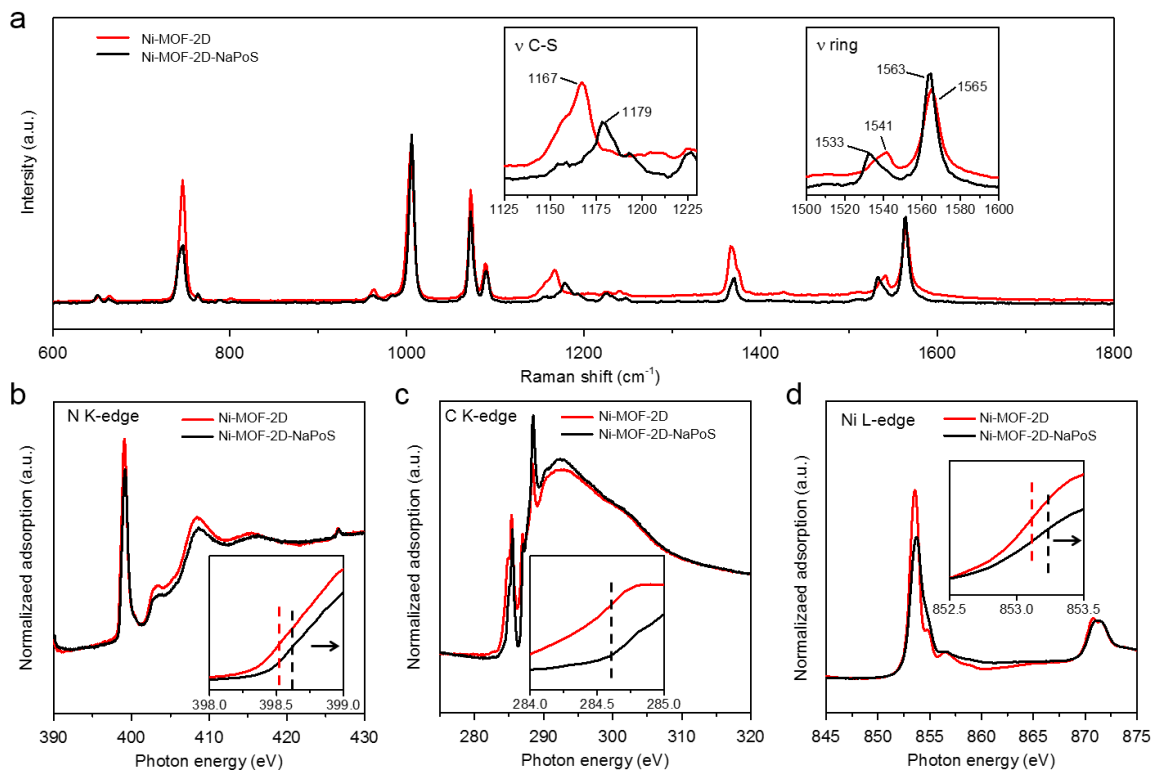
Figure 4 | Analysis of electron transfer between Ni-MOF-2D and NaPoSs. a, Raman spectra of Ni-MOF-2D and Ni-MOF-2D-NaPoS. **e-h**, N and C K-edges, Ni L-edge and S K-edge NEXAFS spectra of Ni-MOF-2D and Ni-MOF-bulk.
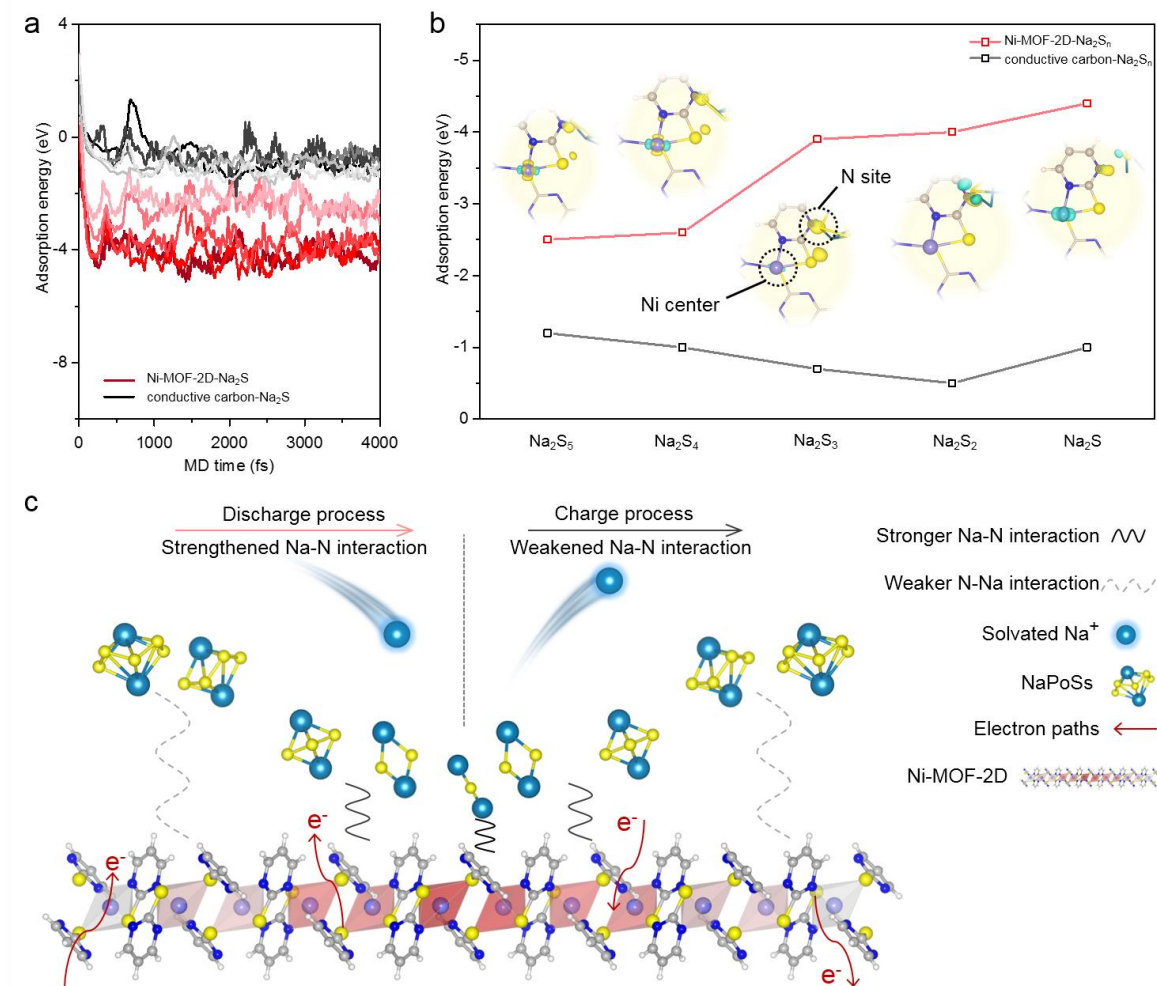
Figure 5 | Computational investigation of NaPoSs confinement on Ni-MOF-2D. a, Adsorption energies of Na_2S_n on graphene and Ni-MOF-2D as a function of *ab initio* molecular dynamics (AIMD) simulation time (fs). **b**, Adsorption energies of Na_2S_n with insets of charge difference analyzes from configurations of Ni-MOF-2D-Na_2S_n in Supplementary Figs. S22, in which yellow and cyan iso-surface represent electron accumulation and electron depletion. Color code is the same as for Fig. 1a and cyan spheres represent Na atoms. The iso-surface value is 0.005 e $Å^{-3}$. **c**, Schematic of NaPoSs confinement on Ni-MOF-2D.
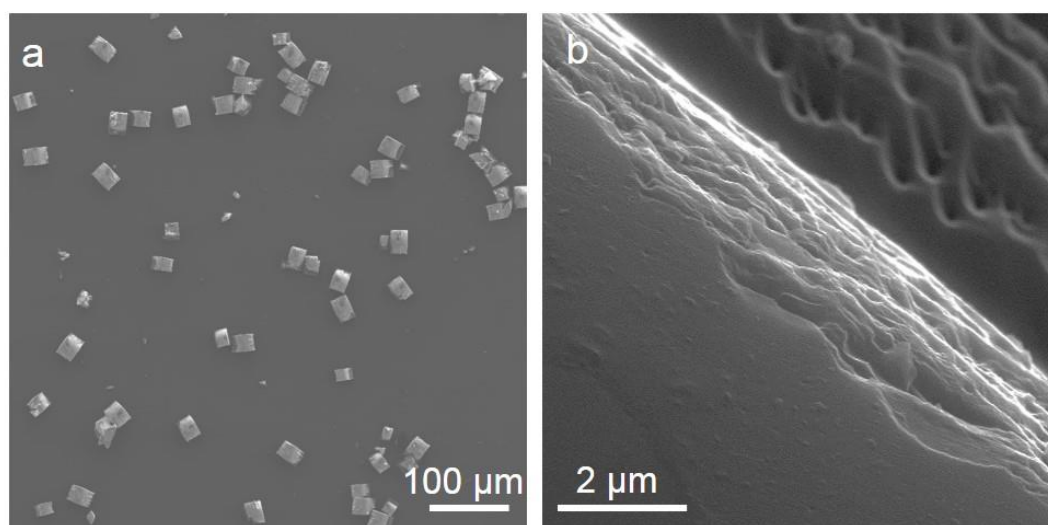
Supplementary Figure 1. SEM images of Ni-MOF-bulk.
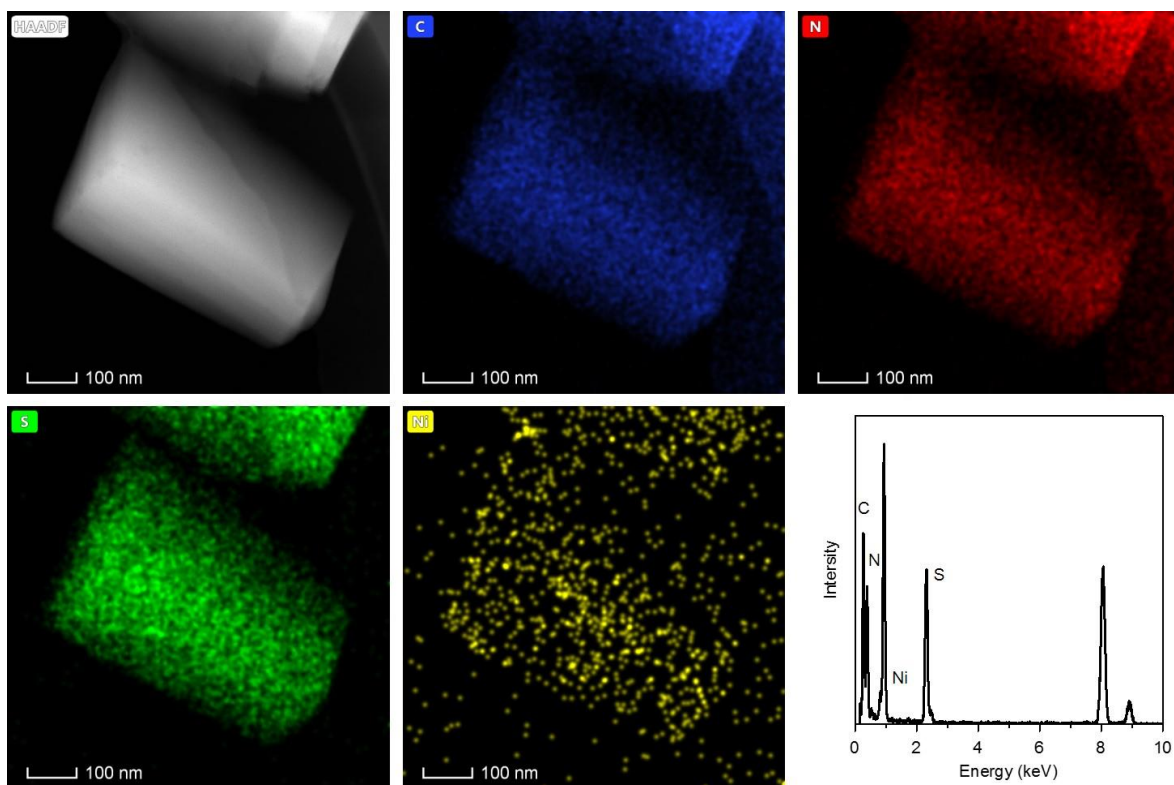
Supplementary Figure 2. EDX elemental maps of Ni-MOF-bulk.
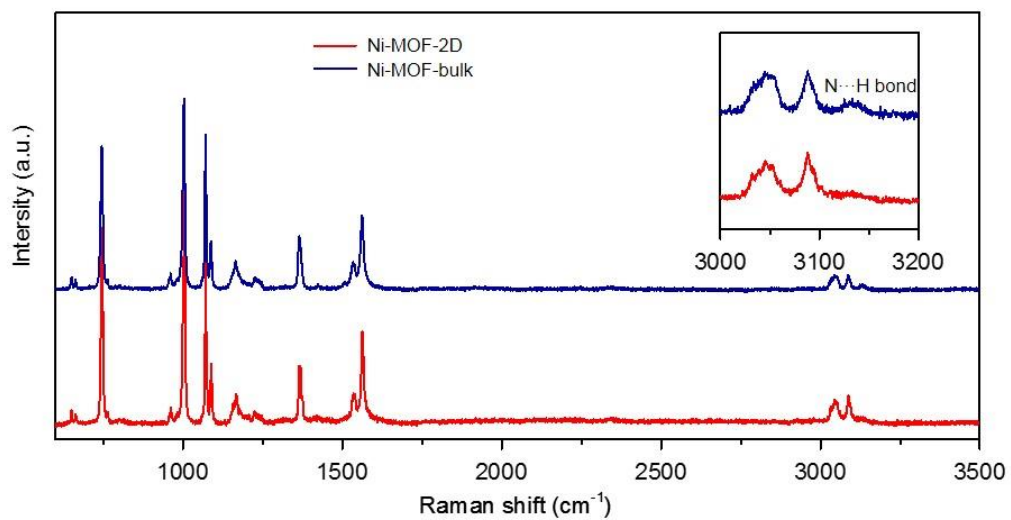
Supplementary Figure 3. Raman spectra of Ni-MOF-2D and Ni-MOF-bulk.
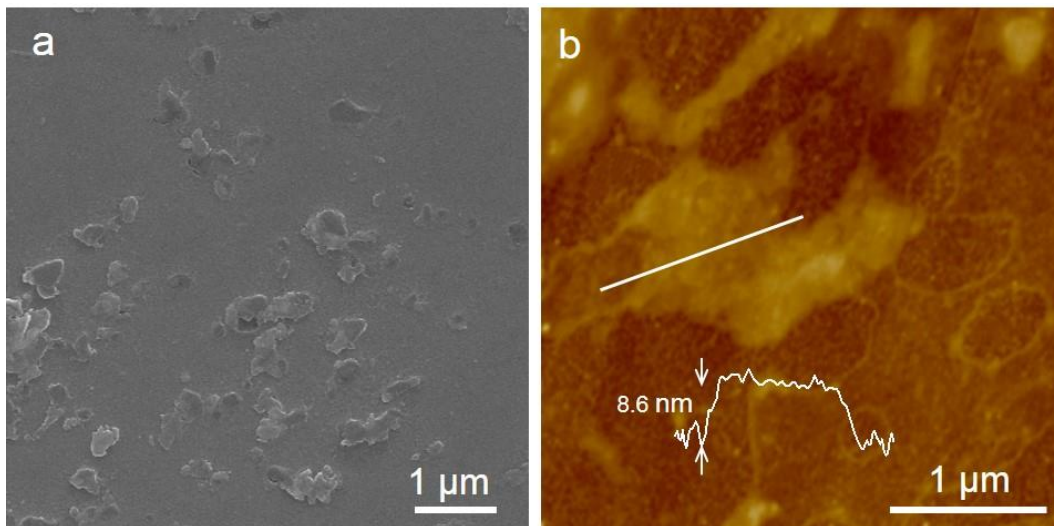
Supplementary Figure 4. a and **b** AFM and SEM images of Ni-MOF-2D.
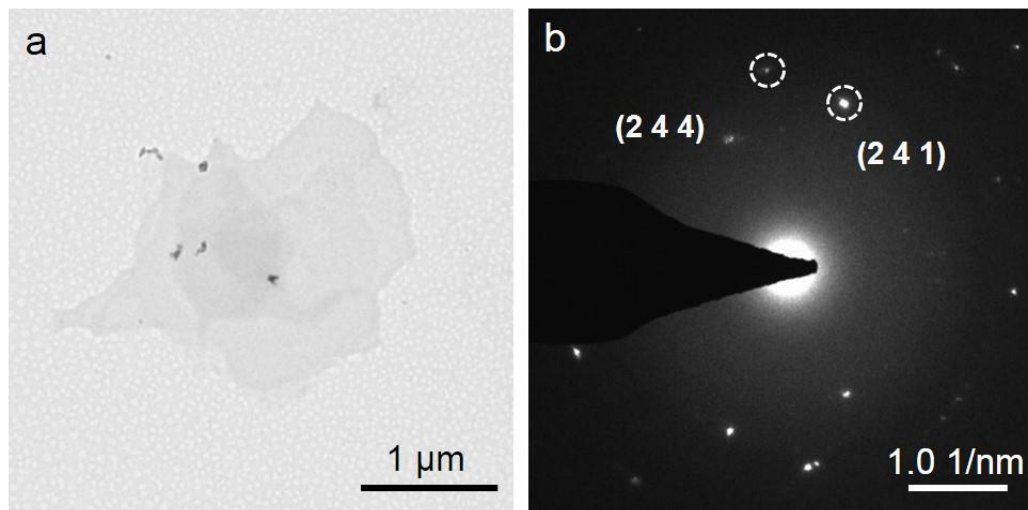
**Supplementary Figure 5. a** and **b** Representative TEM image of Ni-MOF-2D and corresponding SAED image.
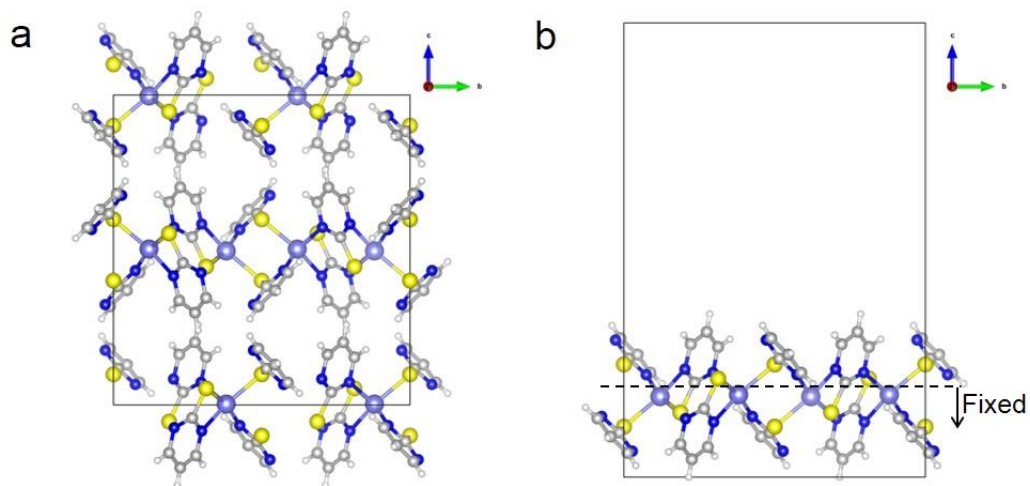
**Supplementary Figure 6. a** and **b**, Calculation model for, respectively, Ni-MOF-2D and Ni-MOF-bulk.
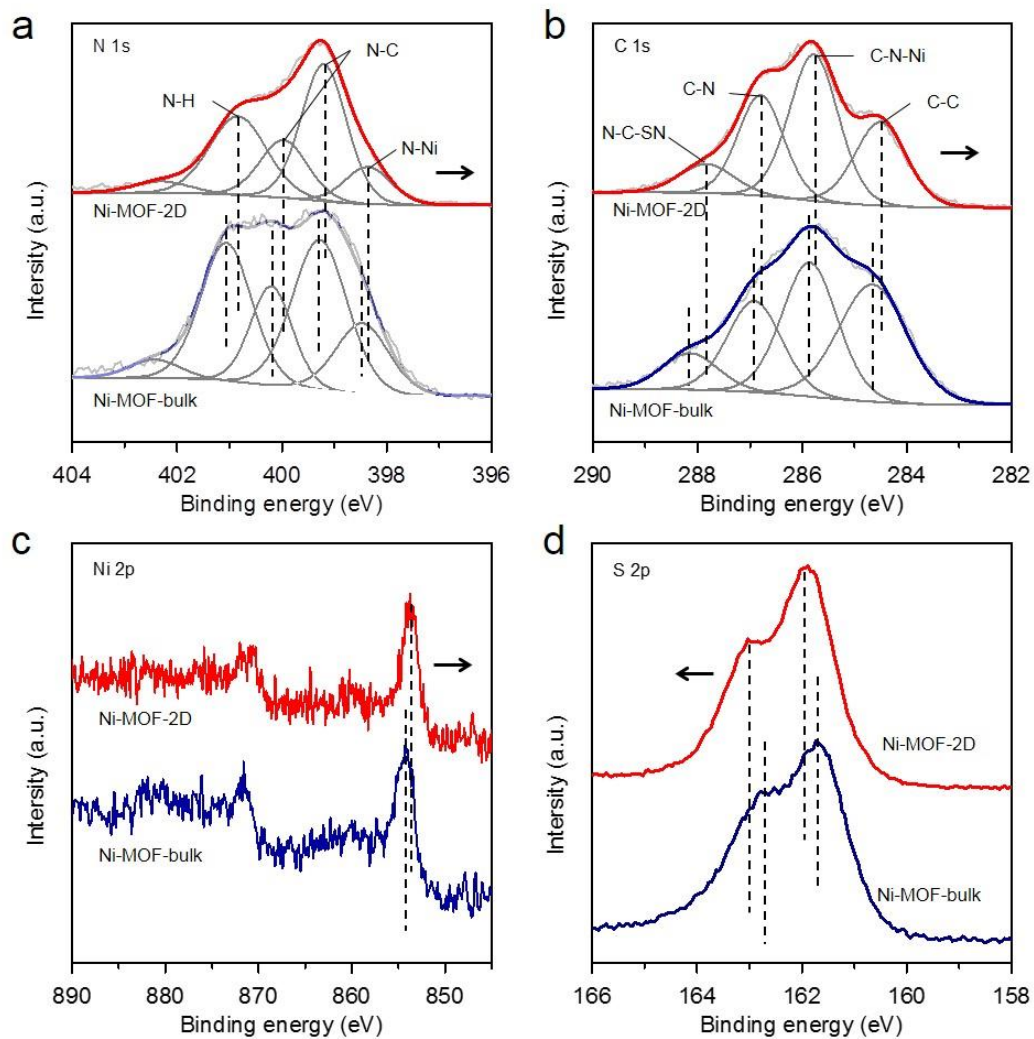
Supplementary Figure 7. Analysis of change in valence states of N, C, Ni and S between Ni-MOF-bulk and Ni-MOF-2D. a-d, N 1s, C 1s, Ni 2p and S 2p XPS spectra of the two samples.
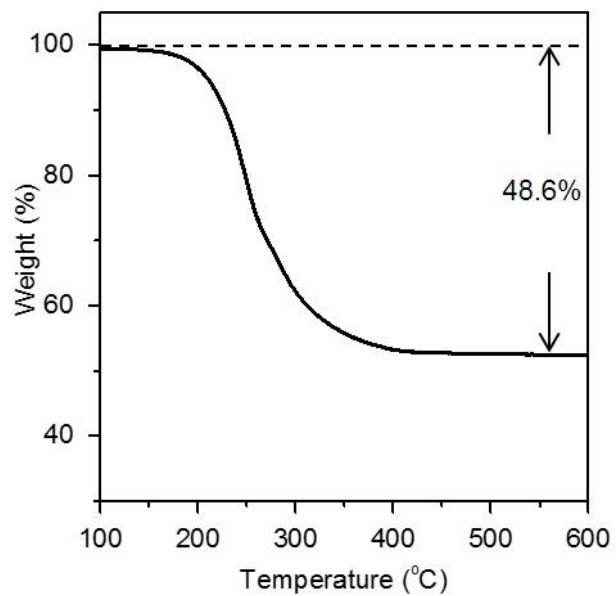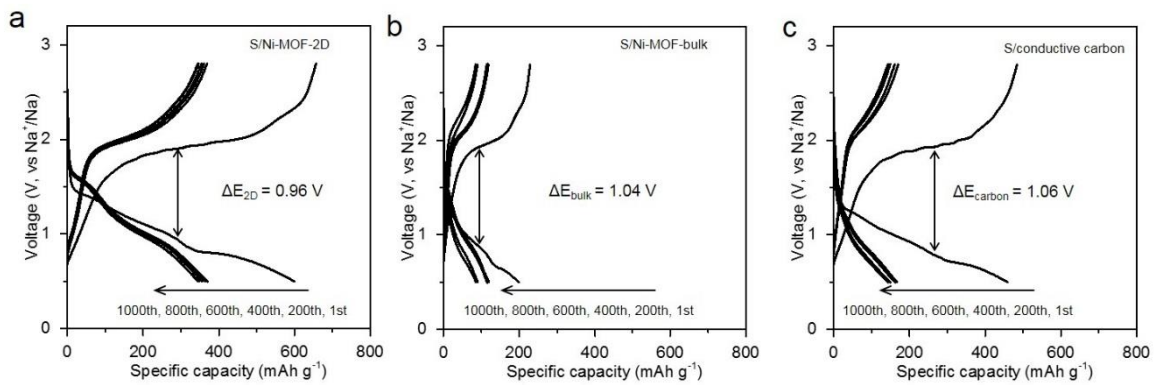
Supplementary Figure 8. TGA curve of the active material.
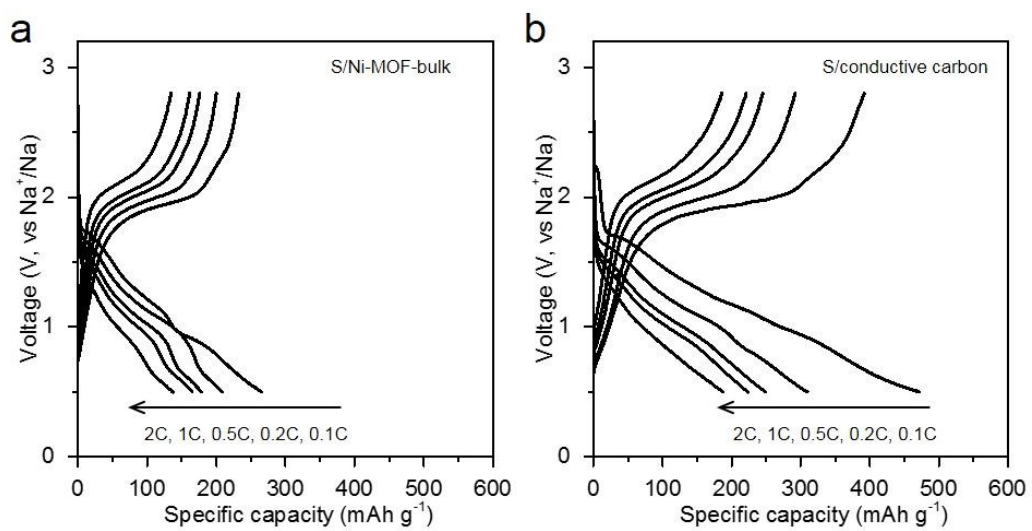
Supplementary Figure 9. a and **b,** Discharge/charge curves of S/Ni-MOF-bulk and S/conductive carbon under rates from 0.1 to 2 C.
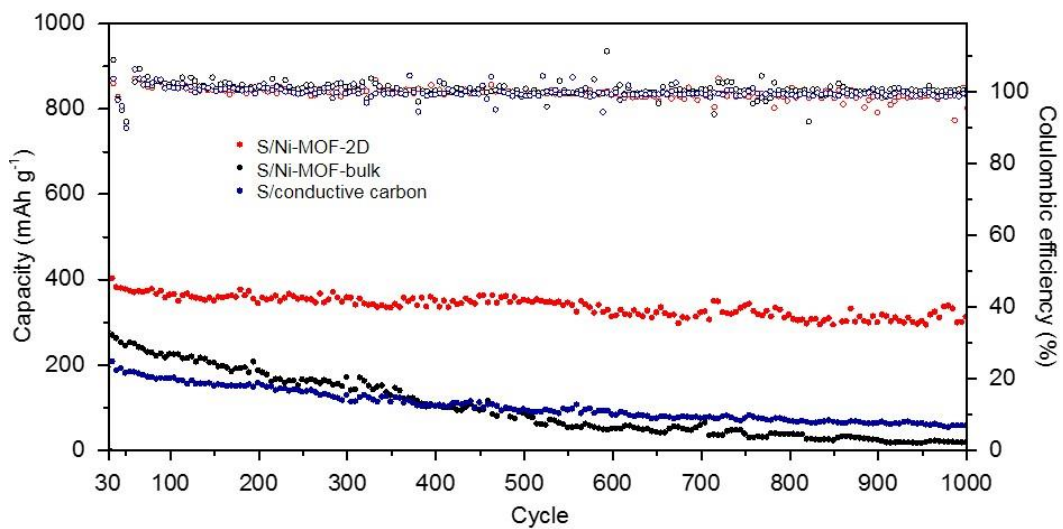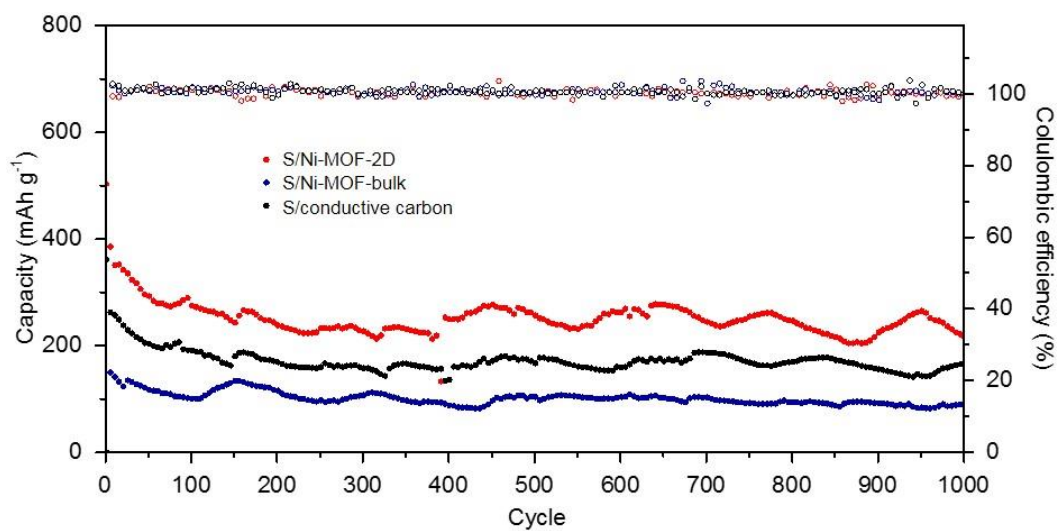
Supplementary Figure 10. Cycling performance and Coulombic efficiency (CE) of the three sulfur electrodes at 0.2 C following the rating test.
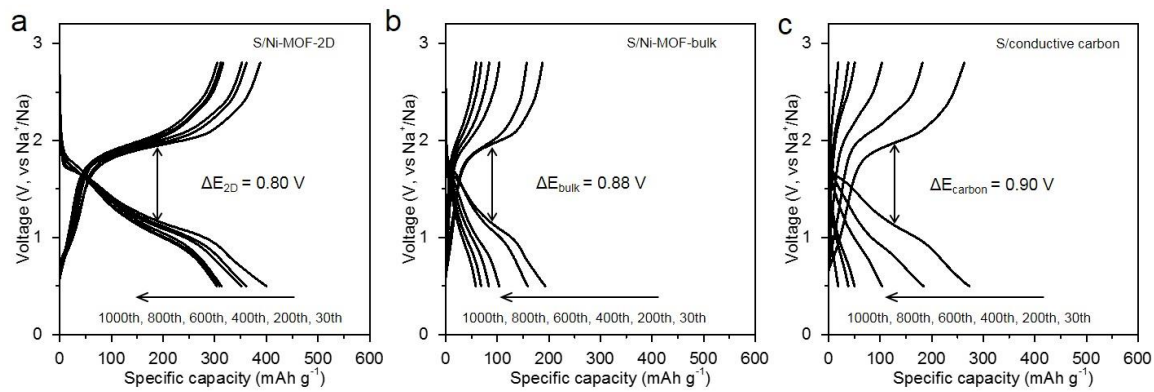
Supplementary Figure 11. a-c, Discharge/charge curves of S/Ni-MOF-2Dc, S/Ni-MOF-bulk and S/conductive carbon at 0.2 C following the rating test.
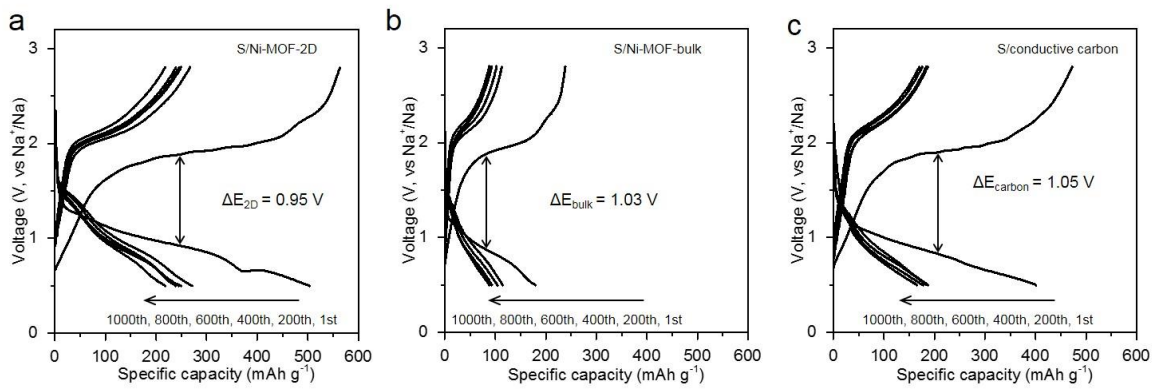
Supplementary Figure 12. a-c, Discharge/charge curves of S/Ni-MOF-2D, S/Ni-MOF-bulk and S/conductive carbon at 1 C.
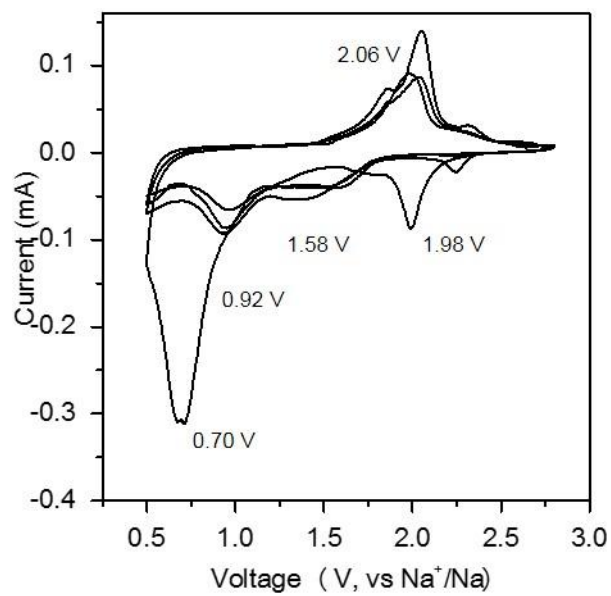
Supplementary Figure 13. Cycling performance and CE of the three sulfur electrodes at 2 C.
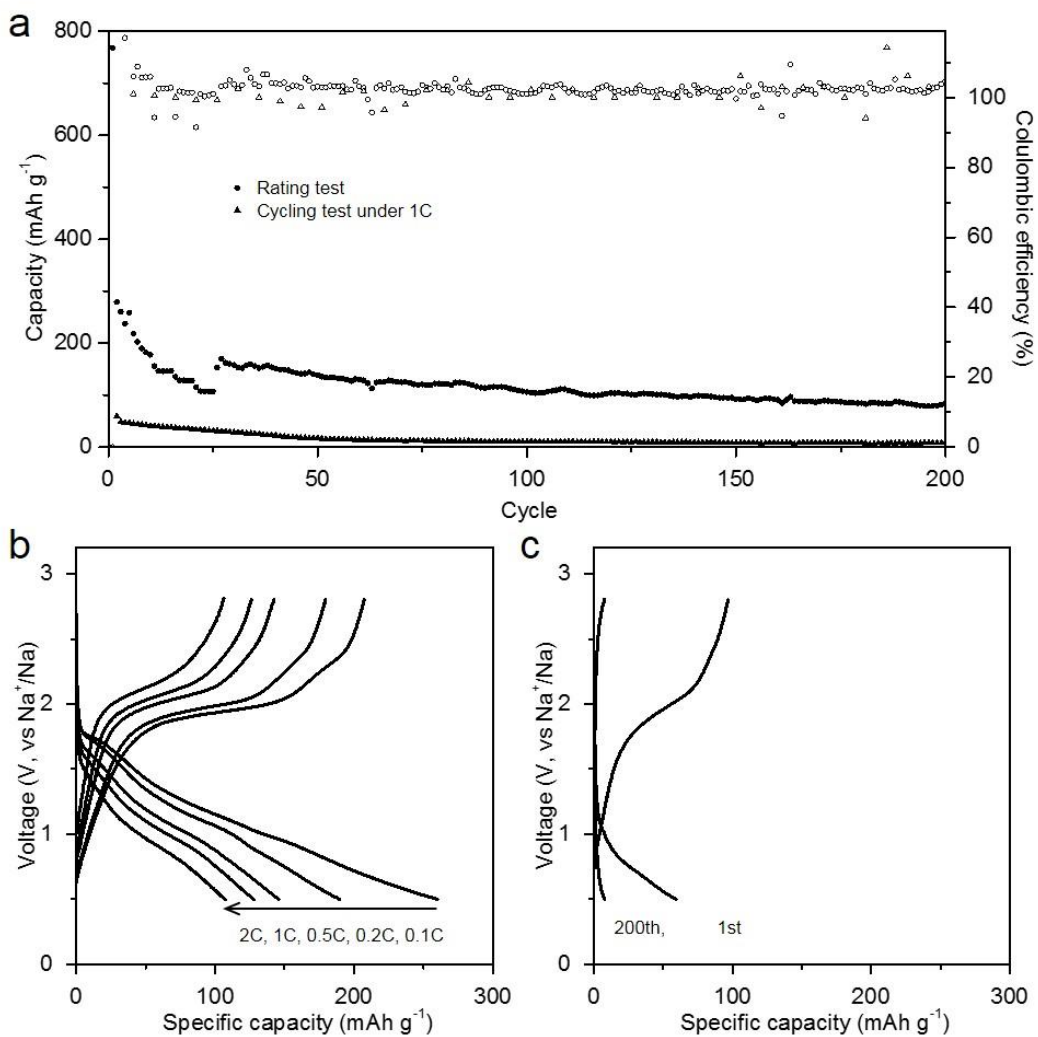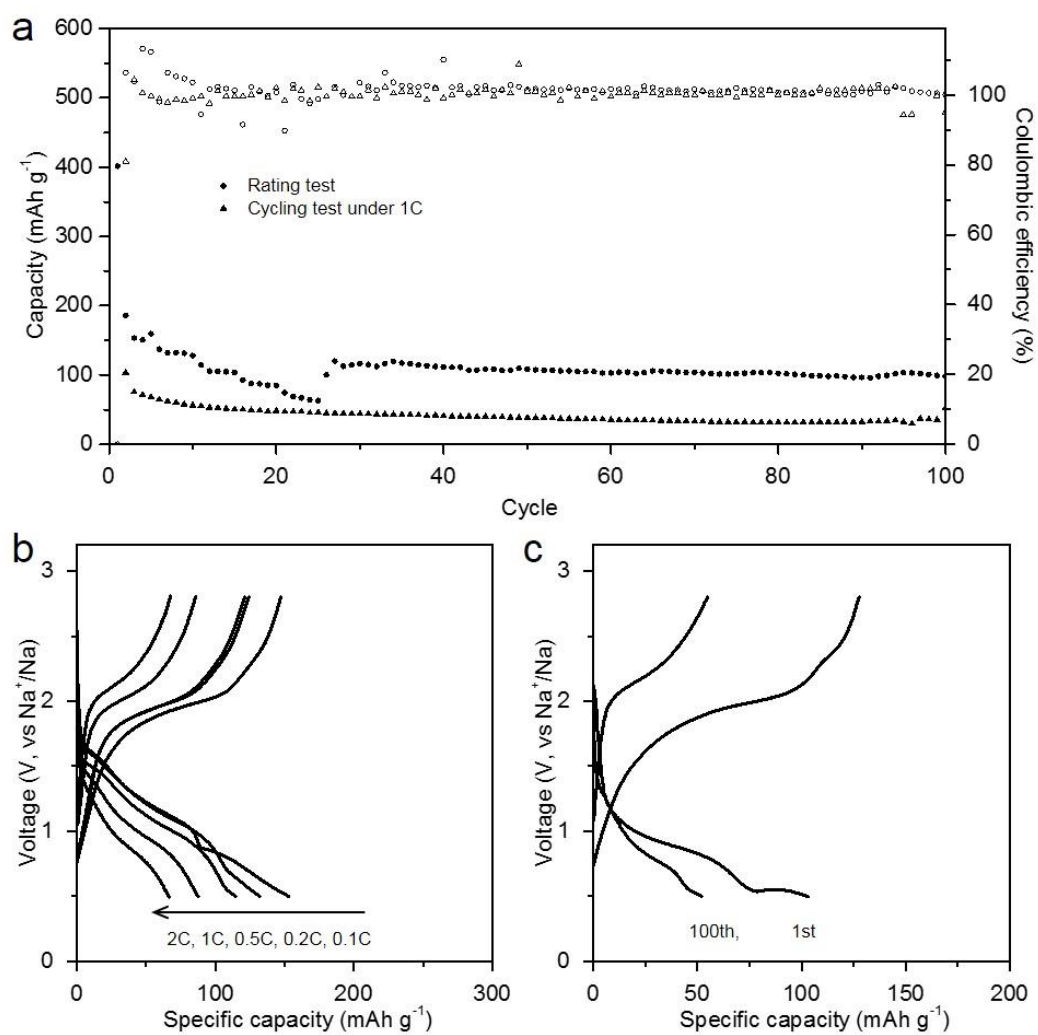
Supplementary Figure 14. a-c, Discharge/charge curves of S/Ni-MOF-2D, S/Ni-MOF-bulk and S/conductive carbon at 2 C.

Supplementary Figure 15. Cyclic voltammograms (CV) curves of S/Ni-MOF-bulk.

**Supplementary Figure 16. a,** Rating capacities and cycling performance at 1 C of the S/ligand. **b** and **c,** Discharge/charge curves of the S/ligand in the rating and cycling test.

Supplementary Figure 17. a, Rating capacities and cycling performance at 1 C of S/Ni-BDC. **b** and **c,** Discharge/charge curves of the S/ligand in the rating and cycling test.
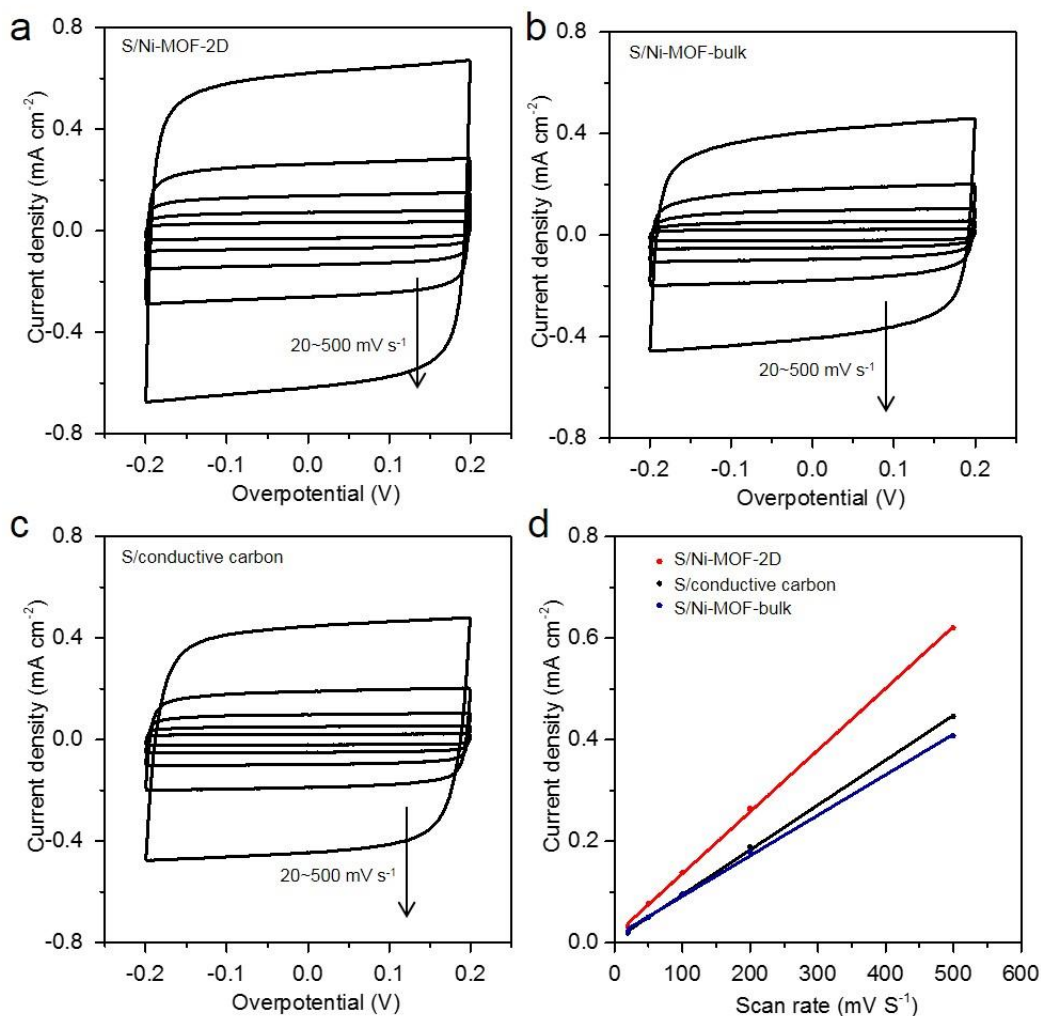
Supplementary Figure 18. Determination of the electrochemically active surface area (ECSA) of the three sulfur cathodes. a-c, CV) curves of S/Ni-MOF-bulk, S/Ni-MOF-bulk and S/conductive carbon symmetrical cells. **d**, Scan rate dependence of the current densities at 0 V. A series of CV tests under different scan rates from 20 - 500 mV s^{-1} were conducted to investigate the ECSA of the three sulfur cathodes. It is accepted widely that the ECSA of a materials of similar composition can be directly compared by measuring the slopes of the linear relations between current densities and scan rates. S/Ni-MOF-2D exhibited a greater linear slope than that for S/Ni-MOF-bulk and S/conductive carbon. This strongly suggests a meaningfully greater ECSA for S/Ni-MOF-2D. The boosted ECSA of S/Ni-MOF-2D is ascribed to its 2D morphology together with greater numbers of exposed active sites.
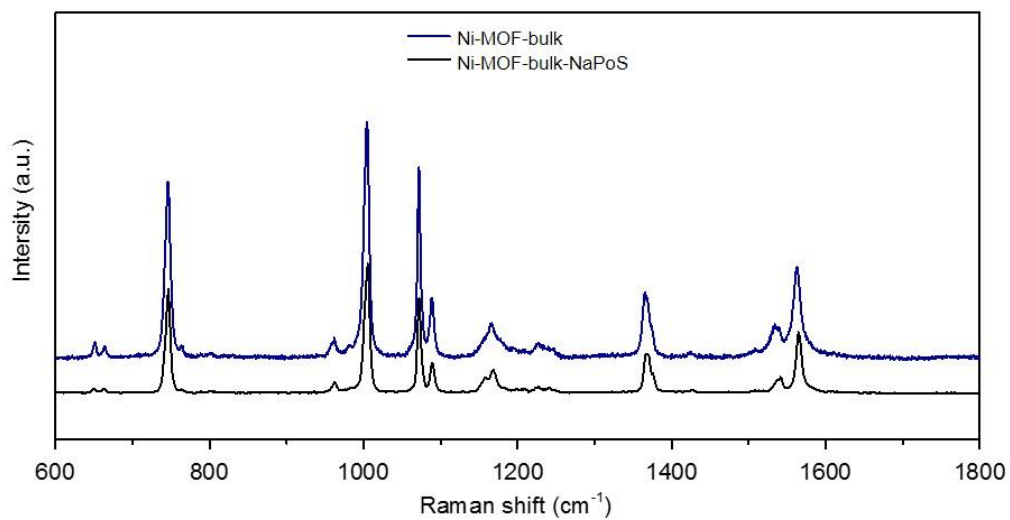
Supplementary Figure 19. Raman spectra of Ni-MOF-bulk and Ni-MOF-bulk-NaPoS. The ν ring and ν C-S bands of Ni-MOF-bulk-NaPoS remain almost the same as those of Ni-MOF-bulk, suggesting weak interaction between Ni-MOF-bulk and NaPoSs.
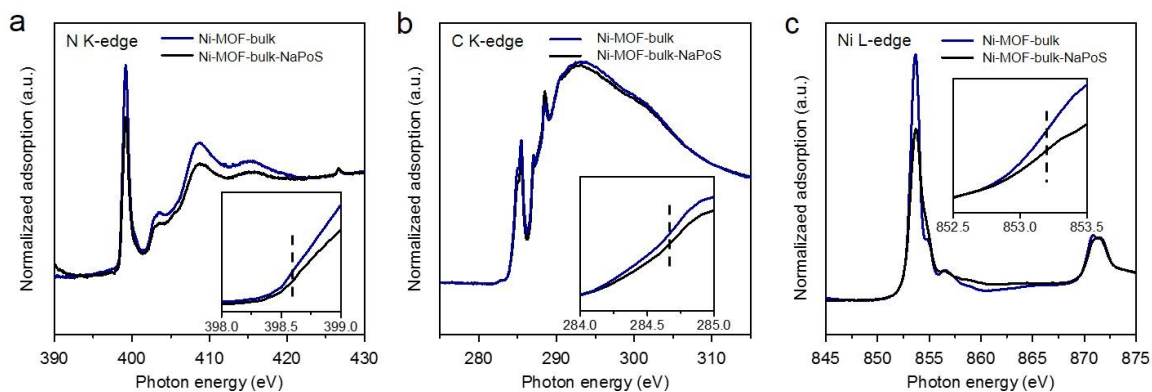
Supplementary Figure 20. Analysis of charge transfer between Ni-MOF-bulk and NaPoSs. a-c, N K-edge, C K-edge and Ni L-edge NEXAFS spectra of the two samples. These show Ni-MOF-bulk-NaPoSs with almost the same white-line adsorption energies as those for Ni-MOF-bulk except that charge transfer from N to the NaPoSs is due to weak electrostatic interaction.
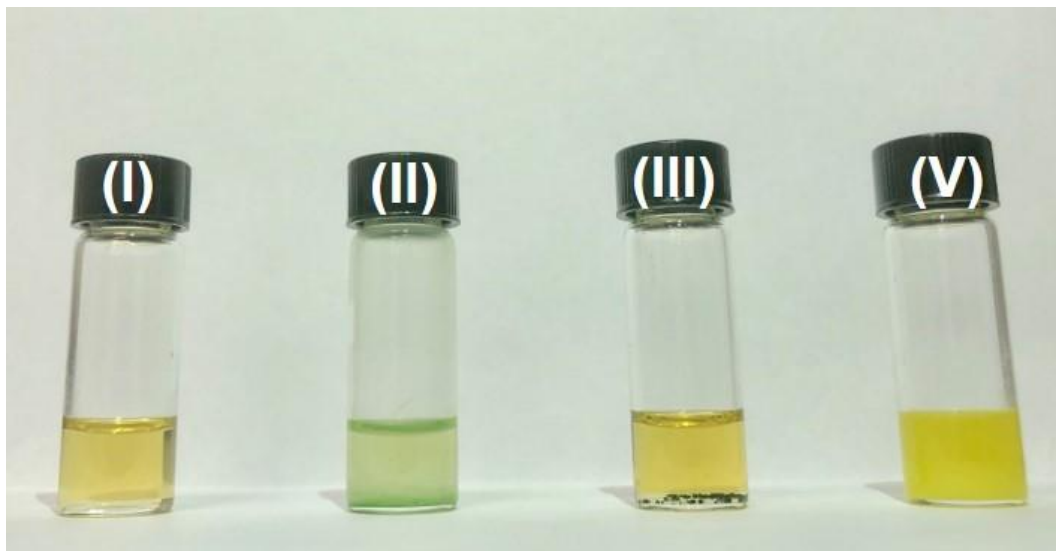
Supplementary Figure 21. Adsorption capacities of Ni-MOF-2D, Ni-MOF-bulk and PymSH. Optical images of (I) blank 0.5 mM Na_2S_x solution and (II)-(V) Ni-MOF-2D, Ni-MOF-bulk and PymSH following 1 h treatment with Na_2S_x solution.
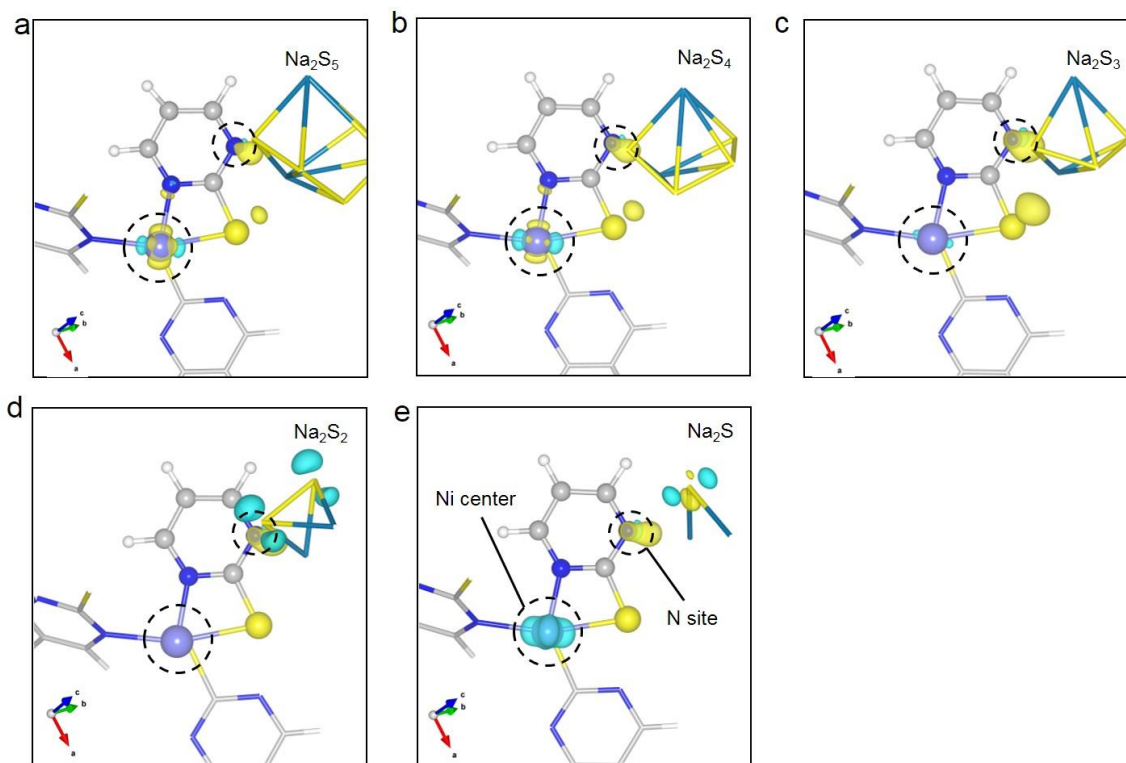
Supplementary Figure 22. a-e, Charge differences in configurations of Ni-MOF-2D-Na$_2$S$_n$. The color code is the same as with Fig. 5b. The iso-surface value = 0.005 e Å^{-3}.
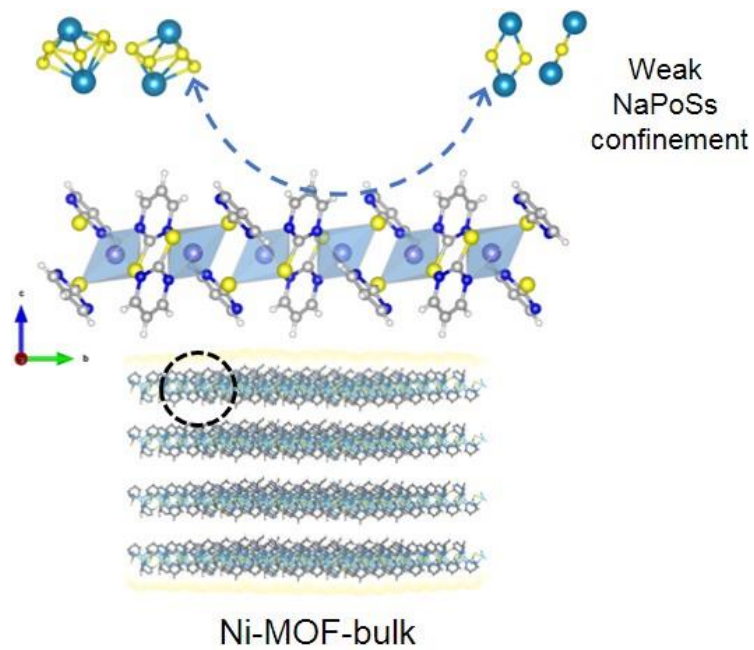
Supplementary Figure 23. Schematic for NaPoSs confinement on Ni-MOF-bulk.
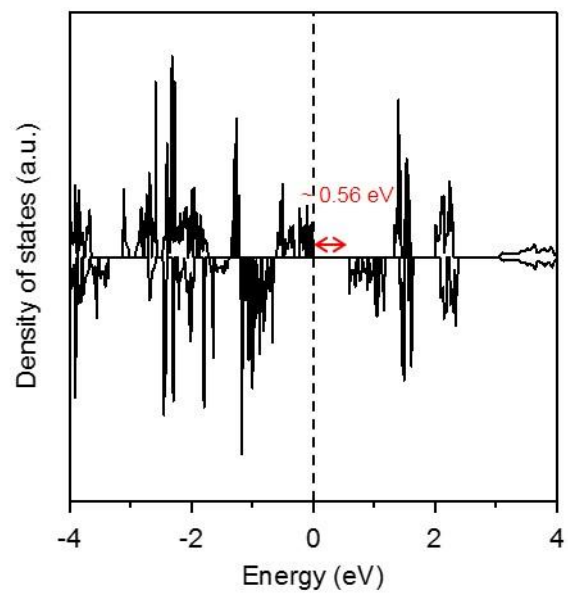
Supplementary Figure 24. DOS analysis of Ni-MOF-2D.

Supplementary Tables

Supplementary Table 1. Bader charges of S atoms and Ni atoms in the super cells (Supplementary Fig. 6).

Sample	Bader charge (e⁻)	
	Q_S	Q_{Ni}
Ni-MOF-2D	0.22	-0.89
Ni-MOF-bulk	0.25	-0.95

Supplementary Table 2. Summary comparison of performance of RT Na-S batteries.

Sample	Rate (C)	Cycles	Capacity decay (% per cycle)	Reversible capacity (mAh g^{-1})	Ref.
S/ Ni-MOF-2D	0.2	970	0.024	313 (after rate tests)	This work
	1	1000	0.042	347	
	2	1000	0.052	242	
S/ hollow carbon on carbon nanofibers	2	400	0.044	256	[1]
Hollow Na$_2$S	1.67	100	0.57	300	[2]
S/Fe on hollow carbon nanospheres	0.06	1000	0.061	394	[3]
S/carbon microspheres	~ 0.06	350	~ 0.21	~ 300	[4]
S/carbon fiber cloth	0.1	300	0.3	120	[5]
S/microporous carbon	0.1	250	0.23	410	[6]
S/hollow carbon	~ 0.06	200	~ 0.38	292	[7]
S/Nafion@separator	0.1	20	~ 0.63	350	[8]
S/carbonized ZIF-8	0.2	250	0.17	500	[9]
S/carbon	~ 0.05	900	0.053	517	[10]
S/microporous carbon	0.5	100	0.31	~ 400	[11]
S/Co on carbon	~ 0.06	600	0.088	507	[12]

Supplementary Table 3. ΔE values for the three sulfur cathodes estimated at 50 % DOD.

Rate (C)	ΔE (V)		
	ΔE_{2D}	ΔE_{bulk}	ΔE_{carbon}
0.2	0.80	0.88	0.90
1	0.96	1.04	1.06
2	0.95	1.03	1.05

Supplementary Table 4. Computed electrochemically active surface area (ECSA) and normalized capacities of the three sulfur cathodes.

Sample	C_{dl} (mF cm^{-2})	R_f^a	ECSA^b (cm^2)	Normalized capacity^c (mA h g^{-1} cm^{-2})		
				0.2 C	1 C	2 C
S/Ni-MOF-2D	1.233	20.55	23.33	13.4	15.1	10.4
S/Ni-MOF-bulk	0.864	14.40	16.27	3.6	5.2	5.3
S/conductive carbon	0.931	15.52	17.53	1.1	8.8	8.2

[a] R_f was calculated from dividing C_{dl} by the capacitance of ideal-planar metal-oxides with smooth surface taken as 0.06 mF cm^{-2}.

[b] ECSA were calculated from multiply R_f by the electrode geometric area of 1.13 cm^2.

[c] Normalized capacities were calculated from dividing the value of specific capacity by the corresponding surface area.

Supplementary Note 1. XPS Analyses of valence states

As is seen in Supplementary Figs. 8 the N 1s profiles exhibit five (5) peaks of Ni-MOF-2D spectrum centered at 402.3, 400.8 (400.0), 399.2 and 398.4 eV that can be attributed to oxidized N, N-H, N-C and N-Ni, respectively, all of which are less than those for Ni-MOF-bulk[13]. A similar trend is observed on C 1s XPS spectra in which Ni-MOF-bulk exhibits the four (4) peaks but centered at greater binding energies than those observed for Ni-MOF-2D, suggesting a lower C valence state for the latter. The C 1s XPS spectra of Ni-MOF-2D can be fitted into four (4) peaks centered at 287.8, 286.8, 285.8 and 284.5 eV that can be assigned to N-C-N, C-N, C-N-Ni and C-C species, respectively[14, 15]. Similarly, Ni 2p XPS spectra of Ni-MOF-2D can be fitted into a pair of doublets centered at 853.8 and 870.6 eV that can be assigned to Ni^{2+} $2p_{3/2}$ and $2p_{1/2}$, whilst the corresponding peaks for Ni-MOF-bulk shift to 854.2 and 871.6 eV. In contrast in the S 2p region of Ni-MOF-2D, two well-resolved peaks, corresponding to the $2p_{3/2}$ and $2p_{1/2}$ split orbits of sulfur in the thiolate form, occur at 161.9 and 163.0 eV. These indicate an upshift of S valence state relative to those of Ni-MOF-bulk. Therefore, as compared with Ni-MOF-bulk, Ni-MOF-2D shows lower valence states for C, N and Ni and a higher valence state for S.

Supplementary References

1. Xia, G. *et al.* Carbon hollow nanobubbles on porous carbon nanofibers: An ideal host for high-performance sodium-sulfur batteries and hydrogen storage. *Energy Storage Materials* **14**, 314-323 (2018).

2. Wang, C. *et al.* Frogspawn‐coral‐like hollow sodium sulfide nanostructured cathode for high‐rate performance sodium–sulfur batteries. *Adv. Energy Mater.* **9**, 1803251 (2018).

3. Zhang, B.-W. *et al.* Long-life room-temperature sodium–sulfur batteries by virtue of transition-metal-nanocluster–sulfur interactions. *Angew. Chem. Int. Ed.* **58**, 1484-1488 (2019).

4. Zhang, L. *et al.* Self-assembling hollow carbon nanobeads into double-shell microspheres as a hierarchical sulfur host for sustainable room-temperature sodium–sulfur batteries. *ACS Appl. Mater. Interfaces* **10**, 20422-20428 (2018).

5. Lu, Q. *et al.* Freestanding carbon fiber cloth/sulfur composites for flexible room-temperature sodium-sulfur batteries. *Energy Storage Materials* **8**, 77-84 (2017).

6. Carter, R., Oakes, L., Douglas, A., Muralidharan, N., Cohn, A. P., Pint, C. L. A sugar-derived room-temperature sodium sulfur battery with long term cycling stability. *Nano Lett.* **17**, 1863-1869 (2017).

7. Wang, Y.-X. *et al.* Achieving high-performance room-temperature sodium–sulfur batteries with s@ interconnected mesoporous carbon hollow nanospheres. *J. Am. Chem. Soc.* **138**, 16576-16579 (2016).

8. Bauer, I., Kohl, M., Althues, H., Kaskel, S. Shuttle suppression in room temperature sodium–sulfur batteries using ion selective polymer membranes. *Chem. Commun.* **50**, 3208-3210 (2014).

9. Chen, Y.-M. *et al.* A nitrogen doped carbonized metal–organic framework for high stability room temperature sodium–sulfur batteries. *J. Mater. Chem. A* **4**, 12471-12478 (2016).

10. Fan, L., Ma, R., Yang, Y., Chen, S., Lu, B. Covalent sulfur for advanced room temperature sodium-sulfur batteries. *Nano energy* **28**, 304-310 (2016).

11. Wei, S. *et al.* A stable room-temperature sodium–sulfur battery. *Nat. Commun.* **7**, 11722 (2016).

12. Zhang, B.-W. *et al.* Atomic cobalt as an efficient electrocatalyst in sulfur cathodes for superior room-temperature sodium-sulfur batteries. *Nat. Commun.* **9**, 4082 (2018).

13. Pei, F. *et al.* Self-supporting sulfur cathodes enabled by two-dimensional carbon yolk-shell nanosheets for high-energy-density lithium-sulfur batteries. *Nat. Commun.* **8**, 482 (2017).

14. Chen, B. *et al.* Controllable graphene incorporation and defect engineering in mos2-tio2 based composites: Towards high-performance lithium-ion batteries anode materials. *Nano Energy* **33**, 247-256 (2017).

15. Zhang, H.-L., Evans, S. D., Henderson, J. R., Miles, R. E., Shen, T. Spectroscopic characterization of gold nanoparticles passivated by mercaptopyridine and mercaptopyrimidine derivatives. *J. Phys. Chem. B* **107**, 6087-6095 (2003).

Chapter 6 Conclusion and perspectives

It is now possible to practically tailor geometric/physicochemical properties of cathode materials to boost electrochemical performance of Li/Na-S batteries using strategies such as the introduction of dopants/defects, fabricating hybrids and heterostructures. However, a number of issues remain, these include:

1. Missing descriptors – these are needed to link macroscopic conversion kinetics and microscopic electronic structures in cathode/anode materials. Theoretical computations have therefore only occasionally been used to predict electrochemical performance. This is partially due to a limitation of current computing power and the complexity of the cathode/anode interfacial reaction, together with the wide range of physicochemical properties of current 2D nanomaterials.

2. Agreed standards – these are needed to evaluate electrochemical behaviour at atomic/molecular level. To correlate microscopic physicochemical/electronic properties of 2D materials, and electrochemical performance in sulfur cathodes or metal anodes, identical standards are essential for both evaluation and comparison. For example, specific surface area of 2D nanomaterials and resultant electrochemically active surface areas (ECSAs) of synthesized electrodes highly significantly impact electrochemical performance. An agreed standard will obviate the impact of differing number and density of active sites, and more accurately permit comparison of intrinsic activities of site and establish accurate property-performance relationships.

3. Accelerated combined experiment and theory – this is needed to develop further the proven fruitful approach. A combination of advanced in situ characterization techniques, operando theoretical computations and microscopy is needed to accelerate research to better

understand conversion kinetics of sulfur intermediates and Li/Na stripping-plating. The properties of 2D nanomaterials might change dynamically during discharge/charge. For example, in situ XAS is a powerful tool that can be used to detect various sulfur intermediates and dynamic chemical structures of 2D materials. Resulting information will be of significant value to determine reaction mechanisms and to guide design of cathode/anode materials.

4. Three-dimensional (3D) electrodes from 2D nanomaterials – this might be a practical approach to meet requirements for metal-sulfur batteries commercialization. Sulfur cathodes and metal anodes with high mass loading and content of active materials are highly desired in practical application. Theoretically, 2D nanomaterials possess promising large active surface area to host sulfur/metal. Nevertheless, a part of the electrochemical active sites on 2D nanomaterials might be blocked in routine slurry electrodes. A promising approach might be fabrication of 3D electrodes from 2D nanomaterials with optimized pore volume and pore structure to take full advantage of their large surface area. Importantly the 3D cathodes with a high sulfur loading (> 6 mg cm^{-2}), sulfur content (> 70 %) and low porosity (< 70 %) are essential to improve volumetric energy density of the metal-sulfur batteries so as to be comparable with commercial Li-ion batteries (~ 600 Wh L^{-1}). Notably, large surface area of 2D nanomaterials would result in electrolyte depletion. Therefore, control the electrolyte content to an acceptable level is another crucial factor to promote the energy/power density of the metal-sulfur batteries.

5. Advanced materials to develop other metal anodes for metal-sulfur batteries. For example, although mechanisms of potassium stripping-plating in corresponding potassium-sulfur batteries have been rarely studied, use of artificial SEI and host materials have proven

effective in K-metal anode protection. With multivalent metal-sulfur batteries such as Mg/Ca/Al-S, strategies might need to be different to develop metal anodes. For example, although the Mg deposition is nondendritic, sluggish kinetics of Mg ions transfer in SEI results in an electric/ionic nonconductive film on Mg metal surface. This leads to uselessness of the Mg anode. 2D nanomaterials as artificial SEIs can act as ion sieve membrane to conduct metal ions and prevent surface passivation on the multivalent metal anodes. The impact of additives and solvents on metal ion diffusion barriers in SEIs could be better understood through transition state computations and AIMD simulations.

Based on overall findings from advanced materials we could expect the establishment of structure-capacity/stability relationships, together with increased insight into the mechanism for sulfur redox/metal stripping-plating from applying a judicious combination of advanced characterizations, electrochemical experiments and theoretical computations. Resulting fundamental understanding of interfacial reactions on sulfur cathodes and metal anodes will speed design for advanced materials to boost electrochemical properties in metal-sulfur batteries and in wider environmental sciences and energy conversions.